Component-wise Analysis of Reinforced Thin-walled Metallic and Composite Structures

ScuDo
Scuola di Dottorato ~ Doctoral School
WHAT YOU ARE, TAKES YOU FAR

Doctoral Dissertation
Doctoral Program in Mechanical Engineering (29^{th} cycle)

Component-wise Analysis of Reinforced Thin-walled Metallic and Composite Structures

By

Tommaso Cavallo

******

Supervisors:
Prof. Erasmo Carrera
Dr. Enrico Zappino

Doctoral Examination Committee:
Prof. Giunta Gaetano, Referee, Luxembourg Institute of Science and Technology
Prof. Fazzolari Fiorenzo, Referee, University of Cambridge
Prof. Andrea Alaimo, Universitá Kore di Enna
Prof. Lorenzo Dozio, Politecnico di Milano
Prof.ssa Maria Cinefra, Politcnico di Torino

Politecnico di Torino
27 June 2017

I hereby declare that, the contents and organization of this dissertation constitute my own original work and does not compromise in any way the rights of third parties, including those relating to the security of personal data.

Tommaso Cavallo
2017

A mia moglie Mihaela
con la quale ho condiviso
interamente le gioie e
le diffocoltá che questi
tre anni hanno riservato.

Ringraziamenti

L'esperienza del dottorato si é rivelata unica non solo perché ha arricchito le mie competenze tecniche ma anche perché mi ha permesso di trascorrere un perido stupendo in un gruppo speciale, il gruppo MUL^2, ricco di persone che amano fare il loro lavoro.
Tutto questo si é reso possibile solo grazie alla professionalitá e alle competenze che il Prof. Erasmo Carrera mette tutti i giorni a disposizione. Un pensiero speciale va proprio a Lui, per avermi supportato non solo dal punto di vista professionale ma anche personale.
Un sentito ringraziamento va al Dott. Enrico Zappino, al quale ho fatto riferimento nelle diverse attivitá. Con la sua professionalitá e umiltá é sempre stato pronto a supportarmi.
In fine, ma non per importanza, ringrazio i miei genitori, *Francesco* e *Maria*, che mi hanno insegnato a raggiungere i risultati con l'impegno e con la costanza e a superare le diffoltá con la determinazione.
Ció che io sono adesso lo devo anche a voi e ve ne saró sempre grato.

Summary

Reinforced structures are thin structures reinforced using additional components, which are joined using different technologies, milling, riveting or welding. The technological process used to realize a reinforced structure makes it possible to have structural continuity between elements on which it is realized, such as the plate, stringers, and ribs. In fact, when a reinforced structure is realized using a milling machine, the stringer derives from the same workpiece and inevitably the continuity between plate and stringers is guaranteed.

When the classical joints, like welding and rivets, are used the congruence of the displacements is verified only in a portion of the interface; moreover, the joints may have a lower strength of the original material. For these reasons the mathematical model used is crucial because otherwise the results are not representative of the component analyzed.

Accurate analyses of reinforced structures require the use of 3D (Solid) FEM (Finite Element Method) models. A large number of degrees of freedoms (DOFs) is needed, and the computational costs could become prohibitive when solid models are used. 2D (Shell) and 1D (beam) models are used instead of 3D models to reduce the CPU in FEM analysis. These simplified mathematical models introduce assumptions, based on geometrical and kinematic approximations, which reduce the DOFs but could largely increase the error. For these reasons contribution direct to introduce efficient and robust reduced models are welcome.

Among these, those referenced as "Component-Wise" approaches which are based on FEs based on Carrera Unified Formulation (CUF) have been recently proved to be a reliable framework for further developments which are the object of the present research proposal. Various analysis of simple components, such as plate and curved reinforced panels, are considered to analyze the effect of the stringers in the FE models compared to the 1D-CUF models.

The stringer changes the solution locally, in term of stress and displacement field and also regarding the local vibration because indeed the local strength increases. The shape of the stringer is an additional parameter to consider when reinforce structures are modeled using the refined models (beam and shell/plate) in the FE modeling.

The one-dimensional CUF formulation is also used to analyze the effect of the

reinforced configurations in the case of complex structures In fact, in the case of reinforced cylindrical components or launchers, the reinforced layout must be modeled considering the local and the global effects. Composite materials, non-structural masses, and load-factor are included in the analysis, performing the implications for the dynamic analysis due to the different approaches used in the modeling.

Various FE models are used to carry out the results of the FE modeling. In particular, in the 3D FE models, both plate and stringer are modeled using the same solid elements. In the 2D FE models, shell elements are utilized for the plate and also for the stringers. In contrast, the 2D-1D FE models are characterized by the coupling between shell and beam elements, in particular, the shell elements are used for the plate while the beam elements for the stringers. The 3D, 2D, and 2D-1D models are analyzed using the commercial NASTRAN code, where the 3D solution is used as the reference solution.

The results show the need for the reduced FE models to adopt appropriate valuations and accurate analysis when reinforced structures are modeled, because the stringer and its shape can influence the static and dynamic analyses.

In addition, the results show the capabilities of the present approach to deal with the analysis of conventional complex space structure. The results indicate that the current models can give accurate results with a high reduction in the computational cost with respect traditional approaches.

Sommario

Le strutture irrigidite sono caratterizzate da piastre sottili rinforzate mediante l'uso di componenti aggiuntivi, detti irrigidimenti o correnti. L'uso dei materiali metallici permette di utilizzare diverse tecnologie per collegare gli irrigidimenti. I giunti meccanici non smontabili, comunemente chiamati rivetti, permettono di giuntare i diversi componenti ma solo in corrispondenza del giunto stesso, quindi la giunzione é localizzata. In aggiunta, tra l'irrigidimento e la piastra la continuitá strutturale non puó essere garantita in quanto essi provengono da differenti blocchi di materiale. La saldatura é il procedimento che permette l'unione fisico/chimica di due giunti mediante la fusione degli stessi, o tramite metallo d'apporto. L'area saldata, detta cordone di saldatura, si distribuisce normalmente lungo l'intera lunghezza dell'irrigidimento, garantendo quindi una giunzione distribuita. Tuttavia, come nella rivettatura, il componente finale sará sempre caratterizzato da una certa discontinuitá strutturale perché anche in questo caso gli elementi saldati sono a sé stanti. Diverso é invece il caso in cui un componente irrigidito é realizzato mediante il processo della lavorazione meccanica per asportazione di truciolo. In questo caso, l'utensile ruotando ad alta velocitá e traslando, rimuove ad ogni passata il metallo in eccesso, con il risultato che al componente finale sará garantita la continuitá strutturale in corrispondenza della giunzione tra la piastra e il corrente. Il componente irrigidito presenterá quindi delle caratteristiche meccaniche fortemente dipendenti dal processo tecnologico utilizzato per la sua realizzazione. In fase di progettazione, l'uso di svariati approcci permette di valutare con una accuratezza variabile lo stato di deformazione e di tensione al quale il componente é soggetto sotto l'azione di carichi di svariata natura.

In campo industriale il Metodo agli Elementi Finiti (FEM) é quello piú diffuso. Il FEM permette di utilizzare i modelli strutturale classici per lo studio delle strutture compresse per le quali non é possibile avere una soluzione in forma chiusa. In aggiunta, la semplicitá con la quale il FEM puó essere implementato all'interno di codici di calcolo automatico, ha spinto gli ingegneri ad un continuo sviluppo che, unito all'incremento delle prestazioni dei moderni calcolatori, ha reso il metodo FEM molto efficace. Negli ultimi cinquant'anni sono stati sviluppati molti codici commerciali basati sul FEM, i piú noti sono il codice *Nastran*® sviluppato dalla *MSC*

o *Abaqus* della *Dassault Systé mes* o ancora *Radioss* sviluppato da *Altair*. I classici modelli strutturali usati nei codici commerciali sono gli elementi trave, basati sui modelli monodimensionali di Euler-Bernoulli o Timoshenko, e gli elementi piastra o bidimensionali, che si rifanno alle teorie di Kirchhoff o Mindlin. I modelli 1D e 2D sono comunemente detti ridotti, ovvero essi risultano avere una cinematica piú semplice basata quindi su semplificazioni matematiche e geometriche. Tuttavia, le limitazioni introdotte dalle approssimazioni rendono tali modelli poco efficaci nell'analisi di strutture avanzate, per questo quando si richiede uno studio di dettaglio, gli elementi solidi, ovvero tridimensionali, sono la soluzione migliore in quanto prive di approssimazioni. La forma e il numero degli elementi solidi usati per discretizzare il componente, influisce notevolmente sul risultato finale, richiedendo spesso un elevato numero di elementi 3D necessari per l'intera struttura. Un aumento degli elementi 3D usati determina un incremento del numero di incognite, o gradi di libertá, con il risultato di avere dei costi computazionali talmente elevati che un singolo processo di analisi puó durare giorni o settimane. Per questo motivo che i modelli risotti 1D e 2D sono fortemente usati in sostituzione di quelli 3D, e l'accoppiamento tra elementi 2D e 2D-1D permette di discretizzare le strutture irrigidite. Tuttavia, la diversa cinematica che caratterizza i modelli ridotti 1D e 2D rende sempre complicato il loro collegamento dal punto di vista matematico, e ció introduce degli errori che difficilmente sono colti dall'ingegnere. In aggiunta, per le strutture realizzate con l'asportazione di truciolo, solo i modelli solidi sono in grado di dare una rappresentazione fedele del componente perché in questo caso tra corrente e piastra c'é continuitá strutturale.

Questa tesi propone l'utilizzo dei modelli raffinati di tipo unidimensionale per lo studio delle strutture irrigidite. L'interfaccia tra piastra e irrigidimento é l'area della struttura irrigidita piú complessa da analizzare in quanto sede di comportamenti locali fortemente dipendenti dal modello adottato per il suo studio. L'uso dei modelli raffinati 1D, oltre ad aver permesso di analizzare i temi principali nell'analisi locale dell'interfaccia e quindi dell'effetto sulla struttura globale, ha permesso di studiare tutte quelle problematiche che l'accoppiamento tra i modelli ridotti 1D e 2D nella modellizzazione classica agli elementi finiti introduce, e che normalmente sono trascurate. Lo studio in dettaglio di modelli di piastre e gusci irrigiditi, ha fornito e basi per l'estensione dei modelli 1D raffinati a strutture complesse come cilindri irrigiditi e lanciatori. In aggiunta, i materiali compositi rendono sempre difficili le analisi dei modelli FEM perché l'orientamento delle fibre varia in modo consistente le proprietá meccaniche del materiale sia localmente che globalmente. In questo lavoro é stato possibile estendere l'uso dei materiali compositi alla realizzazione e all'analisi delle strutture complesse, analizzando in aggiunta l'effetto sulle caratteristiche dinamiche della variazione della massa e della presenza di un fattore di carico, sia dei componenti che dell'intero modello di lanciatore. Oltre ai modelli 1D raffinati derivati dalla Carrera Unified Formulations, CUF, vari modelli classici agli elementi

finiti sono stati usati non solo per analizzare le tematiche nell'ottica della progettazione industriale, ma anche per studiare gli effetti derivanti dalla modellizzazione di strutture irrigidite con i modelli ridotti 1D e 2D. La CUF permette di derivare modelli con qualsiasi cinematica, 1D, 2D e 3D, utilizzando una formulazione unificata, indipendente dalla cinematica scelta. Un ulteriore vantaggio introdotto dai modelli CUF, é la possibilitá di modificare a piacimento i vincoli in ogni punto della struttura, permettendo di studiare le strutture irrigidite realizzate con qualunque processo tecnologico attraverso la stessa formulazione. In questo lavoro i modelli monodimensionali CUF sono usati non solo per lo studio di componenti irrigiditi di forma semplice, piastre e gusci, ma anche per componenti complessi come cilindri irrigiditi e lanciatori. Tali modelli 1D CUF si sono dimostrati capaci di fornire risultati accurati riducendo drasticamente il costo computazionale nell'analisi delle strutture complesse irrigidite.

Contents

List of Tables

List of Figures

Chapter 1

Introduction

Reinforced structures are thin structures reinforced using different stringers, either longitudinal, stringers and transversal, ribs, joined using different technologies. In some aeronautical structures, such as fuselage components, stringers are joined to skins using riveting techniques, because it is simple to be used and because a rivet has a higher strength than a tack weld. But in this case, stringer and skins are joined in the area where there is the rivet. In this case between stringers and panels, there is not structural continuity. In other applications, components are welded using an additional material characterised by defined chemical and mechanical properties. The limit of welding technologies is the capability of the line welded to contains the physical defects moving on a less strength of the welded component. When a component is obtained using the milling technique, the stringer is a part of the original component, and the structural continuity is guaranteed. In this case, also the total strength is higher than a riveted or welded part. As a different technology can carry out the final component with a different level of strength, at some way the approach used to model a reinforced structure can carry out to a different result, with the risk to use or a high value of safety factor or to get results not accurate. These are exactly the kind of issues that are to be discussed by the scientific community because reinforced structures are very attractive structures in different engineering fields and their applications take different research groups to investigate on various engineering problems, including the problem due to the mathematical modeling.

1.1 Various applications of reinforced structures

Reinforced structures are capable of satisfying the strength and lightness requirements, both of which are important properties when the structural weight is a project parameter. In civil engineering, the structural weight becomes necessary when large infrastructures must be realized. Rods and tie rods are opportunely located with

the purpose of support normal and tangential stress. This simple configuration is widely used in bridges (Fig. 1.1a) where the metallic materials, in particular, the steel, are still used to reduce the total costs, and the structure can control the aerodynamic loads. In the same engineering area, skyscrapers (Fig. 1.1b) need of reinforced structural configuration because in this case aerodynamic loads and also seismic events require stiffness and flexibility requirements, by putting the safety of the public and the environment first.

(a) *Pedestrian bridge in Amsterdam*

(b) *Biggest skyscraper in New York*

Figure 1.1. Civil reinforced infrastructures.

In the past in mechanical engineering, the structural weight was one of the most important parameters to have been introduced in the project only for the sporting race for two- or four-wheel motor vehicles. Reinforced structures are also used in the traditional mechanical industry (Fig. 1.2) to limit greenhouse gas emissions because carbon dioxide emissions from traffic have increased by almost a third since 1990. In this years, chassis for car and motorcycle is also realized using lightweight alloys and composite material, how carbon fibers. This advanced structural configuration makes it possible to protects the occupants for less than 10 percent of the weight of a traditional steel chassis in a car.

In biomedical engineering for the upper (Fig. 1.5a) and lower (Fig. 1.5b) prosthetic limbs, the adopted reinforced structure has considerable achievements in this area, and developments makes it possible to improving the living conditions of people with physical disability. Ceramic and carbon fibers prosthetic limbs makes it possible to have a long life than the previous configurations, and prosthetic limbs life can reach about 25 years from surgery.

In the aerospace engineering field, the first example of reinforced structure can be observed in December 17, 1903, date on which the Wright brothers flights 1.4 are recognized by the Fédération Aéronautique Internationale (FAI), the standard setting and record-keeping body for aeronautics, as "the first sustained and controlled

(a) *Chassis for car* (b) *Chassis for motorcycle*

Figure 1.2. Mechanical reinforced structures.

(a) *Upper prosthetic limbs* (b) *Lower prosthetic limbs*

Figure 1.3. Biomedical reinforced components.

heavier-than-air powered flight".

Figure 1.4. The Wright Flyer on 1903.

In this case, the materials used were very poor, spruce, a strong and lightweight

wood, and Pride of the West muslin for surface coverings. Despite, the first flight lasted 12 seconds for a total distance of 120 ft (36.5 m), there has been a lot of publicity on this particular issue all over World. Both the arms industry as a whole has pushed the aircraft development during the first and second war world, and, the importance of developing a space-related industrial policy during the Space Race in 20th-century due to the competition between two Cold War rivals, the Soviet Union (USSR) and the United States (US) for supremacy in space-flight capability, created a massive influx of politic and social attention with a substantial economic value.

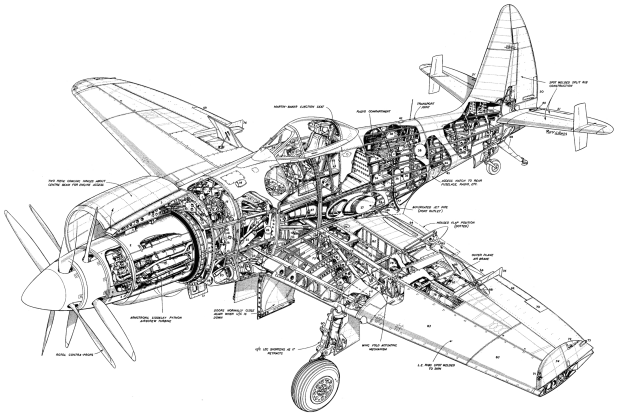

(a) *Westland Wives S.4*

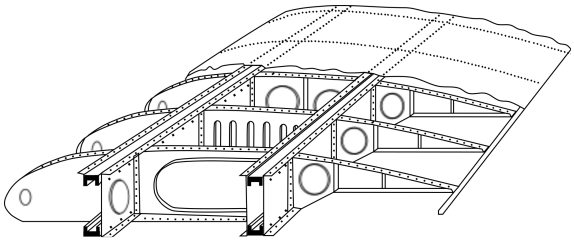

(b) *Wing box*

Figure 1.5. Aeronautical reinforced structures.

The engine has been developed to permit aircraft and space vehicle to fly with a high velocity, but considerable attention has been given to realize reinforced structures characterized by a higher value of strength with the lowest weight. The new technology, lightweight alloys, and composite materials have permitted reinforced structures to become necessary for all the engineering fields. The capability for engineers to design and analyzing components have improved various analytical approaches using different methods with the unique objective of modeling and analyzing complex structures such as reinforced structures.

1.2 The technologies for the construction of reinforced structures

An important issue in the modeling of reinforced structures is to represent correctly the structure configuration deriving from the technological process used to build them. Two main approaches can be used to obtain a reinforced structure; the former is based on the use of rivets or welding to join stringers and skins, while the latter relies on Computer Numerical Control, CNC, a technique where stringers are just connected to the skin.

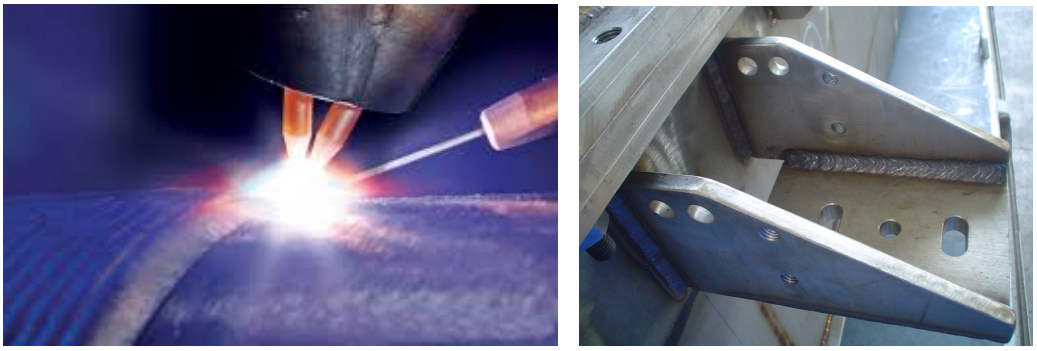

(a) *Wending Technology* (b) *Reinforced Welded component*

Figure 1.6. Aeronautical reinforced structures.

Welding is a process that joins materials, usually metals or thermoplastics, by causing fusion, which is distinct from lower temperature metal joining techniques such as brazing and soldering, which do not melt the base metal, Fig.1.6. In addition to melting the base metal, a filler material is typically added to the joint to form a pool of molten material (the weld pool) that cools to form a joint that is usually stronger than the base material. A classic problem in a welded component is the capability of the metal added to incorporate different physical defects. These defects take the component to a less global strength, mostly when the component is subjected to fatigue loads.

For these reasons that in some engineering field where the fatigue loads are very restrictively how in the aerospace engineering field, the riveting technology is the actual favorite method used to join stringers and panels because it is simple and cheaper. A standard application of rivets in aeronautical applications is shown in Fig1.7 where the ribs and stringers are connected to the fuselage panels using rivets. An additional advantage of riveting is the higher strength of a rivet then a tack weld. However, also in this case between stringer and skin, there is not structural continuity and in some application this an important aspect.

In the space structure, the CNC (Computer Numeric Control) technique is the

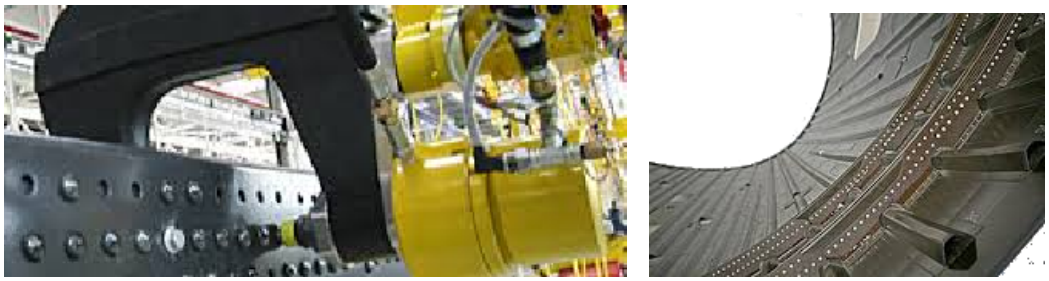

(a) *Riveting Technology* (b) *Aeronautical Riveted Component*

Figure 1.7. Aeronautical reinforced structures.

most-used class of technological process after riveting. Milling is the machining process of using rotary cutters to remove material from a workpiece by advancing (or feeding) in a direction at an angle with the axis of the tool. It covers a wide variety of different operations and machines, on scales from small individual parts to large, heavy-duty gang milling operations. As shown in Fig.1.8, when a structure is realized using the milling technique, the stringer is a part of the original component. From a geometrical point of view, the initial block of material is biggest than the last element, and the stringer is obtained by removing the excess material. Inevitably, the continuity between plate and stringers is guaranteed because they come from the same workpiece.

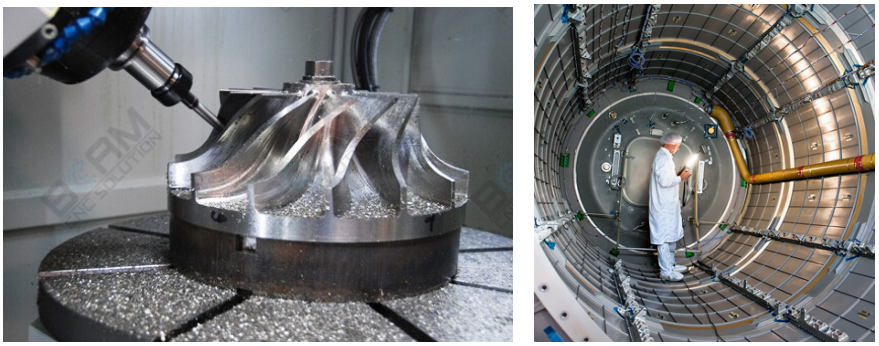

(a) *Milling Technology* (b) *Space Milled Component*

Figure 1.8. Space reinforced structures.

When stringers and skin are a unique component, only solid FE (3D) elements, can represent the structure, and the results can be very accurate. If the structure is welded, shell (2D) and (1D) beams elements also can be used to simulate the mechanical behavior, introducing acceptable errors in both discretization and results.

1.3 State of the art review of the reinforced structures analysis

In the last century, different approaches have been introduced to study reinforced structures with the purpose of investing the internal stress distribution in the static analyses and the dynamic behavior in the dynamic analyses. The complex shape of a generic reinforced structure has brought luminaries of mathematics and engineering to consider in the model some approximations for geometry and/or for the kinematic model used. Timoshenko is one of the first authors in developing of mathematical approaches based on a simple kinematic for a complex structure. Timoshenko [1959] obtained an equivalent orthotropic homogeneous panel of constant thickness by smearing-out the stiffness property of the ribs over the plate considering the ribs closely and evenly spaced in the panel. Omid'varan [1971] formulates a closed solution for the expression of the steady state frequencies of vibration of a simply supported plate stiffened by a grid. At some way, Omid'varan and Delagarza [1973] formulated the steady-state frequencies of vibration of grid-stiffened rectangular plates on which the plate and the grid are assumed to have a monolithic connection at the node points. However, the solution is validated only for the simply supported case with equal grid spacing. Troitsky [1976] published a book where stiffened plates are analyzed using the smearing technique and bending, stability and vibrations are treated. When this approach is used, the contribution of each component is evaluated locally, and it is then superimposed onto the global properties of the panel. When the number of ribs decreases, the plate and rib elements should be considered separately, and at least the congruence between them should be imposed. This approach requires finding the solution for the plate and stringers individually, considering both the unknown interface forces, due to the coupling between the components, and the direct loads. The interface forces, unlike direct loads, are unknown, and as a result, they must be computed iteratively to satisfy compatibility between the components, as shown in the works of Deb and M. [1988], Bert et al. [1989], Farsa et al. [1993], Civan [1994]. This method does not include the effect of torsion or shear transfer from the ribs to the plate. Earlier work on stiffened plates and stiffened cylindrical shells is introduced by Leissa [1993a], Leissa [1993b]. With smearing technique, the reinforced structure is treated as an equivalent orthotropic one, and the stiffeners'mass and stiffness are effectively smeared over the continuous shell or plate. As observed by Leissa [1993b] there are many thin-shell theories, which differ in the terms included accounting for shell bending. The smearing technique was thoroughly summarized a few years ago by Szilard [2004] in his book. Gan et al. [2009] uses the smeared method in a wave propagation method to solve the natural frequencies of a ring-stiffened cylindrical shell. Bauchau and Craig

[2009] used smearing-out method for the analysis of real structural components including bars, beams, and plates. Particular attention is devoted to the analysis of thin-walled beams under bending, shearing, and torsion. Guyader et al. [2010] has recently proposed a related smearing technique for modeling multilayer structures. The disadvantage of smearing the stiffener properties is that it makes the solution of the plate or shell dynamics is a little more complicated than the uniform isotropic case. Luan et al. [2011] adopts the smeared method for cross-stiffened rectangular plates including various improvements to the technique used. Beyond pure smearing, Junger and Feit [1993] consider reaction forces on a plate due to just the translational and rotary inertia of regularly spaced stiffeners. When reinforced structure is large and with evenly spaced stiffeners, it can be considered how an infinite periodic structure. A limit for smeared-stiffener analysis is the lack of taking into account of structural periodicity results in a pass and stop bands of vibration transmission. Mace [1980] considers infinite fluid-loaded stiffened plates excited by line and point forces, giving general expressions for the stiffener reaction forces and moments and specific values for beam-like stiffeners. Langley [1989] uses the periodic method for a series of plates joined end to end with simply supported boundary conditions on two sides of each plate and a stiffener at the joints. Also, Langley [1989] talked about the use of a dynamic stiffness matrix for a single plate unit in assembling a structure with different stiffener spacing from a finite number of plate units. Another technique, based on Fourier decomposition and space-harmonic analysis, is used by Hodges et al. [1985] to model an infinitely long ring-stiffened cylindrical shell on which the cross-section of the symmetric stiffeners are subjected to distortion. Mead and Bardell [1986] investigate wave propagation in two different circular structures. In the first structure, the reinforcements are obtained using longitudinal stiffeners (stringers), while in the second structure the circumferential (ring) stiffeners are used to reinforce the component, as shown in Mead and Bardell [1987]. They allow for stiffeners of arbitrary cross-section. The advantage of this approach is the capability to assume periodicity in the circumferential or axial direction respectively and seeks propagation constants that are related to the wave types in the cylinder. In contrast, the mentioned approach can not consider axial and circumferential stiffeners together but one for a time. Lee and Kim [2002] apply a similar approach for sound transmission through a part of aircraft fuselage characterized by thin-walled cylindrical component reinforced with stiffeners. Each stiffener is treated as a lumped mass, including translational and rotational springs. Space harmonic expansions are used by Efimtsov and Lazarev [2009] to demonstrate a solution for periodically stiffened plates and shells. Also, the functions used are more suitable at high frequencies than the constant propagation method.

Another approach is based on the utilization of the Finite Element Method (FEM). In this case, the structure is modeled using different elements. Although different FEM approaches exist, they all share the common idea of discretizing a

mesh of a continuous domain into a set of discrete sub-domains, which are usually called elements. FEM was first introduced in the 1940s owing to the need to solve different problems related to elasticity and structural analysis in both the civil and aerospace industries. In the 1941 Hrennikoff [1941] wrote the first article on FEM applications, and a few years later, in 1943 Courant [1943] published some results about a simple square structure. In 1973 the mathematicians Strang and Fix [1973] contributed towards an improvement in FEM. The addition of stiffeners has a significant effect on the dynamic characteristics of a plate and is therefore of direct interest in structural designs. In 1969, Leissa [1969] studied the free vibration response of a rectangular plate with different geometries considering the effect of the boundary conditions on the modal parameters. In 1996, Rossi and Laura [1996] conducted research work related to the effect of Poisson′s ratio and the aspect ratio of the plate on the dynamic response. In 2010, Manzanares et al. [2010] studied the transverse vibration of a rectangular plate without constraints on the edge; they considered both theoretical and experimental studies.

1.3.1 1D and 2D elements coupling in FEM

One of the classical problems of FEM is the need for a large storage capacity and high computational power when large structures are considered. In particular, the solid elements, or 3D elements shown in Fig.4.4a, are very accurate because fundamental assumptions do not afflict their kinematics but, unfortunately, they require a large number of unknowns (degrees of freedoms, DOFs), and this leads to high computational costs. Overcoming the problem, a complex structure is made using a combination of plate/shell (2D) and beam (1D) elements. The use of 1D and 2D elements reduce the computational costs but also the accuracy of the solution. These models are based on classical structural theories: Euler [1744] or Timoshenko and Goodier [1951] in the one-dimensional case, and Kirchhoff [1850] and Love [1927] or Reissner [1945] and Mindlin [1951] in the two-dimensional case. Different works have been proposed for a proper simulation of the linkage between stiffeners and panel. Satsangi and Mukhopadhyay [1987] modeling assumes the same displacement field for both stiffeners and plates an 8-nodes plate is modeled. Kolli and Chandrashekhara [1996] developed an FE model where a laminated plate element with 45 degrees of freedom is used in conjunction with a laminated beam element having 12 degrees of freedom for the bending analysis of eccentrically stiffened laminated plates. Similarly, Gangadhara [2003] developed an eight-noded isoparametric shell element in association with three-noded curved beam element for the formulation of the stiffened panel element. In this application, first-order shear deformation theory is used. Recently, Thinh and Khoa [2008] have developed a new 9-node rectangular plate model to study the free vibrations of shell structures with arbitrarily oriented stiffeners. It is often necessary to model stiffeners

out of the plate/shell element plane. In this case, beam nodes are connected to the shell element nodes via rigid fictitious links. This methodology presents some inconsistencies. The main problem is that the out-of-plane warping displacements in the stiffener section are neglected, and the beam torsional rigidity is not correctly predicted. Several solutions have been proposed in the literature to overcome this issue.

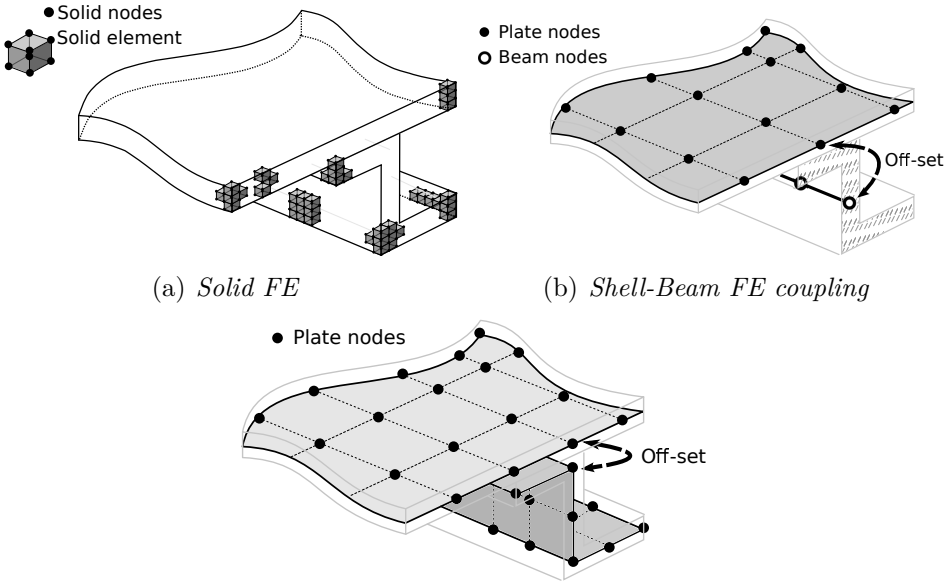

(a) *Solid FE* (b) *Shell-Beam FE coupling*

(c) *Shell FE modeling*

Figure 1.9. Different FE approaches to model reinforced components.

Patel et al. [2006] investigated on the static and dynamic instability characteristics of stiffened shell panels subjected to uniform in-plane harmonic edge loading. The eight-noded isoparametric degenerated shell element and a compatible three-noded curved beam element are used to model the shell panels and the stiffeners, respectively. To overestimate the torsional rigidity the formulation of degenerated beam element is used. Voŕoš [1988] proposed a procedure to model the connection between the plate/shell and the stiffener where the shear deformation of the beam is neglected, and the formulation of the stiffener is based on the well-known Vlasov [1961] theory. In Vörös 'method the stiffener element has two nodes with seven degrees of freedom per node. In the works of Buehrle et al. [2000b] and Durin et al. [2011a], the shell elements are usually used to discretize a plate, while beam elements are used for stringers, how shown in Fig.4.4a. Fig.4.4b shows the case where the 2D elements are also used for stringers, and Guanghui et al. [2006] and Ping et al. [2012] use this approach. The displacement compatibility between the beam and the stiffened element is obtained using a particular transformation, which included

torsional-bending coupling and the eccentricity of internal forces between the stiffener and the plate elements. Solid FE models are used to obtain a model where the kinematic is not affected by different limitation. Large computational costs characterize these FE models, and their use is limited when the model analyzed is a complex model. In the aerospace engineering field, the quality and the precision of the solution is needed, for these reasons that different value of correction factors are used to increase the security of the peoples. One of the first application of reduced space models in the FE analysis can be observed in 1976 when 1/8 scale models of the space-shuttle solid-boosters (SS-SB) is used to investigate the vibration characteristics of the SS-SB Leadbetter et al. [1976]. Two reduced models are used, an FE model is realized using only plate elements, while the second FE model is built using only beam elements. In 2000, the FE modeling is used for the validation of an aircraft fuselage structures Buehrle et al. [2000a]. In this case, the FE models of an isolated ring frame and longitudinal stringer are modeled using bar, beam, plate, and solid elements. In addition, a hybrid model combining beam and plate elements is used to minimize the number of DOFs. Recently, in 2011 two FE reduced models are used to characterize the dynamic behavior concerning pressure oscillation of the boosters for the Arian V Durin et al. [2011b]. The first FE model is realized using only beam elements, while the second FE model includes the shell, beam elements for the structure and solid elements for the fuel. One year late, to perform the dynamic behavior of solid propellant for the Arian V, a linear viscoelastic material is used with frequency dependent mechanical properties Merlette and Pagnacco [2012]. Two FE modelings for the propellant are used with shell and solid elements. Reduction models are very useful to analyze structures with different shapes. In this area, the Carrera Unified Formulation (CUF) has contributed to analyzing complex structures using refined structural theories able to provide accurate solutions with low computational costs.

1.4 Higher-order beam theories

In this thesis, different 1D beam theories have been developed to permit complex space structures to be analyzed. Two are the classical beam methods; the Euler-Bernoulli Euler [1744] theory does not account for transverse shear deformations, the Timoshenko [1921] method assumes a uniform shear distribution along the cross-section of the beam. These approaches are very useful when slender, solid section, homogeneous structures are subjected to bending. Despite, in the analysis of thin-walled structures, open section or complex cross-section, more accurate theory are needed to achieve sufficiently accurate results as shown by Novozhilov [1961]. The focus of many refined beam theories is to overcome the limitation of the classical beam modeling, to address issues such as warping effects and in-plane cross-section

deformation. Over the last century, various refined theories have permitted to overcoming the limit of the classical models. The refined models based on the Carrera Unified Formulation (CUF) developed by Carrera et al. [2011a] have presented the capability to overcome the limitation of the classical beam theory in static, buckling and free vibration analysis. Other methods are based on the Variational Asymptotic Method (VAM) developed by Yu et al. [2002] and on the Generalized Beam Theory (GBT) discussed by Silvestre [2002]. Kapania and Raciti [1989a] and Kapania and Raciti [1989b] introduced a general review of beam modeling considering not only static analysis but also buckling and free vibration analysis are taken into account. Stephen and Levinson [1979] developed the first formulation of a second-order theory by using the cross-sectional warping and transverse direct stress. Heyliger and Reddy [1988] worked on a third-order theory where a quadratic variation was used for the shear strain across the cross-section. Its refined version, with transverse normal stress components, was reported later by Soldatos and Elishakoff [1992]. Levinson [1981] and Rychter [1987] are the founders of the fourth-order beam theories. Bickford [1982] extended the fourth-order theory to the dynamic analysis. kant and Gupta [1988] proposed a higher order shear deformable beam model based on high order displacement model and incorporates a linear and quadratic variation of transverse normal strain and transverse shearing strain respectively through the beam thickness for static and free vibration analysis. Similarly, the high order theory is used by Marur and kant [1996] for the free vibration analysis of reinforced composite beams, and a few years later the vibrations of angle-ply laminated beams are studied by Marur and kant [2007]. Marur et al. [1997] provided an analytical solution to the natural frequency analysis of thick and thin composite beams by accurately describing the cross-section warping. Subramanian [2006] computes the free vibration analysis of laminated composite beams using two higher order displacement based on shear deformation theories including the finite elements modeling. In this case, a high order of in-plane and transverse displacements in the thickness coordinates of the beams, the zero transverse shear strain/stress conditions are satisfied at the top and bottom surfaces of the beam. Ganesan and Zabihollah [2007a] developed a high-order FE formulation where the stiffness coefficients of the tapered laminated beam are determined based on the stress and strain transformations and classical laminate theory. Ganesan and Zabihollah [2007b] shows different results on the free undamped vibration analysis of various types of tapered composite beams. Şimşek and Kocatuŕk [2007] used a third-order shear deformation theory to carry out the free vibration analysis of beams considering different boundary conditions.

1.5 Carrera Unified Formulation

This work is part of the framework of the Carrera Unified Formulation (CUF), which is a hierarchical theory allowing for the automatic and straightforward development of higher-order kinematics with no need of apriori assumptions. According to CUF, in fact, 3D problems are reduced to 2D or 1D ones in a unified manner, that is, by exploiting arbitrarily rich expansions of the unknown variables. In the structural mechanic's scenario, CUF was initially devoted to the development of refined plate and shell theories, as shown in the works of Carrera [2002] and Carrera [2003]. In recent works Carrera et al. [2011a], CUF has been extended to beam modeling very useful when slender body are analyzed how space vehicles are. Carrera et al. [2014a] shows the capability of the CUF model to provide accurate results reducing the computational costs. Thanks to the principal author Carrera a mathematical tool able to derive high-order models in compact form have been developed. The theoretical formulation and some applications can be found in the different works Carrera and Giunta [2010a], Carrera et al. [2010, 2011b, 2014b], Carrera and Giunta [2010b]. Carrera et al. [2013a] shows the capability of the present component-wise (CW) approach in the analysis of various structures. The CW models can model different structures with the help of a unique one-dimensional formulation. In the case of reinforced structures, this method permits to model both skins and stringers using the same 1D-formulation. The effectiveness of the CW approach is shown by Carrera et al. [2013a] for static analyses and by Carrera et al. [2013b] in the dynamic analyses of simple structures. In 2013, Giunta et al. [2013] performs the free vibration analysis of composite simple beam models using refined theory. Recently, Cavallo et al. [b] analyzed the problems due to the modeling of the area between skin and stringer in particular when the $1D/2D$ FE models are used to model the structures using a less expensive computational model. A significant breakthrough has meant that complex reinforced structures to be analyzed, isotropic curved panels and reinforced cylinder. In particular, Carrera et al. [2016] performs the static analysis of complex reinforced structures. At some way, Carrera et al. [2016] analyses complex reinforced structure using a refined one-dimensional model in free vibration analyses. An extension to complex reinforced structures allows to an isotropic launcher structures to be analyzed. Carrera et al. [2015] considers a launcher with the shape similar to the European launcher Arian V with a central body and two lateral boosters. The analysis of the effect due to the solid fuel consumption in an outline of the isotropic launcher structure permits to Carrera et al. to highlight the limit of the use of axial and radial solid fuel consumption. Cavallo et al. [a] carry out different analysis on composite space structures, highlighting the effects of composite materials and non-structural masses on the free vibration analysis.

Chapter 2

Preliminaries

This chapter aims to introduce the notations, the beam geometry and to define the displacement, stress, and strain vectors used in the present thesis. The geometrical strain-displacement relations, as well as the material constitutive equations, are addressed herein following the adopted notation.

2.1 Reference system and geometrical relations

The Cartesian coordinates is the reference system used in the present work, as shown in figure 2.1a

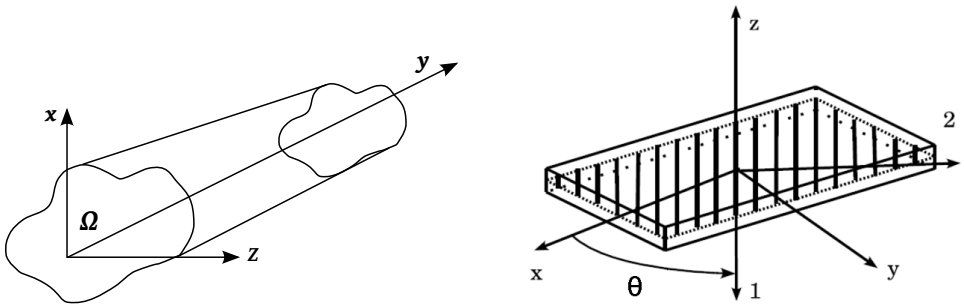

(a) *Cartesian coordinate system* (b) *Reference system rotation*

Figure 2.1. Global reference system.

u is the displacement vector with the following components:

$$\mathbf{u}^T(x,y,z) = \left\{ \begin{array}{ccc} u_x & u_y & u_z \end{array} \right\} \tag{2.1}$$

The superscript "T" denote transposition. Stresses are denoted using $\boldsymbol{\sigma}$, and the strains vector is written as $\boldsymbol{\varepsilon}$. Stresses and strain vector can be written in explicit

form as:

$$\boldsymbol{\sigma}^T = \left\{ \begin{array}{cccccc} \sigma_{xx} & \sigma_{yy} & \sigma_{zz} & \sigma_{xy} & \sigma_{xz} & \sigma_{yz} \end{array} \right\} \tag{2.2}$$

$$\boldsymbol{\epsilon}^T = \left\{ \begin{array}{cccccc} \epsilon_{xx} & \epsilon_{yy} & \epsilon_{zz} & \epsilon_{xy} & \epsilon_{xz} & \epsilon_{yz} \end{array} \right\} \tag{2.3}$$

The following geometrical equation links the displacement $\boldsymbol{u}$ and the strain vectors $\boldsymbol{\varepsilon}$, expressed in the linear form:

$$\begin{aligned} \varepsilon_{xx} = \frac{\partial u_x}{\partial x}; \quad \varepsilon_{xx} = \frac{\partial u_y}{\partial y}; \quad \varepsilon_{xx} = \frac{\partial u_z}{\partial z}; \\ \gamma_{xy} = \frac{\partial u_x}{\partial y} + \frac{\partial u_y}{\partial x}; \quad \gamma_{xz} = \frac{\partial u_x}{\partial z} + \frac{\partial u_z}{\partial x}; \quad \gamma_{yz} = \frac{\partial u_y}{\partial z} + \frac{\partial u_z}{\partial y}. \end{aligned} \tag{2.4}$$

Eq.2.4 can be written in compact form in according with the notation introduced in Eq.2.1 and Eq. 2.3, therefore the strain vector can be written as:

$$\boldsymbol{\varepsilon} = \boldsymbol{bu} \tag{2.5}$$

where matrix $\boldsymbol{b}$ is a differential operator. In explicit form, Eq. 2.5 becomes:

$$\left\{ \begin{array}{c} \varepsilon_{xx} \\ \varepsilon_{yy} \\ \varepsilon_{zz} \\ \gamma_{xz} \\ \gamma_{yz} \\ \gamma_{xy} \end{array} \right\} = \boldsymbol{bu} = \begin{bmatrix} \partial_x & 0 & 0 \\ 0 & \partial_y & 0 \\ 0 & 0 & \partial_z \\ \partial_z & 0 & \partial_x \\ 0 & \partial_z & \partial_y \\ \partial_y & \partial_x & 0 \end{bmatrix} \left\{ \begin{array}{c} u_x \\ u_y \\ u_z \end{array} \right\} \tag{2.6}$$

2.2 Equilibrium equations

The stress components above mentioned, in the equation 2.2 must fulfill the following differential equations:

$$\begin{aligned} \delta u_x : \frac{\partial \sigma_{xx}}{\partial x} + \frac{\partial \sigma_{xz}}{\partial z} + \frac{\partial \sigma_{xy}}{\partial y} = g_x \\ \delta u_y : \frac{\partial \sigma_{yy}}{\partial y} + \frac{\partial \sigma_{yz}}{\partial z} + \frac{\partial \sigma_{yx}}{\partial x} = g_y \\ \delta u_z : \frac{\partial \sigma_{zz}}{\partial z} + \frac{\partial \sigma_{zx}}{\partial x} + \frac{\partial \sigma_{zy}}{\partial y} = g_z \end{aligned} \tag{2.7}$$

where g_x, g_y and g_z are volume forces. These are the equilibrium equations by verified at each point.

2.3 Constitutive equations

The material properties can be used to derive the relations between stresses and strains. In this work, the materials properties are considered linear and therefore the Hooke's law is used. The stress can be expressed in term of strain using the following equation:

$$\boldsymbol{\sigma} = \boldsymbol{C}\boldsymbol{\varepsilon} \tag{2.8}$$

If the material is isotropic, matrix $\boldsymbol{C}$ can be written conventionally using Lamé's coefficients:

$$\boldsymbol{C} = \begin{bmatrix} \lambda+2G & \lambda & \lambda & 0 & 0 & 0 \\ \lambda & \lambda+2G & \lambda & 0 & 0 & 0 \\ \lambda & \lambda & \lambda+2G & 0 & 0 & 0 \\ 0 & 0 & 0 & G & 0 & 0 \\ 0 & 0 & 0 & 0 & G & 0 \\ 0 & 0 & 0 & 0 & 0 & G \end{bmatrix} \tag{2.9}$$

where

$$\lambda = \frac{E\nu}{(1+\nu)(1-2\nu)}, \quad G = \frac{E}{2(1+\nu)}. \tag{2.10}$$

If the material is orthotropic, matrix $\boldsymbol{C}$ can be written in the material reference system as:

$$\boldsymbol{C} = \begin{bmatrix} C_{11} & C_{12} & C_{13} & 0 & 0 & 0 \\ C_{21} & C_{22} & C_{23} & 0 & 0 & 0 \\ C_{31} & C_{32} & C_{33} & 0 & 0 & 0 \\ 0 & 0 & 0 & C_{44} & 0 & 0 \\ 0 & 0 & 0 & 0 & C_{55} & 0 \\ 0 & 0 & 0 & 0 & 0 & C_{66} \end{bmatrix} \tag{2.11}$$

The matrix $\boldsymbol{C}$ can be subjected to one or more rotation because $\boldsymbol{C}$ must be expressed in the global reference system.

Rotating the material only around $z - axis$, as shown in Fig. 2.1b, matrix $\boldsymbol{C}$ assumes the form:

$$\boldsymbol{C} = \begin{bmatrix} C_{11} & C_{12} & C_{13} & 0 & 0 & C_{16} \\ C_{21} & C_{22} & C_{23} & 0 & 0 & C_{26} \\ C_{31} & C_{32} & C_{33} & 0 & 0 & C_{36} \\ 0 & 0 & 0 & C_{44} & C_{45} & 0 \\ 0 & 0 & 0 & C_{54} & C_{55} & 0 \\ C_{61} & C_{62} & C_{63} & 0 & 0 & C_{66} \end{bmatrix} \tag{2.12}$$

The terms $C_{1,6}$, $C_{2,6}$ and $C_{3,6}$ can introduce a coupling between bending and in-plane phenomena. In other words, an in-plane forces can produce a moment.

Chapter 3

Governing equations

The governing equations for the Carrera Unified Formulation are derived using the Principle of Virtual Displacements (PVD). The equilibrium equations can be written in the compact form, called Fundamental Nucleus (FN). The advantages of using the FN is to derive any structural model 1D, 2D or 3D, using a unified notation, without the needs to a dedicated formulation.

3.1 Principle of Virtual Displacements

The Principle of Virtual Displacements is on of more method used to obtain various equations. In particular, the equations derived using the PVD are expressed in terms of displacements. In static case where there is not considered the term due to the inertial force, the PVD can write as follow:

$$\delta L_{int} = \delta L_{ext} \tag{3.1}$$

where L_{int} is the internal elastic work, L_{ext} is the work done by the external forces and δ indicates the virtual variation. The internal work can be expressed in explicit form as:

$$\delta L_{int} = \int_V \left(\sigma_{xx}\delta\varepsilon_{xx} + \sigma_{yy}\delta\varepsilon_{yy} + \sigma_{zz}\delta\varepsilon_{zz} + \sigma_{xz}\delta\varepsilon_{xz} + \sigma_{yx}\delta\varepsilon_{yz} + \sigma_{xy}\delta\varepsilon_{xy}\right) dV \tag{3.2}$$

The same equation can be written in compact form using the matrix formulation:

$$\delta L_{int} = \int_V \delta\boldsymbol{\varepsilon}^T \boldsymbol{\sigma} dV. \tag{3.3}$$

3.2 Governing equations in strong form

Considering a generic body, the external work can derive from four main contributions: volume forces, $\boldsymbol{g}$, on volume V, surface forces, $\boldsymbol{p}$, on surface S, the line forces

, $\boldsymbol{q}$, on the line l and the concentrated force, $\boldsymbol{P}$, at the point Q. The formulation of the external work, introduced in Chapter 2, becomes:

$$\delta L_{ext} = \int_V \delta \boldsymbol{u}^T \boldsymbol{g} dV + \int_S \boldsymbol{\delta u}^T \boldsymbol{p} dS + \int_L \boldsymbol{\delta u}^T \boldsymbol{q} dy + \boldsymbol{\delta u}^T|_Q \boldsymbol{P} \tag{3.4}$$

The relationship between the displacement vector $\boldsymbol{u}$ and the strain vector, $\boldsymbol{\varepsilon}$ is expressed by the geometrical relation:

$$\boldsymbol{\varepsilon} = \boldsymbol{b}\boldsymbol{u} \tag{3.5}$$

where matrix $\boldsymbol{b}$ is a differential operator. In explicit form, the equation becomes:

$$\begin{Bmatrix} \varepsilon_{xx} \\ \varepsilon_{yy} \\ \varepsilon_{zz} \\ \gamma_{xz} \\ \gamma_{yz} \\ \gamma_{xy} \end{Bmatrix} = \boldsymbol{b}\boldsymbol{u} = \begin{bmatrix} \partial_x & 0 & 0 \\ 0 & \partial_y & 0 \\ 0 & 0 & \partial_z \\ \partial_z & 0 & \partial_x \\ 0 & \partial_z & \partial_y \\ \partial_y & \partial_x & 0 \end{bmatrix} \begin{Bmatrix} u_x \\ u_y \\ u_z \end{Bmatrix} \tag{3.6}$$

The internal work can be written in terms of displacement,

$$\delta L_{int} = \int_V \delta(\boldsymbol{b}\boldsymbol{u})^T \boldsymbol{\sigma} dV \quad = \quad \int_V (\delta \boldsymbol{u}^T \boldsymbol{b}^T) \boldsymbol{\sigma} dV \tag{3.7}$$

It is is possible to move the differential operator from the displacement to the strains by integrating by parts [1],

$$\int_V (\delta \boldsymbol{u}^T \boldsymbol{b}^T) \boldsymbol{\sigma} dV = -\int_V \delta \boldsymbol{u}^T (\boldsymbol{b}^T \boldsymbol{\sigma}) dV + \int_S \delta \boldsymbol{u}^T (\boldsymbol{I_n}^T \boldsymbol{\sigma}) dS \tag{3.9}$$

In the first term of the right-hand side, operator $\boldsymbol{b}$ acts on the stress vector. The Principle of Virtual Displacements can be written as:

$$\begin{aligned} -\int_V \delta \boldsymbol{u}^T (\boldsymbol{b}^T \boldsymbol{\sigma}) dV + \int_S \delta \boldsymbol{u}^T (\boldsymbol{I_n}^T \boldsymbol{\sigma}) dS = \\ = \int_V \delta \boldsymbol{u}^T \boldsymbol{g} dV + \int_S \boldsymbol{\delta u}^T \boldsymbol{p} dS + \int_L \boldsymbol{\delta u}^T \boldsymbol{q} dy + \boldsymbol{\delta u}^T|_Q \boldsymbol{P} \end{aligned} \tag{3.10}$$

[1] Integration by parts on a volume integral can be expressed as:

$$\int_V (\delta \boldsymbol{u}^T \boldsymbol{D}^T) \boldsymbol{\sigma} dV = -\int_V \delta \boldsymbol{u}^T (\boldsymbol{D}^T \boldsymbol{\sigma}) dV + \int_S \delta \boldsymbol{u}^T (\boldsymbol{I_n}^T \boldsymbol{\sigma}) dS \tag{3.8}$$

where $\boldsymbol{I_n}$ is a matrix with the cosine directors. Farther details can be found in the book of Washizu [1968].

The equilibrium equation at a generic point P on volume V of a body are,

$$\delta \boldsymbol{u} : \quad -\boldsymbol{b}^T \boldsymbol{\sigma} = \boldsymbol{g} \tag{3.11}$$

From this equation, it is clear that the differential operator $\boldsymbol{b}$ must be the same for both the equilibrium and the geometrical equations.
The integrals on the surface give the boundary conditions, that can be expressed as

$$\delta \boldsymbol{u} : {\boldsymbol{I}_{\boldsymbol{n}}}^T \boldsymbol{\sigma} = \boldsymbol{p} \tag{3.12}$$

The equilibrium equations can be derived in explicit form by expanding Equation (3.11):

$$\begin{aligned} \delta u_x : &\frac{\partial \sigma_{xx}}{\partial x} + \frac{\partial \sigma_{xz}}{\partial z} + \frac{\partial \sigma_{xy}}{\partial y} = g_x \\ \delta u_y : &\frac{\partial \sigma_{yy}}{\partial y} + \frac{\partial \sigma_{yz}}{\partial z} + \frac{\partial \sigma_{yx}}{\partial x} = g_y \\ \delta u_z : &\frac{\partial \sigma_{zz}}{\partial z} + \frac{\partial \sigma_{zx}}{\partial x} + \frac{\partial \sigma_{zy}}{\partial y} = g_z \end{aligned} \tag{3.13}$$

At the some way the same procedure can be used for the boundary conditions, but this is omitted for the sake of brevity.
Hooke's law allows one to write the equilibrium equations in terms of displacements:

$$\delta \boldsymbol{u} : -\boldsymbol{b}^T \boldsymbol{C} \boldsymbol{b} \boldsymbol{u} = \boldsymbol{g} \tag{3.14}$$

Considering as isotropic material, matrix $\boldsymbol{C}$ can be written conventionally using Lamé's coefficients:

$$\boldsymbol{C} = \begin{bmatrix} \lambda + 2G & \lambda & \lambda & 0 & 0 & 0 \\ \lambda & \lambda + 2G & \lambda & 0 & 0 & 0 \\ \lambda & \lambda & \lambda + 2G & 0 & 0 & 0 \\ 0 & 0 & 0 & G & 0 & 0 \\ 0 & 0 & 0 & 0 & G & 0 \\ 0 & 0 & 0 & 0 & 0 & G \end{bmatrix} \tag{3.15}$$

where

$$\lambda = \frac{E\nu}{(1+\nu)(1-2\nu)}, \quad G = \frac{E}{2(1+\nu)}. \tag{3.16}$$

The equilibrium equations can be written, in strong form, using a matrix $\boldsymbol{k}$, which originates from the previous indicated matrix multiplication,

$$\delta \boldsymbol{u} : \quad \boldsymbol{k} \boldsymbol{u} = \boldsymbol{g} \tag{3.17}$$

where

$$\boldsymbol{k} = -\boldsymbol{b}^T \boldsymbol{C} \boldsymbol{b} \tag{3.18}$$

Referring only to isotropic and homogeneous materials, the matrix $\boldsymbol{C}$ is assumed to be constant in V. The matrix $\boldsymbol{k}$ is a 3×3 matrix, it contains 9 differential operators,

$$\boldsymbol{k} \quad = \quad \begin{bmatrix} k_{xx} & k_{xy} & k_{xz} \\ k_{yx} & k_{yy} & k_{yz} \\ k_{zx} & k_{zy} & k_{zz} \end{bmatrix} \tag{3.19}$$

which, in explicit form, becomes:

$$\begin{aligned}
k_{xx} &= -(\lambda + 2G)\ \partial_x\partial_x - G\ \partial_y\partial_y - G\ \partial_z\partial_z \\
k_{xy} &= -\lambda\ \partial_x\partial_y - G\ \partial_y\partial_x \\
k_{xz} &= -\lambda\ \partial_x\partial_z - G\ \partial_z\partial_x \\
k_{yx} &= -\lambda\ \partial_y\partial_x - G\ \partial_x\partial_y \\
k_{yy} &= -(\lambda + 2G)\ \partial_y\partial_y - G\ \partial_x\partial_x - G\ \partial_z\partial_z \\
k_{yz} &= -\lambda\ \partial_y\partial_z - G\ \partial_z\partial_y \\
k_{zx} &= -\lambda\ \partial_z\partial_x - G\ \partial_x\partial_z \\
k_{zy} &= -\lambda\ \partial_z\partial_y - G\ \partial_y\partial_z \\
k_{zz} &= -(\lambda + 2G)\ \partial_z\partial_z - G\ \partial_x\partial_x - G\ \partial_y\partial_y
\end{aligned} \tag{3.20}$$

The symbol ∂_y means partial derivatives respect y. In Equation (3.20) the derivatives appear in pairs since the first derivatives are due to virtual variation of the strains while the second is due to the stresses. Since in the strong form the displacements are continuous functions it is possible to state that

$$\partial_y\partial_x = \partial_x\partial_y = \partial_{yx}, \quad \partial_z\partial_x = \partial_x\partial_z = \partial_{zx}, \quad \partial_z\partial_y = \partial_y\partial_z = \partial_{zy} \tag{3.21}$$

therefore Equation (3.20) becomes

$$\begin{aligned}
k_{xx} &= -(\lambda + 2G)\ \partial_{xx} - G\ \partial_{yy} - G\ \partial_{zz} \\
k_{xy} &= -(\lambda + G)\ \partial_{xy} \\
k_{xz} &= -(\lambda + G)\ \partial_{xz} \\
k_{yx} &= -(\lambda + G)\ \partial_{yx} \\
k_{yy} &= -(\lambda + 2G)\ \partial_{yy} - G\ \partial_{xx} - G\ \partial_{zz} \\
k_{yz} &= -(\lambda + G)\ \partial_{yz} \\
k_{zx} &= -(\lambda + G)\ \partial_{zx} \\
k_{zy} &= -(\lambda + G)\ \partial_{zy} \\
k_{zz} &= -(\lambda + 2G)\ \partial_{zz} - G\ \partial_{xx} - G\ \partial_{yy}
\end{aligned} \tag{3.22}$$

Finally the equilibrium equations can be written in terms of displacements,

$$\begin{aligned}\delta u_x : &-(\lambda+2G)\left(\frac{\partial^2 u_x}{\partial x^2}\right) - G\left(\frac{\partial^2 u_z}{\partial y^2}+\frac{\partial^2 u_x}{\partial z^2}\right)+\\ &-(\lambda+G)\left(\frac{\partial^2 u_y}{\partial x\partial y}+\frac{\partial^2 u_z}{\partial x\partial z}\right)=g_x \qquad (3.23)\\ \delta u_y : &-(\lambda+2G)\left(\frac{\partial^2 u_y}{\partial y^2}\right) - G\left(\frac{\partial^2 u_y}{\partial x^2}+\frac{\partial^2 u_y}{\partial z^2}\right)+\\ &-(\lambda+G)\left(\frac{\partial^2 u_x}{\partial y\partial x}+\frac{\partial^2 u_z}{\partial y\partial z}\right)=g_y \qquad (3.24)\\ \delta u_z : &-(\lambda+2G)\left(\frac{\partial^2 u_z}{\partial z^2}\right) - G\left(\frac{\partial^2 u_z}{\partial x^2}+\frac{\partial^2 u_z}{\partial y^2}\right)+\\ &-(\lambda+G)\left(\frac{\partial^2 u_z}{\partial z\partial x}+\frac{\partial^2 u_y}{\partial z\partial y}\right)=g_z \qquad (3.25)\end{aligned}$$

3.2.1 Fundamental nucleus in strong form

Two of the nine terms in the matrix $\boldsymbol{k}$ have a different structure, as follows:

$$k_{xx} = -(\lambda+2G)\ \partial_{xx} - \lambda\ \partial_{zz} - \lambda\ \partial_{yy} \qquad (3.26)$$

$$k_{xy} = -\lambda\ \partial_{xy} - G\ \partial_{yx} \qquad (3.27)$$

It is evident that the other components of matrix $\boldsymbol{k}$ can be obtained in a similar form of the two previously terms. The terms k_{yy} and k_{zz} have the same form of k_{xx} because they are on the diagonal. The elements out of the diagonal come from a permutation of the indexes of k_{xy} in fact k_{xz}, k_{yz}, k_{yx}, k_{zx} and k_{zy} can be obtained by permuting the indexes in k_{xy}.

3.2.2 Extension to composite material

When the composite materials are used, all the nine terms of the fundamental nuclei must be considered:

$$
\begin{aligned}
k_{xx} =& \partial_x C_{11}\partial_x + \partial_y C_{61}\partial_x + \partial_z C_{44}\partial_z + \partial_x C_{16}\partial_y + \partial_y C_{66}\partial_y \\
k_{xy} =& \partial_x C_{12}\partial_y + \partial_y C_{62}\partial_y + \partial_z C_{45}\partial_z + \partial_x C_{16}\partial_x + \partial_y C_{66}\partial_x \\
k_{xz} =& \partial_x C_{13}\partial_z + \partial_y C_{63}\partial_z + \partial_z C_{44}\partial_x + \partial_z C_{45}\partial_y \\
k_{yx} =& \partial_y C_{21}\partial_y + \partial_x C_{61}\partial_y + \partial_z C_{54}\partial_z + \partial_y C_{26}\partial_y + \partial_x C_{66}\partial_y \\
k_{yy} =& \partial_y C_{22}\partial_y + \partial_x C_{62}\partial_y + \partial_z C_{55}\partial_z + \partial_y C_{26}\partial_x + \partial_x C_{66}\partial_x \\
k_{yz} =& \partial_y C_{23}\partial_z + \partial_y C_{13}\partial_z + \partial_z C_{54}\partial_x + \partial_z C_{55}\partial_y \\
k_{zx} =& \partial_z C_{31}\partial_x + \partial_x C_{44}\partial_z + \partial_y C_{45}\partial_z + \partial_z C_{36}\partial_y \\
k_{zy} =& \partial_z C_{32}\partial_y + \partial_x C_{45}\partial_z + \partial_y C_{55}\partial_z + \partial_z C_{36}\partial_x \\
k_{zz} =& \partial_z C_{33}\partial_z + \partial_x C_{44}\partial_x + \partial_y C_{54}\partial_x + \partial_x C_{45}\partial_y + \partial_y C_{55}\partial_y
\end{aligned}
\tag{3.28}
$$

These terms have to be written in explicit form because the material constants cannot be written concerning Lamé parameters. Also, they have a similar structure in the isotropic case.

3.3 Equilibrium equations in week form

When the equilibrium equations are expressed in term of displacements (see Eq.3.11), the solution of the elastic problem needs to define a displacement field able to fulfil the equilibrium equations in each point of the volume V of the body. Unluckily, the solution in close form of the equilibrium equations can be obtained only for simple geometries and boundary conditions. The weak form of these equations is needed to resolve complex problems.

The displacement in a generic three-dimensional field is:

$$
\boldsymbol{u}(x, y, z) = \Phi_i(x, y, z)\boldsymbol{u}_i \tag{3.29}
$$

Where $\Phi_i(x, y, z)$ is a generic set of interpolating shape functions and $\boldsymbol{u}_i$ represents the unknown coefficients. The choice of the interpolating functions $\Phi_i(x, y, z)$ makes it possible to kinematic assumption to be used to derive a structural model. Further details can be found on the book by Carrera et al. [2011a].

3.3.1 Displacement approximation

The introduction of the finite element approximation on the beam axis, $N_i(y)$, allows to the displacement field to be written as the sum of known functions multiplied by a constant.

According to the notation, i is the index used for the displacement:

$$\boldsymbol{u} = N_i \boldsymbol{u}_i \tag{3.30}$$

The virtual variation of the displacement can be written in the same form using index j,

$$\delta\boldsymbol{u} = N_j \delta\boldsymbol{u}_j \tag{3.31}$$

The strains and their virtual variations can also be written in this compact form,

$$\boldsymbol{\varepsilon} = \boldsymbol{b} N_i \boldsymbol{u}_i \tag{3.32}$$

$$\delta\boldsymbol{\varepsilon} = \boldsymbol{b} N_j \delta\boldsymbol{u}_j \tag{3.33}$$

In the same way, the stresses become

$$\boldsymbol{\sigma} = \boldsymbol{C}\boldsymbol{b} N_i \boldsymbol{u}_i \tag{3.34}$$

Indices i and j can vary according to the number of nodes of the element.

3.3.2 Classical Theories

Classical beam theories assume a linear distribution of the displacement u_y and a constant distribution of u_x and u_z. The displacement field above the beam cross-section is:

$$\begin{array}{lll} u_x = & u_{0x}\,(y) & \\ u_y = & u_{0y}\,(y) & +\theta\,(y)\,x \quad +\phi\,(y)\,z \\ u_z = & u_{0z}\,(y) & \end{array} \tag{3.35}$$

where u_{0x}, u_{0y}, u_{0z} are the displacements along the direction x, y and z respectively. At some way, the rotations around $z-$ and $x-$ axis are expressed by θ and ϕ angles. The transverse shear deformations ϵ_{xy} and ϵ_{yz} are neglected by the Euler-Bernoulli theory [Euler, 1744]. The related displacement field becomes:

$$\begin{array}{lll} u_x = & u_{0x}\,(y) & \\ u_y = & u_{0y}\,(y) & -u_{x,y}\,(y)\,x \quad -u_{z,y}\,(y)\,z \\ u_z = & u_{0z}\,(y) & \end{array} \tag{3.36}$$

The shear stress plays a significant role in various beam problems. By including the shear deformations ϵ_{xy} and ϵ_{yz}, the Eq.(3.35) represents the kinematic field of the Timoshenko theory [Timoshenko, 1921] which could also be written in the following form:

$$\begin{array}{lll} u_x = & u_{0x}\,(y) & \\ u_y = & u_{0y}\,(y) & +(\epsilon_{xy} - u_{x,y})\,x \quad +(\epsilon_{yz} - u_{z,y})\,z \\ u_z = & u_{0z}\,(y) & \end{array} \tag{3.37}$$

Eq.3.37 is equivalent to Eq.3.35 with the difference for the shear strains, ϵ_{xy} and ϵ_{yz}, and bending contributions, $u_{x,y}$ and $u_{z,y}$, because they are separate.
The Timoshenko model can not detect the out- and in-plane deformations and the bending/torsion coupling, both of which are relevant parameters to detect more complex deformations/stress state of the cross-section. However, the Timoshenko model provides a constant distribution of shear strain above the cross-section.

Refined Theories based on Taylor expansion

Various methods have been introduced to improve traditional beam models. The cross-section deformation can be detected by using of warping functions:

$$\begin{array}{lllllll} u_x = & u_{0x}\,(y) & & & & & \\ u_y = & u_{0y}\,(y) & +f\,(x)\,(\epsilon^o_{xy}) & -u_{x,y}\,x & +f\,(z)\,(\epsilon^o_{yz}) & -u_{z,y}\,z & \\ u_z = & u_{0z}\,(y) & & & & & \end{array} \tag{3.38}$$

where $f(x)$ and $f(z)$ are the warping functions and ϵ^o_{xy}, ϵ^o_{yz} are the transverse shear strains measured with respect to the beam reference axis. So far, Eq.(3.38) neglect the in-plane axial strains ϵ_{xx} and ϵ_{zz}. The use of classical theories (3.36), (3.37) and (3.38) can be too restrictive because they are based on some hypotheses.
The solution is to use higher order theories, such as Matsunaga's model, in which the displacement components are expressed as follows:

$$\begin{array}{ll} u_x = & 0 \\ u_y = & z^n\,u_{y_n} \\ u_z = & z^n\,u_{z_n} \end{array} \tag{3.39}$$

where the subscripts and superscripts indicate summation according to the generalized Einstein notation.
For a complete removal of the inconsistency, we should assume:

$$\mathbf{u} = x^m\,z^n\,\mathbf{u}_{(mn)}(y), \qquad m,n = 1,2,....,N \tag{3.40}$$

where $\mathbf{u}$ stands the displacement vector. The number of terms N needs to be chosen properly, and it is an input of the problem in the CUF; in fact, the hierarchical CUF model permits to change the order of the expansion N without the need to reform the theory but only changing the value of N. Variational statement could be used to write governing equations that permit the calculation of the introduced displacement variables $u_{x(mn)}$, $u_{y(mn)}$ and $u_{z(mn)}$. As Washizu pointed out [Washizu, 1968], the only sad thing about this method is a large number of related governing equations ($3N$). The Carrera Unified Formulation represents a possible avenue

to tackle this problem considering the displacement field as an N-order expansion regarding generic functions, F_τ:

$$\mathbf{u} = F_\tau(x,z)\mathbf{u}_\tau(y), \qquad \tau = 1,2,....,T \tag{3.41}$$

u_τ is the displacement vector and T stands for the number of terms of the expansion. Eq.(3.41) adopts the MacLaurin expansion using the 2D polynomials x^i and z^j as base (i and j are positive integers). Different terms of the MacLaurin expansion can be added changing simply the value of N and this procedure permits to include many terms from the Tartaglia'triangle for the evaluation of the displacement field. To be clear, the second-order displacement field is:

$$\begin{aligned} u_x &= u_{x_1} + x\ u_{x_2} + z\ u_{x_3} + x^2\ u_{x_4} + xz\ u_{x_5} + z^2\ u_{x_6} \\ u_y &= u_{y_1} + x\ u_{y_2} + z\ u_{y_3} + x^2\ u_{y_4} + xz\ u_{y_5} + z^2\ u_{y_6} \\ u_z &= u_{z_1} + x\ u_{z_2} + z\ u_{z_3} + x^2\ u_{z_4} + xz\ u_{z_5} + z^2\ u_{z_6} \end{aligned} \tag{3.42}$$

while the third-order displacement field becomes :

$$\begin{aligned} u_x &= u_{x_1} + x\ u_{x_2} + z\ u_{x_3} + x^2\ u_{x_4} + xz\ u_{x_5} + z^2\ u_{x_6} + x^3\ u_{x_7} + x^2z\ u_{x_8} + xz^2\ u_{x_9} + z^3\ u_{x_{10}} \\ u_y &= u_{y_1} + x\ u_{y_2} + z\ u_{y_3} + x^2\ u_{y_4} + xz\ u_{y_5} + z^2\ u_{y_6} + x^3\ u_{y_7} + x^2z\ u_{y_8} + xz^2\ u_{y_9} + z^3\ u_{y_{10}} \\ u_z &= u_{z_1} + x\ u_{z_2} + z\ u_{z_3} + x^2\ u_{z_4} + xz\ u_{z_5} + z^2\ u_{z_6} + x^3\ u_{z_7} + x^2z\ u_{z_8} + xz^2\ u_{z_9} + z^3\ u_{z_{10}} \end{aligned} \tag{3.43}$$

A remarkable feature is that classical beam theories are obtainable as particular cases of Taylor expansions. It should be noted that classical theories require reduced material stiffness coefficients to contrast Poisson's locking. Unless otherwise specified, for classical and first-order models Poisson's locking is corrected according to [Carrera et al., 2011a].

Advanced Theories based on Lagrange Expansions

LE models exploit Lagrange polynomials to build 1D higher-order theories. In this paper, one type of cross-section polynomial sets are adopted: nine-point elements, L9. The isoparametric formulation is exploited to deal with arbitrarily shaped geometries. Oñate [2009] gives the L9 interpolation functions:

$$\begin{aligned} F_\tau &= \tfrac{1}{4}(r^2 + r\ r_\tau)(s^2 + s\ s_\tau) \qquad \tau = 1,3,5,7 \\ F_\tau &= \tfrac{1}{2}s_\tau^2(s^2 - s\ s_\tau)(1-r^2) + \tfrac{1}{2}r_\tau^2(r^2 - r\ r_\tau)(1-s^2) \qquad \tau = 2,4,6,8 \\ F_\tau &= (1-r^2)(1-s^2) \qquad \tau = 9 \end{aligned} \tag{3.44}$$

Where r and s from -1 to $+1$. The displacement field given by an L9 element is:

$$\begin{aligned} u_x &= F_1\, u_{x_1} + F_2\, u_{x_2} + F_3\, u_{x_3} + F_4\, u_{x_4} + F_5\, u_{x_5} + F_6\, u_{x_6} + F_7\, u_{x_7} + F_8\, u_{x_8} + F_9\, u_{x_9} \\ u_y &= F_1\, u_{y_1} + F_2\, u_{y_2} + F_3\, u_{y_3} + F_4\, u_{y_4} + F_5\, u_{y_5} + F_6\, u_{y_6} + F_7\, u_{y_7} + F_8\, u_{y_8} + F_9\, u_{y_9} \\ u_z &= F_1\, u_{z_1} + F_2\, u_{z_2} + F_3\, u_{z_3} + F_4\, u_{z_4} + F_5\, u_{z_5} + F_6\, u_{z_6} + F_7\, u_{z_7} + F_8\, u_{z_8} + F_9\, u_{z_9} \end{aligned} \tag{3.45}$$

Where $u_{x_1}, ..., u_{z_9}$ are the displacement variables of the problem, and they represent the translational displacement components of each of the nine points of the L9 element, this means that LE models provide elements having displacement variables only.

3.3.3 FEM model

A classical Finite Element technique is adopted with the purpose of easily dealing with arbitrarily shaped cross-sections. The generalized displacement vector is given by:

$$\mathbf{u}_\tau(y) = N_i(y)\mathbf{q}_{\tau i} \tag{3.46}$$

where N_i are the shape functions and $\mathbf{q}_{\tau i}$ is the nodal displacement vector:

$$\mathbf{q}_{\tau i} = \left\{ \begin{array}{ccc} q_{u_{x_{\tau i}}} & q_{u_{y_{\tau i}}} & q_{u_{z_{\tau i}}} \end{array} \right\}^T \tag{3.47}$$

In the end the displacement field assumes the following form:

$$\mathbf{u}(x, y, z) = F_\tau(x, z)N_i(y)\mathbf{q}_{\tau i} \tag{3.48}$$

For the sake of brevity, the shape functions are not listed here. They can be found in the literature, for instance in [Bathe, 1996]. The theory order of the beam model is related to the expansion on the cross-section and it is not correlated with the number of nodes per element along the y axis. In other words, these two parameters are totally free and not related to each other. The stiffness matrix of the elements and the external loadings, which are consistent with the model, are obtained via the Principle of Virtual Displacements.

3.3.4 Fundamental nuclei

Stiffness matrix

The virtual variation of the internal work in compact form is

$$\delta L_{int} = \delta \boldsymbol{u}_{js} \left(\int_V N_j F_s \boldsymbol{b}^T \boldsymbol{C} \boldsymbol{b} N_i F_\tau dV \right) \boldsymbol{u}_{\tau i} \tag{3.49}$$

It is now possible to introduce the 3×3matrix $\boldsymbol{K}^{\tau sij}$,

$$\delta L_{int} = \delta \boldsymbol{u}_j \boldsymbol{K}^{\tau sij} \boldsymbol{u}_i \tag{3.50}$$

Matrix $\boldsymbol{k}^{\tau sij}$ is the fundamental nucleus of the stiffness matrix and is a 3×3 matrix, as shown in the following formula,

$$K^{\tau sij} = \int_V \Big[N_j \underbrace{\overbrace{\boldsymbol{b}^T}^{\left[\ 3 \times 6\ \right]} \overbrace{\left[\ 6 \times 6\ \right]}^{\boldsymbol{C}} \overbrace{\left[\ 6 \times 3\ \right]}^{\boldsymbol{b}}}_{\left[\ 3 \times 3\ \right]} N_i \Big] dV = \begin{bmatrix} k_{xx}^{\tau sij} & k_{xy}^{\tau sij} & k_{xz}^{\tau sij} \\ k_{yx}^{\tau sij} & k_{yy}^{\tau sij} & k_{yz}^{\tau sij} \\ k_{zx}^{\tau sij} & k_{zy}^{\tau sij} & k_{zz}^{\tau sij} \end{bmatrix} \tag{3.51}$$

In explicit form, the 9 terms are

$$\begin{aligned}
k_{xx}^{\tau sij} =& (\lambda + 2G) \int_V N_i N_j F_{\tau,x} F_{s,x} dV + G \int_V N_{i,y} N_{j,y} F_\tau F_s dV + G \int_V N_i N_j F_{\tau,z} F_{s,z} dV \\
k_{xy}^{\tau sij} =& \lambda \int_V N_{i,y} N_j F_\tau F_{s,x} dV + G \int_V N_i N_{j,y} F_{\tau,x} F_s dV \\
k_{xz}^{\tau sij} =& \lambda \int_V N_i N_j F_{\tau,z} F_{s,x} dV + G \int_V N_i N_j F_{\tau,x} F_{s,z} dV \\
k_{yx}^{\tau sij} =& \lambda \int_V N_i N_{j,y} F_{\tau,x} F_s dV + G \int_V N_{i,y} N_j F_\tau F_{s,x} dV \\
k_{yy}^{\tau sij} =& (\lambda + 2G) \int_V N_{i,y} N_{j,y} F_\tau F_s dV + G \int_V N_i N_j F_{\tau,x} F_{s,x} dV + G \int_V N_i N_j F_{\tau,z} F_{s,z} dV \\
k_{yz}^{\tau sij} =& \lambda \int_V N_i N_{j,y} F_{\tau,z} F_s dV + G \int_V N_{i,y} N_j F_\tau F_{s,z} dV \\
k_{zx}^{\tau sij} =& \lambda \int_V N_i N_j F_{\tau,x} F_{s,z} dV + G \int_V N_i N_j F_{\tau,z} F_{s,x} dV \\
k_{zy}^{\tau sij} =& \lambda \int_V N_{i,y} N_j F_\tau F_{s,z} dV + G \int_V N_i N_{j,y} F_{\tau,z} F_s dV \\
k_{zz}^{\tau sij} =& (\lambda + 2G) \int_V N_i N_j F_{\tau,z} F_{s,z} dV + G \int_V N_i N_j F_{\tau,x} F_{s,x} dV + G \int_V N_{i,y} N_{j,y} F_\tau F_s dV
\end{aligned} \tag{3.52}$$

Equation 3.52 can be easy compared to equation 3.2.2: This approach makes it possible to adopt the mathematical model in all the complex structural cases.

The fundamental nucleus has a “formal” invariant, it does not change with any change in the shape functions or the number of nodes in the element. It is easy to build the stiffness matrix using the fundamental nucleus. Figure 3.1 shows a graphical representation of the assembly procedure. The loops on indices i and

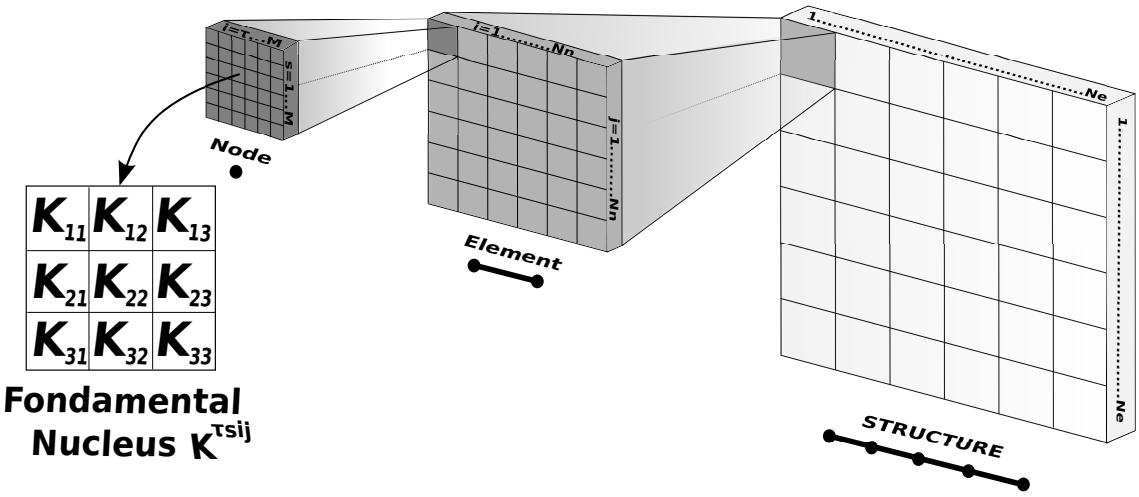

Figure 3.1. Assembly procedure of the stiffness matrix

j allow the matrix of the single element to be created. Different elements can be assembled in the classic FEM way by superimposing the stiffness of the shared nodes according to the PVD statements Equations (3.52) show clearly that FN of 1D FE, are the same of those of the weak form of 3D elasticity problems. If we compare the the strong form of the element k_{xx} with the same term in Equation (3.52) we have,

$$\begin{array}{rccccccc} k_{xx} = & -(\lambda+2G) & \partial_x \quad \partial_x & -G & \partial_y \quad \partial_y & -G & \partial_z \quad \partial_z \\ k_{xx}^{\tau sij} = & +(\lambda+2G) & \displaystyle\int_V N_i N_j F_{\tau,x} F_{s,x} dV & +G & \displaystyle\int_V N_{i,y} N_{j,y} F_\tau F_s dV & +G & \displaystyle\int_V N_i N_j F_{\tau,z} F_{s,z} dV \end{array} \tag{3.53}$$

The weak form of the FN can be easily derived from the strong form with few operations:

- move the derivative from the displacements to the shape functions, the second derivatives must be split in a derivative on the displacement and one on their virtual variation.
- the sign is opposite since there is no need of integrating by parts.

Mass matrix

The virtual variation of the inertial work, as well as the internal work, can be expressed in terms of displacements. If the displacements are expressed in compact formulation, the inertial work becomes

$$\delta L_{ine} = \delta \boldsymbol{u}_j \left(\int_V N_j F_s \boldsymbol{I} \rho \boldsymbol{I} F_\tau N_i dV \right) \ddot{\boldsymbol{u}}_i \tag{3.54}$$

The identity matrix $\boldsymbol{I}$ is introduced and the fundamental nucleus of the mass matrix is

$$\delta L_{ine} = \delta \boldsymbol{u}_{js} \boldsymbol{M}^{\tau sij} \ddot{\boldsymbol{u}}_{i\tau} \tag{3.55}$$

where

$$\boldsymbol{m}^{ij} = \int_V N_j \boldsymbol{I} \rho \boldsymbol{I} N_i dV \tag{3.56}$$

Matrix $\boldsymbol{m}^{ij}$ is a 3×3 matrix. It only has 3 elements on the diagonal that are not 0,

$$\begin{aligned} m_{xx}^{\tau sij} &= \int_V N_j F_s \rho N_i F_\tau dV \\ m_{yy}^{\tau sij} &= \int_V N_j F_s \rho N_i F_\tau dV \\ m_{zz}^{\tau sij} &= \int_V N_j F_s \rho N_i F_\tau dV \end{aligned} \tag{3.57}$$

While the elements outside the diagonal are null,

$$m_{yz}^{\tau sij} = m_{zx}^{\tau sij} = m_{zy}^{\tau sij} = m_{xy}^{\tau sij} = m_{xz}^{\tau sij} = m_{yx}^{\tau sij} = 0 \tag{3.58}$$

The assembly of the global mass matrix follows the same rules as those of the stiffness matrix. The loops on the indices i and j give the mass matrix of the elements. The mass matrix of the structure can be assembled by superimposing the masses of the shared nodes.

Loading vector

The loading vector can be derived using the formulation of the virtual variation of the external work. The virtual variation of the displacements in Equation (3.34) can be used to express the virtual variation of the external work in the CUF framework. The virtual variation of the external work can be written as:

$$\delta L_{ext} = \int_V \delta \boldsymbol{u}^T \boldsymbol{g} dV + \int_S \boldsymbol{\delta u}^T \boldsymbol{p} dS + \int_L \boldsymbol{\delta u}^T \boldsymbol{q} dy + \boldsymbol{\delta u}_j^T \boldsymbol{P} \tag{3.59}$$

were $\boldsymbol{g}$ are the volume forces, $\boldsymbol{p}$ are the surface forces, $\boldsymbol{q}$ are the line forces and P are the concentrated loads. The external loads are usually applied as surface loads (a pressure), or as a concentrated load.

Each contribution of the external load can be written in the indicial form. The volume loads become

$$\delta L_{ext} = \int_V \delta \boldsymbol{u}^T \boldsymbol{g} dV = \delta \boldsymbol{u}_{js}^T \int_V N_j F_s \boldsymbol{g} dV \tag{3.60}$$

The surface load are

$$\delta L_{ext} = \int_S \delta \boldsymbol{u}^T \boldsymbol{p} dS = \delta \boldsymbol{u}_{js}^T \int_S N_j F_s \boldsymbol{p} dS \tag{3.61}$$

The line loads becomes

$$\delta L_{ext} = \int_l \delta \boldsymbol{u}^T \boldsymbol{q} dl = \delta \boldsymbol{u}_{js}^T \int_l N_j F_s \boldsymbol{q} dl \tag{3.62}$$

Where l is the line where the load is applied. Finally the concentrated loads are

$$\delta L_{ext} = \delta \boldsymbol{u}^T P = \delta \boldsymbol{u}_{js}^T N_j F_s P \tag{3.63}$$

The load vector can be written as the sum of the previous contributions

$$\boldsymbol{P}^{sj} = \int_V N_j F_s \boldsymbol{g} dV + \int_S N_j F_s \boldsymbol{p} dS + \int_l N_j F_s \boldsymbol{q} dl + N_j F_s P \tag{3.64}$$

The load vector of the element can be assembled following the same procedure that was introduced for the stiffness matrix. In this case, only a loop on j and s gives the load vector of the element. The global vector can be derived by summing the loads in the shared nodes.

3.3.5 Load Factor

When using classical beam theories, translational as well as rotational load factors are usually applied on the reference axis - or on the shear axis if transverse stresses are also included. Let the following acceleration field be applied to the structure:

$$\ddot{\mathbf{u}}_0(x, y, z) = \{\ddot{u}_{x_0} \quad \ddot{u}_{y_0} \quad \ddot{u}_{z_0}\}^T \tag{3.65}$$

The virtual variation of the external work, δL_{ext}, due to the acceleration field $\ddot{\mathbf{u}}_0$ is given by

$$\delta L_{ext} = \int_V \rho \delta \mathbf{u}^T \ddot{\mathbf{u}}_0 dV \tag{3.66}$$

where ρ is the density of the material. By substituting the Eq.3.48 into the Eq.3.66, the external work in compact form becomes:

$$\delta L_{ext} = \delta \mathbf{q}_{\tau i}^T \mathbf{M}^{ij} \ddot{\mathbf{q}}_{sj_0} = \delta \mathbf{q}_{\tau i}^T \mathbf{P}_{ine}^{i\tau} \tag{3.67}$$

where $\mathbf{P}_{ine}^{i\tau}$ is the nucleus of the loading vector due to the acceleration field.

3.3.6 Localized Inertia

In the present thesis, the effect due to non-structural masses is also investigated. The effect of non-structural masses is included to investigate the effects of fuel consumption, and also the effect of lumped mass on the dynamic behavior of reinforced structures. Non-structural masses can be arbitrarily located in the 3D domain of

the beam structure. In the framework of the Carrera Unified Formulation, this is realized by adding the following term to the fundamental nucleus of the mass matrix, as shown in Pagani et al. [2014]:

$$\mathbf{m}^{ij\tau s} = \mathbf{I}\left[F_\tau(x_m, z_m)F_s(x_m, z_m)N_i(y_m)N_j(y_m)\right]\widetilde{m} \tag{3.68}$$

where $\mathbf{I}$ is the 3×3 identity matrix, while $\widetilde{m}$ represents the non-structural mass placed at the point (x_m,y_m,z_m).

Chapter 4

Classical and refined approaches to model reinforced structures

A reinforced structure is a thin structure reinforced using different reinforcements, longitudinal or stringers, and transversal or ribs as shown in Fig.4.1. Various approaches can be adopted to model the component and to investigate the local effect at the interface between skin and stringer.

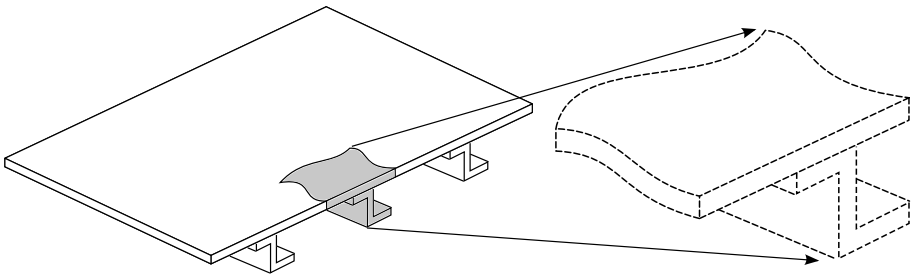

Figure 4.1. Reinforced structure example

4.1 Classical modelling methods

In the classical finite element (FE) modelling, reinforced structures can be made using different approaches based on the use of various finite elements, 3D, 2D or 1D.

Solid or 3D models

The first way to model a reinforced structure is based on the use of the *solid* o 3D elements. A structural component can be considered a solid body when their characteristics lengths along three different directions have the same order of magnitude,

see Fig.4.2. This approach can be considered the best choose to obtain accurate

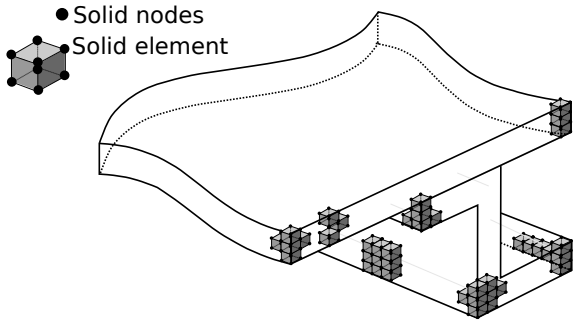

Figure 4.2. Solid or 3D model

results because fundamental assumptions do not afflict the kinematics of the 3D element, unfortunately, they require a large number of unknowns (degrees of freedoms, DOFs), and this leads to high computational costs. This side effect is due to the need to introduce several solid elements along the thin- thickness, thus requiring the needed for the use of a high number of solid elements for all the model because the quality of the Jacobian matrix depends on the value of the ratio between the three dimension of each solid element.

The use of 2D and 1D finite elements is required to reduce the computational costs than the 3D case.

Plate/Shell or 2D models

The use of 2D models allows the computational costs to be reduced. These models, in fact, introduce some approximations on the kinematic model (see Timoshenko [1921] and Mindlin [1951]).

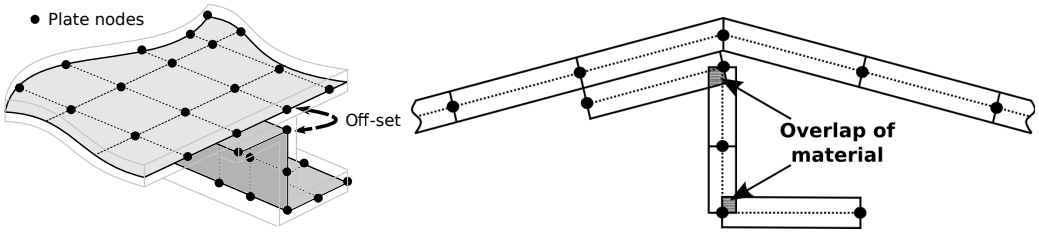

(a) *Layout for the 2D model.* (b) *2D deformed structure.*

Figure 4.3. Overlapping of the plate/shell elements

A reinforced structure can be modelled using the 2D elements; in this case, the first step consists in the identification of the middle surface of the skin, where, different plate elements are located using a constant thickness. Also, the reinforcements

can be modelled using the 2D elements, for this reason, that they are called simply *2D models*. This kind of model may present some geometrical overlapping of the elements, as shown in Fig.4.3b. Also, the continuity of the displacements is guaranteed only at the nodes, that is the interface between the skin and the reinforcement can not be studied in detail. The use offset can reduce this problem, but this requires a great effort in the modelling face.

Shell-Beam or 2D-1D models

Another approach consists in the use of plate/shell elements for the skin and beam elements for the stringer, as shown in Fig.4.4. This method is useful because the stringer can be considered as a beam element.

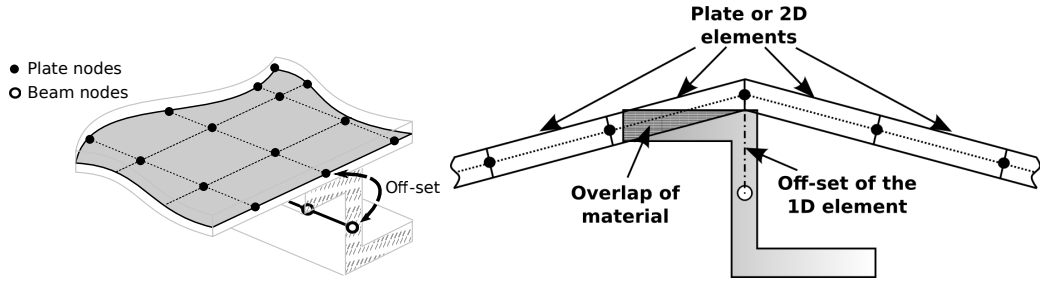

(a) *Layout for the 2D-1D model.* (b) *2D-1D deformed structure.*

Figure 4.4. Overlapping of the plate-beam elements

As in the case of the full two-dimensional model, also when a mixed one- and two-dimensional model has considered the connection between beam and plate elements requires the use of an offset value able to translate the reference axis of the beam. Moreover, in this case, the cross-section is completely neglected, and it is described only using the momentum of inertia. Also, the kinematic assumptions used by the classical beam model do not allow any deformation of the cross-section (see Fig.4.4b). This approach does not permit the interface between the skin and the stringer to be modelled correctly, that is, all the details of the connection can be missed.

4.2 Component-Wise approach as alternative to the classical FE models

The new approach, called component-wise approach, makes it possible to model each element alone. The cross-section is obtained attacking together all components, as Fig.4.5 shows. The skin and the stringer can be made using a unique 1D formulation. The advantage to using the same kinematic model for both skin and stringer allows

the mathematical inconsistency between skin and stringer to be removed, as happens when the 2D and 1D FEs are used to model a reinforced structure. When the structure is deformed, the present 1D-CUF model is not afflicted by the overlap of material. Its kinematic is similar to the 3D kinematic but with the advantage to using fewer elements along the beam axis reducing the DOFs. This modelling approach can be applied thanks to the use of two different expansion functions, one expansion function along the y-axis (or beam axis) and one expansion function on the cross-section, removing the problem with the Jacobian matrix.

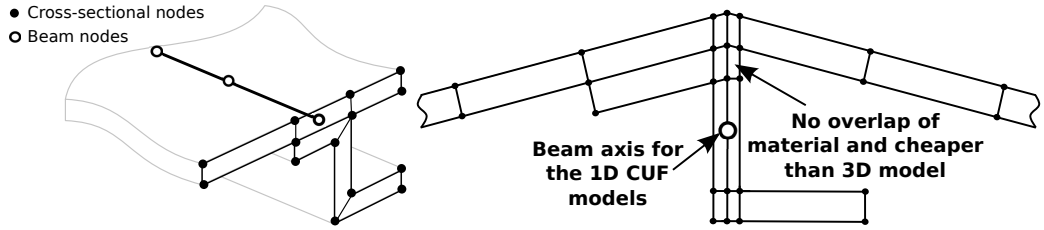

(a) *Layout for the 1D-CUF model.* (b) *1D-CUF deformed structure.*

Figure 4.5. 1D-CUF model as the 3D model but cheaper

For the sake of simplicity, in Fig.4.5 the structure proposed in Fig.4.1 is modelled using on the cross-section 4-node elements, some of them for the panel, and other for the stiffener. However various approaches can be adopted to model the displacement field on the cross-section, as will be shown following. The approximation of the kinematic can be increased locally using a more refined mesh. This approach allows an high-fidelity description of the geometry to be obtained. Both compact and thin-walled stiffeners can be analysed.

In the following, this refined 1D model is used to analyze simple and curved reinforced panels, investigating the effect introduced at the interface between skin and stringer, in the static and dynamic analysis, also highlighting the limit and the advantages of each model. Then, the model is extended to the analysis of complex reinforced structure, cylindrical components and launchers.

Chapter 5

One-dimensional refined models assessment

5.1 Convergence Analyses of a reinforced panel

This section investigates the behavior of the previously introduced FE models in the analysis of the reinforced structures. The chapter presents a convergence analysis of a refined one-dimensional model, named LE model because the kinematics is based on the Lagrange Expansion. The model considered is a square plate reinforced using three longitudinal stringers, as shown in Fig.5.1. In particular, the convergence analysis concerns the number of $B4$ beam elements on the $y - axis$, and than the cross-sectional discretization is improved changing the number of LE elements between two stringers but with a fixed number of beam elements. The comparison between Taylor and Lagrange Expansion functions is also estimated.

If not otherwise stated, the material used is an aluminum alloy, with a Young modulus, E, equal to 75 GPa, a Poisson ratio, ν, equal to 0.3 and a density value, ρ, equal to 2700 $\frac{kg}{m^3}$.

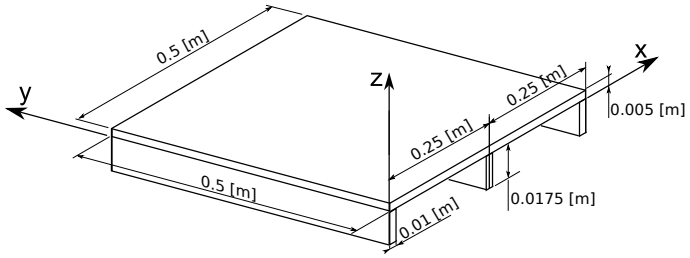

Figure 5.1. Geometrical Properties for the flat plate.

5.1.1 The effect of the number of beam elements

The effect of the number of $B4$ elements along the $y-axis$ is investigated in this section. Two 9-points LE elements are used between the stringers. The cross-section is realized using 10-LE elements, as shown in Fig.5.2.

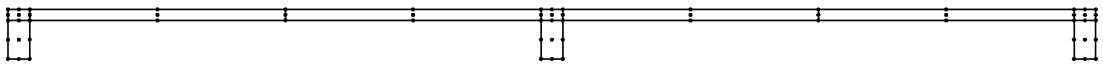

Figure 5.2. Mesh and nodes distribution for the reinforce panel cross-section.

The number of structural nodes N_n on the $y-axis$ depends on the number of $B4$ beam elements used.

$$N_n = (N_e * K) - (N_e - 1) \tag{5.1}$$

where, N_n is the total number of structural nodes, N_e is the number of $B4$ elements, and K depends on the number of nodes of each beam element. In the case of a $B4$ beam model, K is equal to 4.

Fig.5.3 shows the effect on the frequencies due to the number of $B4$ beam elements used to discretize the structure along the y-direction. For the sake of brevity, the model with 2 $B4$ elements is called the $2-B4$ model; the same acronym is also used for the other models. The $6-B4$ model is used as the reference solution. The first 10 modes are considered, and MAC^2 is used to compare the results, as shown in Fig.5.4. The Modal Assurance Criterion (MAC), is defined as a scalar number that represents the degree of consistency between two vectors (see Allemang and Brown [1982]):

$$MAC_{ij} = \frac{\left|\{\phi_{A_i}\}^T\{\phi_{B_j}\}\right|^2}{\{\phi_{A_i}\}^T\{\phi_{A_i}\}\{\phi_{B_j}\}\{\phi_{B_j}\}^T} \tag{5.2}$$

where, $\{\phi_{A_i}\}$ is the i^{th}-eigenvector of model A, while $\left\{\phi_{B_j}\right\}$ is the j^{th}-eigenvector of model B. MAC can range from zero (when two modes are completely different) to 1 (when the maximum correspondence between two modes is achieved). Different tonalities of gray appear when two modes correspond only partially.

Fig.5.4a shows that the model is not able to find mode 8 or mode 10 when only $2-B4$ elements are used. The difference, with respect to the $6-B4$ model, reaches 5% for mode 9.

Tab.5.1 shows at least 4 $B4$ elements are necessary to obtain an error below 1% for all 10 modes. For this reason, the $5-B4$ model is considered the best choose between computational costs and accuracy.

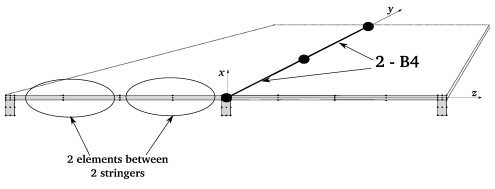

(a) *2-B4 elments on the $y-axis$*

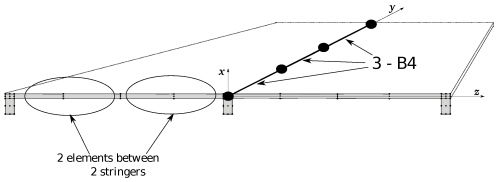

(b) *3-B4 elments on the $y-axis$*

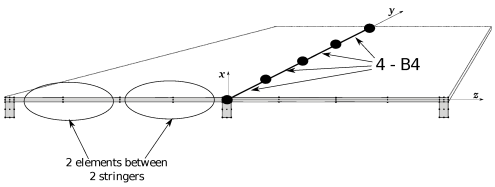

(c) *4-B4 elments on the $y-axis$*

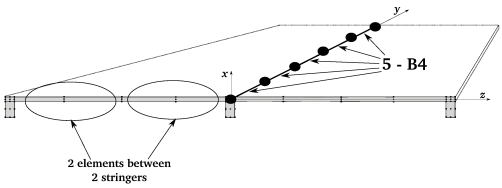

(d) *5-B4 elments on the $y-axis$*

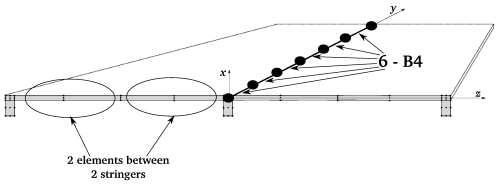

(e) *6-B4 elments on the $y-axis$*

Figure 5.3. Analysis using different number of $B4$ elements on the $y-axis$.

Freq [Hz]	6-$B4$	5-$B4$	4-$B4$	3-$B4$	2-$B4$
DOF	3591	3024	2457	1890	1323
1	298.8	299.3 $^{(+0.2\%)}$	300.2 $^{(+0.5\%)}$	301.8 $^{(+1.0\%)}$	305.8 $^{(+2.3\%)}$
2	308.3	308.7 $^{(+0.1\%)}$	309.3 $^{(+0.3\%)}$	310.3 $^{(+0.6\%)}$	313.0 $^{(+1.5\%)}$
3	478.2	479.0 $^{(+0.2\%)}$	480.3 $^{(+0.4\%)}$	482.6 $^{(+0.9\%)}$	488.1 $^{(+2.1\%)}$
4	589.1	589.9 $^{(+0.1\%)}$	591.1 $^{(+0.3\%)}$	593.4 $^{(+0.7\%)}$	599.6 $^{(+1.8\%)}$
5	601.6	602.3 $^{(+0.1\%)}$	603.6 $^{(+0.3\%)}$	606.3 $^{(+0.8\%)}$	627.4 $^{(+4.3\%)}$
6	678.3	679.4 $^{(+0.2\%)}$	681.3 $^{(+0.4\%)}$	685.6 $^{(+1.1\%)}$	711.3 $^{(+4.9\%)}$
7	906.9	907.7 $^{(+0.1\%)}$	909.9 $^{(+0.3\%)}$	912.4 $^{(+0.6\%)}$	923.6 $^{(+1.8\%)}$
8	954.9	956.6 $^{(+0.2\%)}$	959.9 $^{(+0.5\%)}$	980.3 $^{(+2.7\%)}$	**
9	1047.0	1048.9$^{(+0.2\%)}$	1052.2$^{(+0.5\%)}$	1059.6$^{(+1.2\%)}$	1099.4$^{(+5.0\%)}$
10	1093.9	1096.0$^{(+0.2\%)}$	1099.9$^{(+0.5\%)}$	1121.5$^{(+2.5\%)}$	**

$(\ )^{(*\%)}$: $*$ *percentage different with respect to* $6-B4$ *configuration*

$**$: *Modal shape not expected in model*

Table 5.1. First 10 frequencies using different number of $B4$ elements.

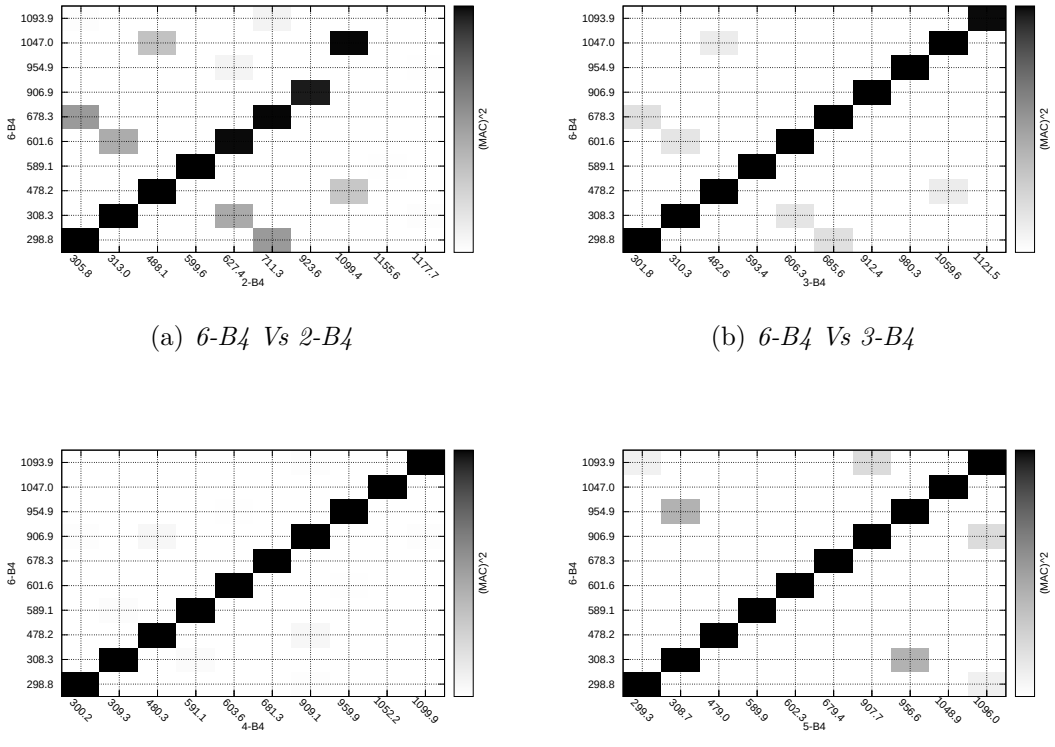

(a) *6-B4 Vs 2-B4*

(b) *6-B4 Vs 3-B4*

(c) *6-B4 Vs 4-B4*

(d) *6-B4 Vs 5-B4*

Figure 5.4. MAC considering different number of elements on the $y - axis$.

Fig.5.5 shows the behavior of the first 10 frequencies. The $2 - B4$ model is not able to find modes 8 and 10 as predicted. This aspect is highlighted on Fig.5.6 because the line is discontinuous. Fig.5.7 shows how increasing the number of $B4$ elements, the error decreases, and it is below 0.5% when $5 - B4$ elements are used.

5.1.2 The effect of the cross-sectional discretization

According to the previously chapter, 5 $B4$ beam elements make it possible to obtain the nearest to the reference one. The goal of this section in investigates the effect on the solution introduced by the number of LE elements used to model the cross-section. In fact, the solution also depends on the number of elements between two stringers. Fig.5.8 shows different configurations obtained changing the number of LE elements between two stringers. The number of $B4$ elements is now fixed to five. The model with 2 LE elements between two stringers is called $2 - Elem$, and

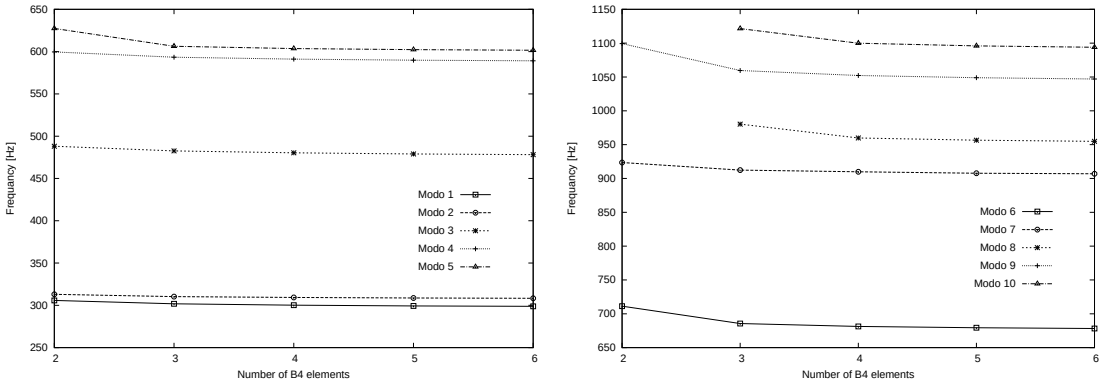

(a) *Form frequencies 1 to 5* (b) *Form frequencies 6 to 10*

Figure 5.5. Convergence behaviour using different beam elements.

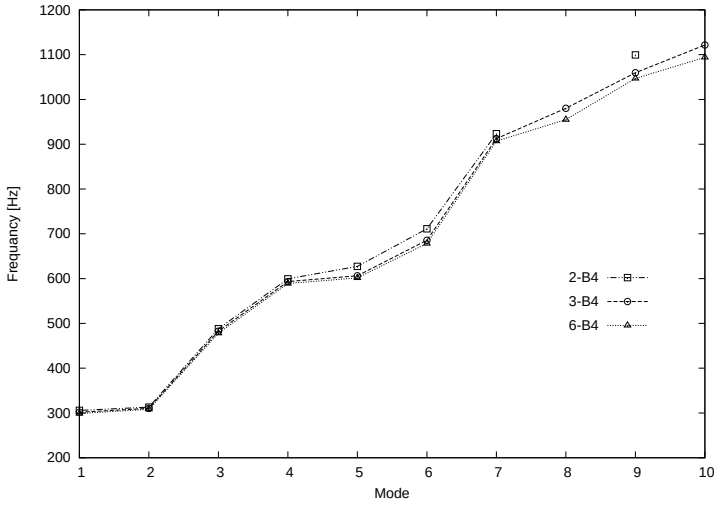

Figure 5.6. Behaviour of the frequencies with respect to the modes.

so on. The reference model is shown in Fig.5.8e, where 6 LE elements are used between the two stringers. The quality of the solution improves when the number of LE elements increase. The percentage difference, on the reference model, is about 20% when only 2 LE elements are used for modes 6, 7 and 9 as can be observed in Tab.5.2. Only 5 LE elements are necessary to make it possible to obtain an error of less than 1%. Fig.5.9 shows that if more than two LE elements are used, a linear matching takes place between the considered modes, but this is not the case for the $2-Elem$ model, as can be seen in Fig.5.9a. Fig.5.10 shows the behavior of the first ten modes when the number of LE elements is increased. The first four modes show an almost linear behavior, but the first three modes are simple modes, as shown in Fig.5.11a,b,c, while mode 4 is a very complex, shell-like mode. The 1D CUF model

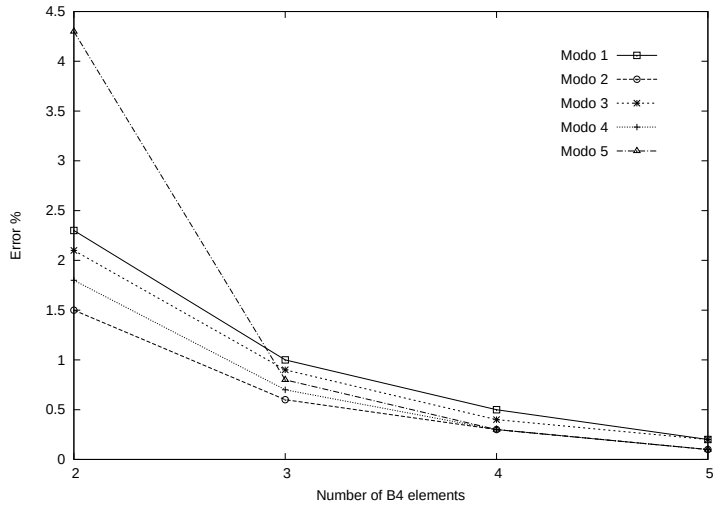

Figure 5.7. Percentage difference with respect to the model with $6 - B4$ elements.

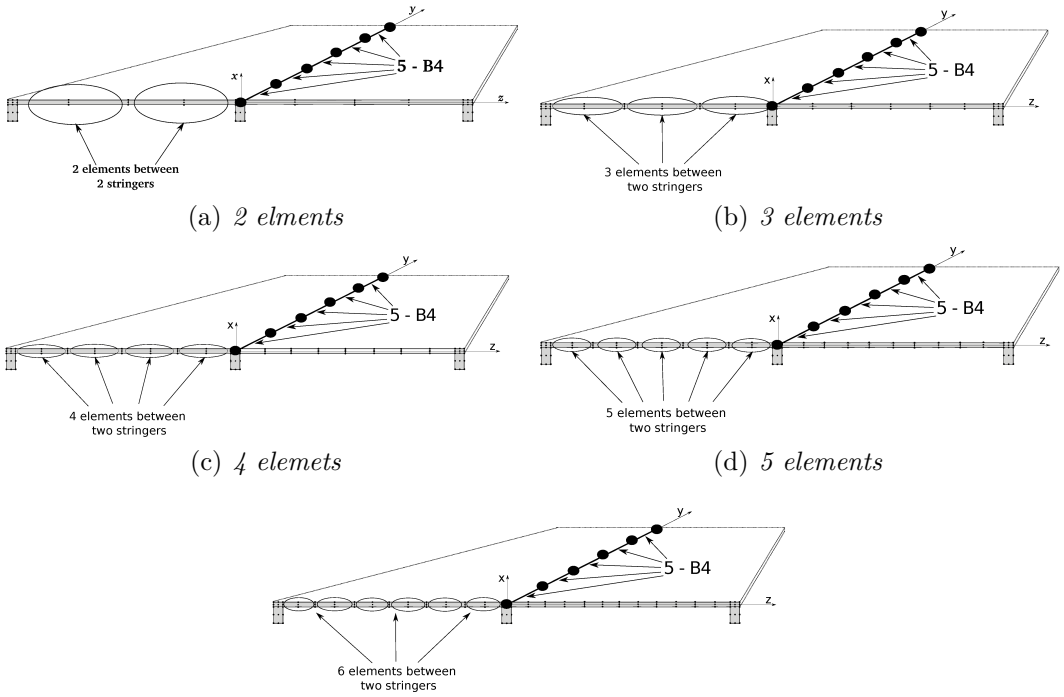

(a) *2 elments* (b) *3 elements*

(c) *4 elemets* (d) *5 elements*

(e) *6 elements*

Figure 5.8. Various mesh using different LE elements between two stringers.

provide a good solution for typical shell modes, which are called shell-like modes, where the deformation of the plate does not follow the classical beam deformation (bending and torsional deformations). Fig.5.11 shows more shell-like modes found

Freq[Hz]	$6Elem$	$5Elem$	$4Elem$	$3Elem$	$2Elem$
DOF	5328	4752	4176	3600	3024
1	282.6	283.6 (+0.4%)	285.4 (+1.0%)	289.3 (+2.4%)	299.3 (+5.9%)
2	292.3	293.3 (+0.3%)	295.0 (+0.9%)	298.7 (+2.2%)	308.7 (+5.6%)
3	472.4	473.2 (+0.2%)	474.7 (+0.5%)	477.2 (+1.0%)	479.0 (+1.4%)
4	549.8	552.2 (+0.4%)	556.7 (+1.3%)	567.0 (+3.1%)	567.0 (+3.1%)
5	563.3	565.0 (+0.3%)	567.9 (+0.8%)	573.8 (+1.9%)	602.3 (+6.9%)
6	574.0	578.2 (+0.7%)	586.3 (+2.1%)	605.7 (+5.5%)	679.4 (+18.4%)
7	756.5	762.0 (+0.7%)	772.4 (+2.1%)	797.1 (+5.4%)	907.7 (+20.0%)
8	870.4	873.8 (+0.4%)	880.1 (+1.1%)	895.3 (+2.9%)	956.6 (+9.9%)
9	898.1	903.9 (+0.6%)	915.4 (+1.9%)	944.6 (+5.2%)	1096.0 (+22.0%)
10	1013.4	1021.7(+0.8%)	1035.8(+2.2%)	1058.7 (+4.5%)	1048.9 (+3.5%)

$(\ )^{(*\%)}$: $*$ *percentage different with respect to the* $6-Elem$ *model.*

Table 5.2. First 10 frequencies using various mesh on the cross-section.

using the LE models. The error for the first four modes, including the case with only two LE elements between the two stringers, is under 5% (see Fig.5.12). If the number of LE elements increases, the solution converges to the reference solution for modes 6 to 10 and using three LE elements, the error decreases rapidly by about 15%, as shown in Fig.5.12. However, the error is less than 1% for all of the modes considered when only 5 LE elements are used, as shown in Tab.5.2.

The minimum number of beam elements along the $y-axis$ must be at least 5, and in the same way, the minimum number of LE elements between two stringers must be at least 5 to ensure an error of less the 1%.

5.1.3 Variable kinematic models: LE vs TE

This part is focused on the effects of the choice of the expansion function over the cross-section. Using TE expansion function different order are considered while using LE model, different meshes over the cross-section are taken into account. For the models, $5-B4$ are used along with the beam axis. Concerning LE models, the analysis is conducted by increasing the number of LE elements between the stringers. In this case, the notation used is $LE-(N)E$, where N represents the number of LE elements. In the case of the TE models, the convergence is investigated with an increasing order of expansion. $TE(N)$ denotes a model of order N, and $EULE$ denotes the Euler-Bernoulli model. Table 5.3 shows the first five frequencies evaluated using different models. The reference solution is obtained using a full 3D FEM model from the commercial $NASTRAN$ code. The results show that the TE models require a very low number of DOFs but, a sixth order model, $TE6$, still does

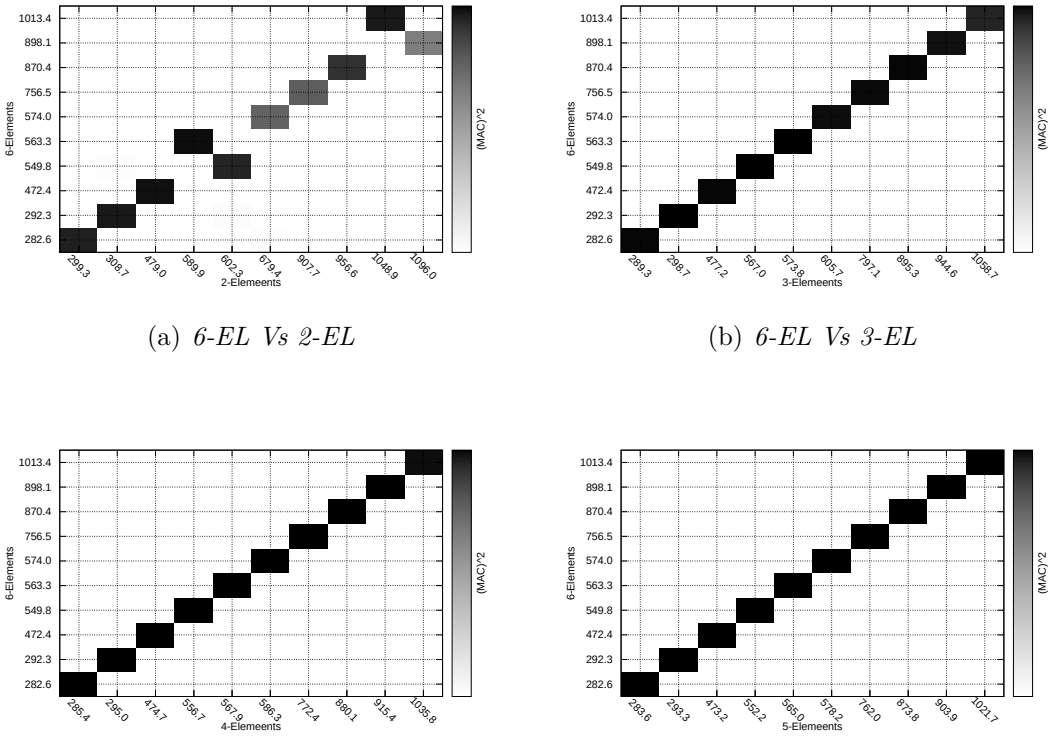

(a) *6-EL Vs 2-EL*

(b) *6-EL Vs 3-EL*

(c) *6-EL Vs 4-EL*

(d) *6-EL Vs 5-EL*

Figure 5.9. MAC considering different number of elements between two stringers.

not provide good convergence. Also, the TE models are not able to detect various modes when lower order theories are used. In contrast, the LE models provide better results. In this case, convergence can be easily achieved by improving the discretization over the cross-section. Only three LE elements are enough to obtain accurate results and also the number of DOFs is just one-half that of the reference model. A higher number of half-waves on the cross-section require a refined mesh with a greater number of LE elements, to be accurately evaluated.

The convergence behavior of the first five modes is shown in Fig.5.13. From the results obtained, the LE models can detect very complex modal shapes, and the results converge to the reference values more than the TE models. On the other hand, TE models are very cheap but do not provide accurate results for reinforced structures.

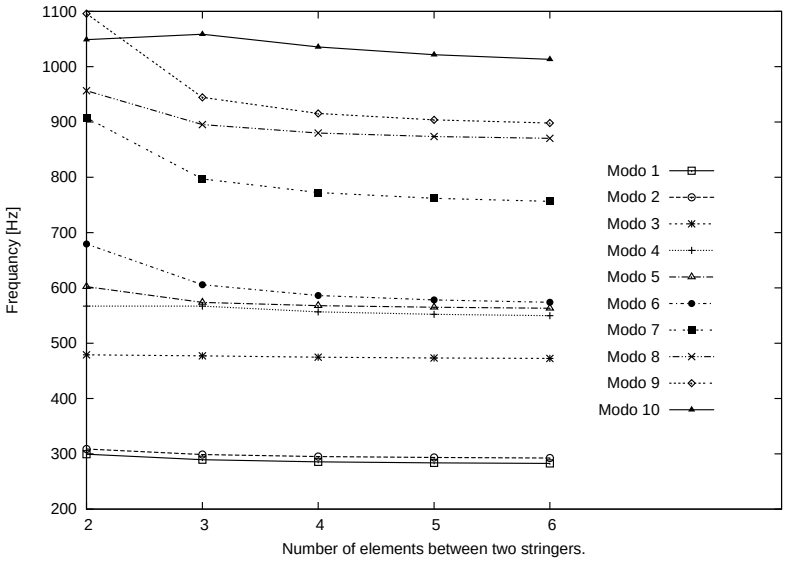

Figure 5.10. Frequencies using various LE elements between two stringers.

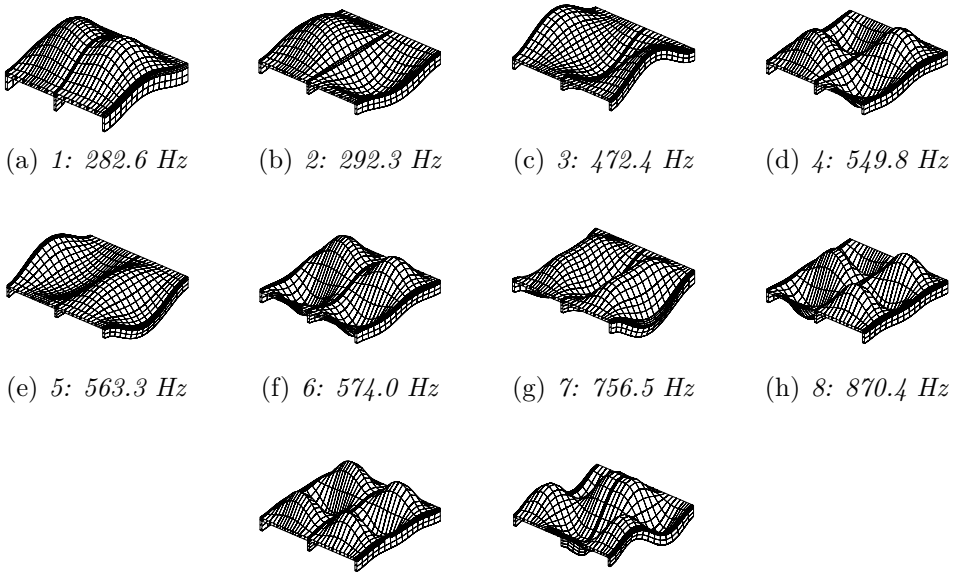

(a) *1: 282.6 Hz* (b) *2: 292.3 Hz* (c) *3: 472.4 Hz* (d) *4: 549.8 Hz*

(e) *5: 563.3 Hz* (f) *6: 574.0 Hz* (g) *7: 756.5 Hz* (h) *8: 870.4 Hz*

(i) *9: 898.1 Hz* (j) *10: 1013.4 Hz*

Figure 5.11. First 10 modes using 6 LE elements between two stringers.

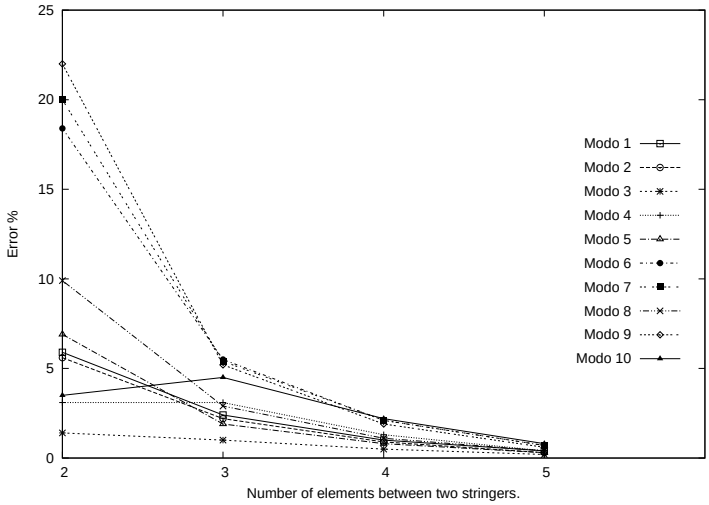

Figure 5.12. Error considering various LE elements between two stringers.

Model	DOF	Mode 1	Mode 2	Mode 3	Mode 4	Mode 5
$FEM3D$	6840	14.1	14.5	23.6	27.2	28.1
LE-2E	3024	$15.0^{(+6.4\%)}$	$15.4^{(+6.2\%)}$	$24.0^{(+1.7\%)}$	$30.1^{(+10.7\%)}$	$29.5^{(+5.0\%)}$
LE-3E	3600	$14.5^{(+2.8\%)}$	$14.9^{(+2.8\%)}$	$23.9^{(+1.3\%)}$	$28.3^{(+4.0\%)}$	$28.7^{(+2.1\%)}$
LE-4E	4176	$14.3^{(+1.4\%)}$	$14.8^{(+2.1\%)}$	$23.7^{(+0.4\%)}$	$27.8^{(+2.2\%)}$	$28.4^{(+1.1\%)}$
LE-5E	4752	$14.2^{(+0.7\%)}$	$14.7^{(+1.4\%)}$	$23.7^{(+0.4\%)}$	$27.6^{(+1.5\%)}$	$28.2^{(+0.4\%)}$
LE-6E	5328	$14.1^{(+0.0\%)}$	$14.6^{(+0.7\%)}$	$23.6^{(+0.0\%)}$	$27.5^{(+1.1\%)}$	$28.2^{(+0.4\%)}$
EULE	48	$21.2^{(+50.4\%)}$	-	-	-	-
TE1	144	$21.0^{(+48.9\%)}$	$161.2^{(+1011.7\%)}$	-	-	-
TE2	288	$18.5^{(+31.2\%)}$	$27.3^{(+88.3\%)}$	$156.0^{(561.0\%)}$	$71.0^{(+161.0\%)}$	-*
TE3	480	$18.2^{(+29.1\%)}$	$23.3^{(+60.7\%)}$	$42.2^{(78.8\%)}$	$50.9^{(+87.1\%)}$	$164.4^{(+485.1\%)}$
TE4	720	$17.8^{(+26.2\%)}$	$22.7^{(+56.6\%)}$	$36.8^{(55.9\%)}$	$54.7^{(+101.1\%)}$	$90.1^{(+220.6\%)}$
TE5	1008	$17.6^{(+24.8\%)}$	$20.8^{(+43.4\%)}$	$31.7^{(34.3\%)}$	$49.0^{(+80.1\%)}$	$45.3^{(+61.2\%)}$
TE6	1344	$16.4^{(+16.3\%)}$	$19.7^{(+35.9\%)}$	$29.3^{(24.2\%)}$	$42.6^{(+56.6\%)}$	$34.4^{(+22.4\%)}$

−: Modes not detected by the model

$(\ )^{(*\%)}$: percentage different to the 3D solution

Table 5.3. First 5 frequencies using TE and LE models.

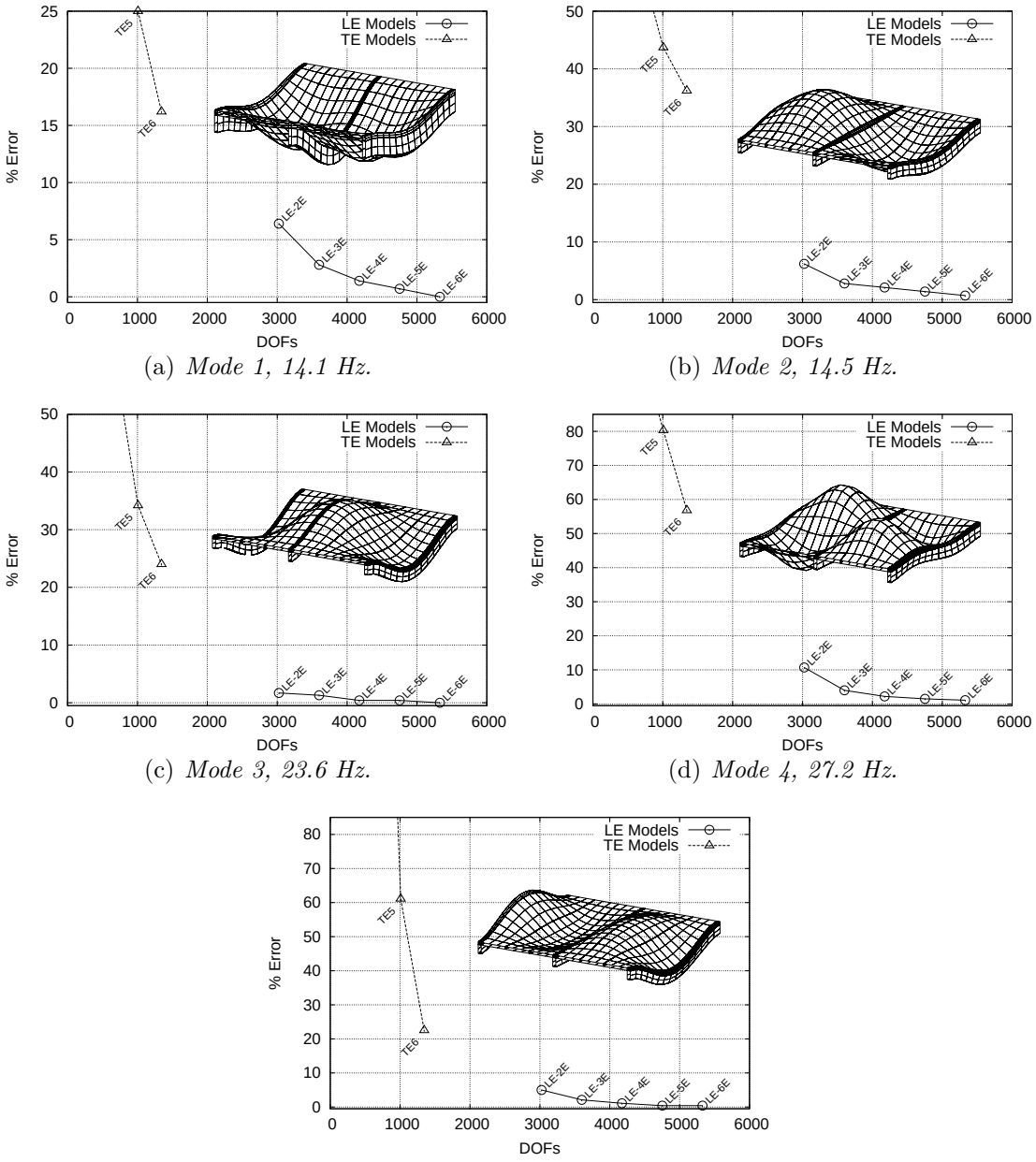

(a) *Mode 1, 14.1 Hz.* (b) *Mode 2, 14.5 Hz.*

(c) *Mode 3, 23.6 Hz.* (d) *Mode 4, 27.2 Hz.*

(e) *Mode 5, 28.1 Hz.*

Figure 5.13. Convergence analysis of the reinforced panel.

Chapter 6

Reinforced structures analysis using classical and refined models

This chapter concerns the static and free vibration analysis of flat and curved panels using various modelling approaches.

6.1 Flat-plate Analysis

Static and free vibration analyses of various flat plates are introduced in this section. Different FE reduced model are considered. The models with *shell* elements for plate and stringer are called $2D$ FE model. When the plate are made using *shell* elements and the stringers are modeled using *beam* element, the $2D-1D$ FE models are obtained. *Solid* or $3D$ FE models are used as the reference solution. The FE models are analyzed using the commercial MSC NASTRAN® code. The structures considered are built in aluminum alloy, with a Young modulus, E, equal to 75 GPa, a Poisson ratio, ν, equal to 0.3 and a density value, ρ, equal to 2700 $\frac{kg}{m^3}$.

6.1.1 Static analysis

The static analysis of a stiffened plate is performed in this section. The case considered is the static analysis of a stiffened plate loaded by a static load. A "very low" aspect-ratio is used because this is the worst condition for classical beam models. Different orders of expansion, N, are considered in the TE models, while, different meshes are used over the cross-section when the LE models are adopted. Four- and nine points LE elements are utilized. Only cubical beam elements (B4) are used in the axial discretization for the FEM approximation. The beam nodes are uniformly distributed along the longitudinal axis ($y-axis$).

The geometry of the structure is shown in Fig. 6.1. Sides a and b are both equal

to 2 [m], and the plate thickness is 0.02 [m]. The geometry of the cross-section, the *x-z plane*, is shown in Fig. 6.3*a* and the geometrical dimensions are reported in Tab.6.3. The structure is subjected to a concentrated load, P, which is applied at point (C) with magnitude of 20000 N (see Fig. 6.2).

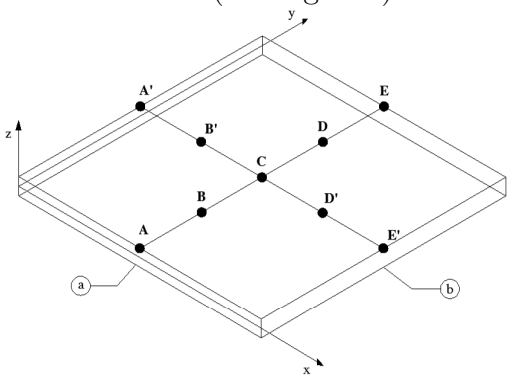

Figure 6.1. Three-dimensional plate model.

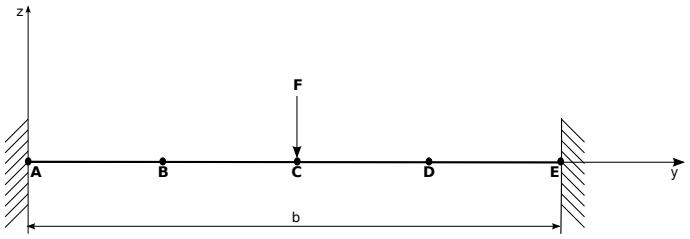

Figure 6.2. Geometrical and boundary conditions in the beam configuration.

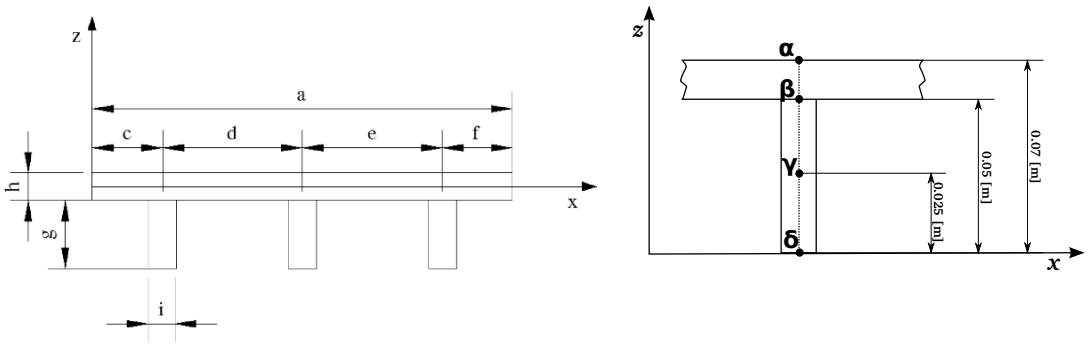

(a) *Cross-section geometry.*

(b) *Stringer geometry and reference points.*

Figure 6.3. Cross-section geometrical properties.

The vertical displacements are evaluated at four points on the top of the plate (C,B,A′,B′, see Fig. 6.1), while the stress analysis are computed at four points through the thickness of the central stringers (α, β, γ, δ, see Fig. 6.3*b*). The 1D refined model based on the CUF is called 1D CUF model. Three FE models are added in the analyses. A principal solid FE model, FEM_{3D-REF} (see Fig.6.7), used to compare all the results. A second solid FE model, FEM_{3D} (see Fig. 6.8), with some degrees of freedoms nearest to the present beam model.

For the 1D CUF model different expansion functions are used. Concerning Taylor expansions, two TE models are used, in particular, an eighth, $TE8$, and a tenth, $TE10$, order model. Concerning Lagrange expantion functions, four LE models are considered, $P-1$, $P-2$, $P-3$ and $P-4$. The cross-sections of the LE models are shown in Figures 6.4a, 6.5a and 6.6a, while the node distributions are presented in Figures 6.4b, 6.5b and 6.6b, respectively. Models $P-4$ and $P-2$ have the same cross-section, but the first has 8-B4 elements on the $y-axis$, as can be seen in Table 6.1. FEM_{3D} and the $P-2$ models have the same number of DOFs.

$Model$	N_{El}	$N_{Nodes-El}$	N_{B4}
Reinforced Plate			
$P-1$	14	4	8
$P-2$	36	9	8
$P-3$	36	9	8
$P-4$	36	9	12

Table 6.1. Properties of the LE models.

Point	$x[m]$	$y[m]$	$z[m]$
A	$a/2$	0	$h/2$
B	$a/2$	$b/4$	$h/2$
C	$a/2$	$b/2$	$h/2$
D	$a/2$	$\frac{3}{4}b$	$h/2$
E	$a/2$	b	$h/2$
A’	0	$b/2$	$h/2$
B’	$a/4$	$b/2$	$h/2$
D’	$\frac{3}{4}a$	$b/2$	$h/2$
E’	a	$b/2$	$h/2$

Table 6.2. Position of the reference points for the stiffened plate.

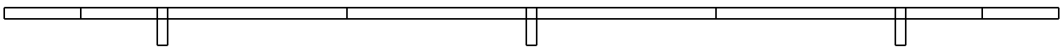

(a) *Cross-Section Mesh.*

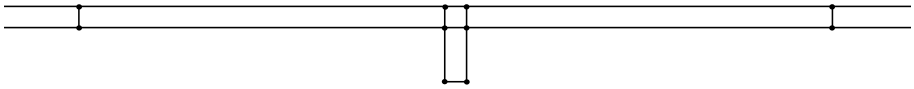

(b) *Nodes positioning.*

Figure 6.4. Model P-1 for the stiffened plate.

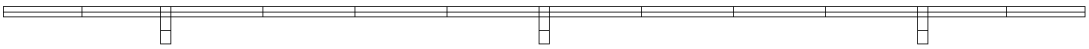

(a) *Cross-Section Mesh.*

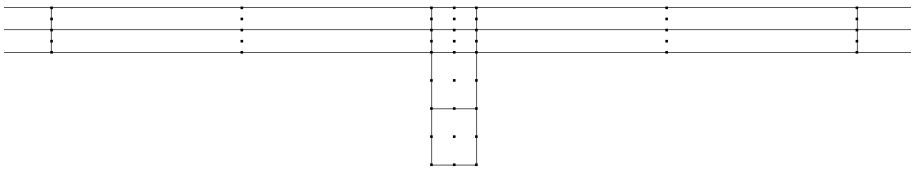

(b) *Nodes positioning.*

Figure 6.5. Model P-2 for the stiffened plate.

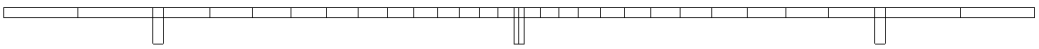

(a) *Cross-Section Mesh.*

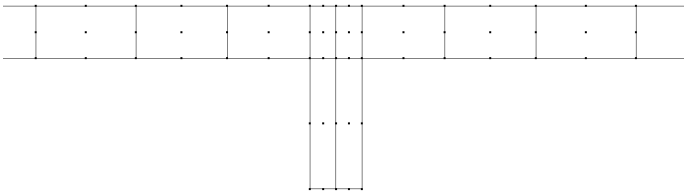

(b) *Nodes positioning.*

Figure 6.6. Model P-3 for the stiffened plate.

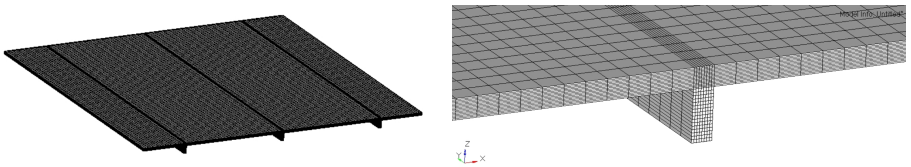

(a) *Global structure.* (b) *Local view.*

Figure 6.7. Solid FE Refined Model with 724299 DOFs.

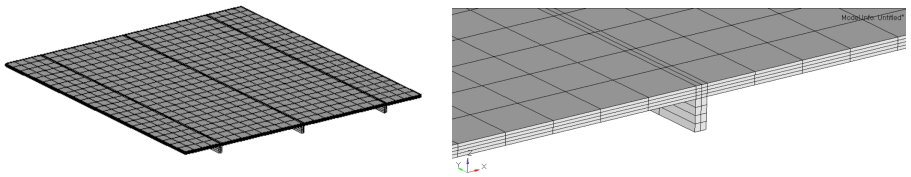

(a) *Global structure.* (b) *Local view.*

Figure 6.8. Solid FE Model with 14325 DOFs.

a	c	d	e	f	g	h	i
2.00	0.30	0.70	0.70	0.30	0.05	0.02	0.02

Table 6.3. Cross-section geometry [m] for the stiffened plate.

Displacement analysis

The vertical displacement in the $x-z$ and $z-y$ planes are shown in Figures 6.9a and b, respectively. Tab.6.4 shows the displacements evaluated using the different models. The first column contains the models used, and the results of each model are given regarding vertical displacements in the points shown in Fig.6.1.

Model	DOF	$Point-C$	$Point-B$	$Point-A'$	$Point-B'$
FEM_{3D-R}	724299	-4.216	-2.047	+0.239	-2.055
FEM_{3D}	14325	-3.81$^{(-10.4\%)}$	-2.25$^{(+10.3\%)}$	+0.24$^{(+1.7\%)}$	-1.76$^{(-14.0\%)}$
TE 8	3375	-3.27$^{(-23.2\%)}$	-1.55$^{(-23.9\%)}$	-0.59$^{(-346.9\%)}$	-1.96$^{(-4.3\%)}$
TE 10	4950	-3.66$^{(-14.0\%)}$	-1.75$^{(-14.4\%)}$	+0.13$^{(-42.3\%)}$	-2.02$^{(-1.4\%)}$
$P-1$	2325	-2.19$^{(-48.6\%)}$	-0.99$^{(-51.6\%)}$	-1.49$^{(-727.2\%)}$	-1.52$^{(-25.6\%)}$
$P-2$	14325	-4.18$^{(-1.8\%)}$	-2.00$^{(-2.1\%)}$	+0.24$^{(+3.3\%)}$	-2.02$^{(-1.6\%)}$
$P-3$	16275	-4.21$^{(-1.1\%)}$	-2.01$^{(-1.6\%)}$	+0.23$^{(-0.4\%)}$	-2.01$^{(-1.8\%)}$
$P-4$	21201	-4.20$^{(-1.4\%)}$	-2.01$^{(-1.4\%)}$	+0.24$^{(+2.1\%)}$	-2.03$^{(-1.0\%)}$

$(\ )^{(*\%)}$: $*$ *percentage different with respect to* FEM_{3D-REF} *Model.*

Table 6.4. Vertical displacement $\times\ 10^{-3}$ [m] for the stiffened plate.

The refined solid FE model (FEM_{3D-REF}) is shown in the first row, while the second row contains the second solid FE model (FEM_{3D}). Tab.6.4 contains also the TE and LE results. When the order N increases, TE results are characterized by a slow convergence on the FEM_{3D-REF}, as shown in Fig. 6.9. As a consequence, the TE results are neglected in the subsequent analyses. The results of the $P-1$ model show the limitations of the four-points elements; its kinematic requires a refined mesh, and the correction of the Poisson locking and higher order elements are therefore preferred. As Shown in Tab.6.4, Models $P-2$, $P-3$ and $P-4$ provide an accurate solution with an error of about 2%, using some DOFs that is less than 3% of those used by the reference model.

Stress analysis

The stress analysis is computed with the present models comparing the results with those of the solid FEM_{3D-REF} model. σ_{yy} and τ_{yz} are considered. σ_{yy} is evaluated through the thickness of the central stringer for $x=\dfrac{a}{2}$ and $y=\dfrac{b}{2}$, while τ_{yz} is

measured for $x = \frac{a}{2}$, $y = \frac{3}{4}b$. Fig. 6.10*a* shows the σ_{yy} distribution through the thickness, from the top of the plate to the bottom of the stringer.

Model	DOF	$Point-\alpha$	$Point-\beta$	$Point-\gamma$	$Point-\delta$
		$x = a/2$, $y = b/2$			
FEM_{3D-REF}	724299	-53.1	+13.0	+74.2	+118.1
FEM_{3D}	14325	-24.0 $^{(-54.7\%)}$	+10.8 $^{(-17.2\%)}$	+39.8 $^{(-46.3\%)}$	+70.5 $^{(-40.3\%)}$
$P-2$	14325	-50.7 $^{(-4.5\%)}$	+12.2 $^{(-6.2\%)}$	+72.8 $^{(-1.8\%)}$	+121.1 $^{(+2.5\%)}$
$P-3$	16275	-56.4 $^{(+6.3\%)}$	+14.1 $^{(+8.6\%)}$	+71.1 $^{(-4.1\%)}$	+121.0 $^{(+2.5\%)}$
$P-4$	21201	-52.8 $^{(-0.5\%)}$	+12.6 $^{(-2.8\%)}$	+72.7 $^{(-2.1\%)}$	+120.1 $^{(+1.7\%)}$

$(\ )^{(*\%)}$: $*$ *percentage different with respect to* FEM_{3D-REF} *Model.*

Table 6.5. σ_{yy} [MPa] at the selected points for the stiffened plate.

Model	DOF	$Point-\gamma$
	$x = a/2$, $y = (3/4)b$	
FEM_{3D-REF}	724299	-2.95
FEM_{3D}	14325	-5.12 $^{(+73.6\%)}$
$P-2$	14325	-2.54 $^{(-13.9\%)}$
$P-3$	16275	-3.03 $^{(+2.7\%)}$
$P-4$	21201	-2.98 $^{(+1.0\%)}$

$(\ )^{(*\%)}$: $*$ *percentage different with respect to* FEM_{3D-REF} *Model.*

Table 6.6. τ_{yz} [MPa] at the central stringer for the stiffened plate.

Fig.6.10*b* shows the τ_{yz} distribution through the thickness of the stringer. Tab.6.5 shows the value of the axial stress. Despite the FEM_{3D} and $P-2$ models have the same DOFs, the $P-2$ solution is more accurate. All the LE models provide a better solution, even though the LE DOFs are about 3% of the FEM_{3D-REF} DOFs. Tab.6.10*b* shows the τ_{yz} value in the center of the central stringer. In this case, the $P-2$ error is about 14% than the FEM_{3D-REF} solution, but the FEM_{3D} model is much less accurate. Both the $P-3$ and $P-4$ models give very accurate solutions, and very close to the value provided by the FEM_{3D-REF} model. These results show that the computation of the shear stress requires a more accurate model than the evaluation of the axial stress. The refined beam models based on the CUF presented in this work can correctly predict the stress distributions but with a remarkable reduction in computational costs.

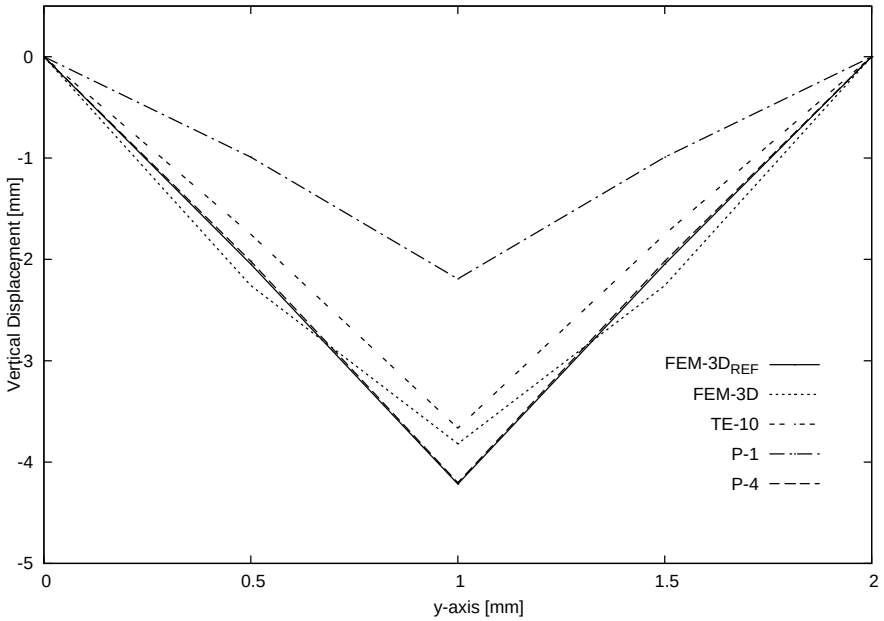

(a) *Axial Displacement at* $x = a/2$.

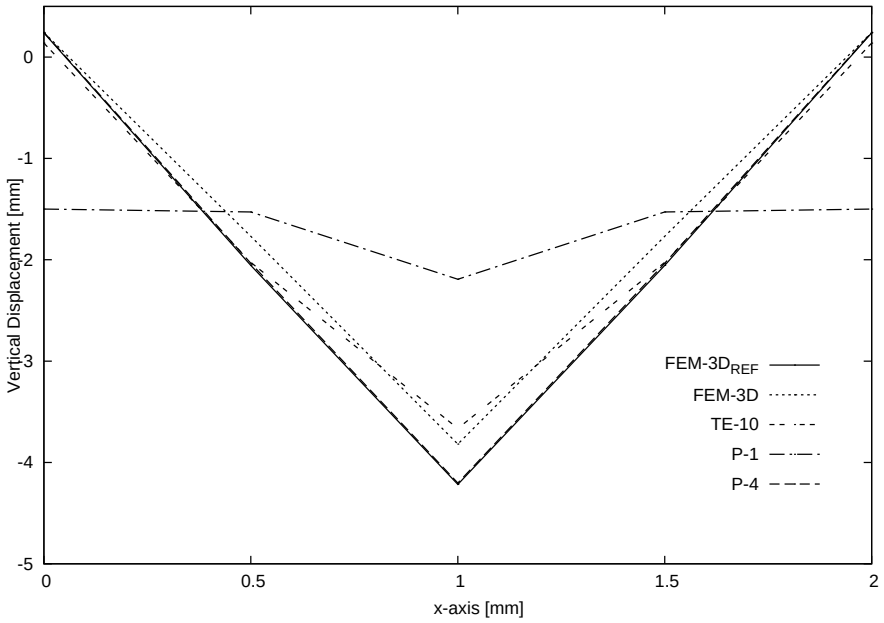

(b) *Cross-section displacement at* $y = b/2$.

Figure 6.9. Vertical displacements for the flat plate.

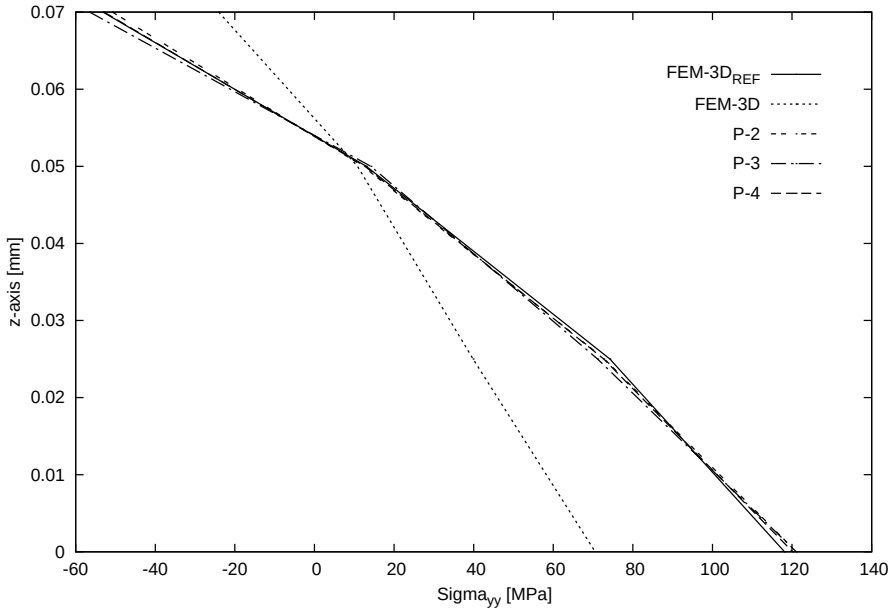

(a) σ_{yy} *in* $x = a/2$ *and* $y = b/2$.

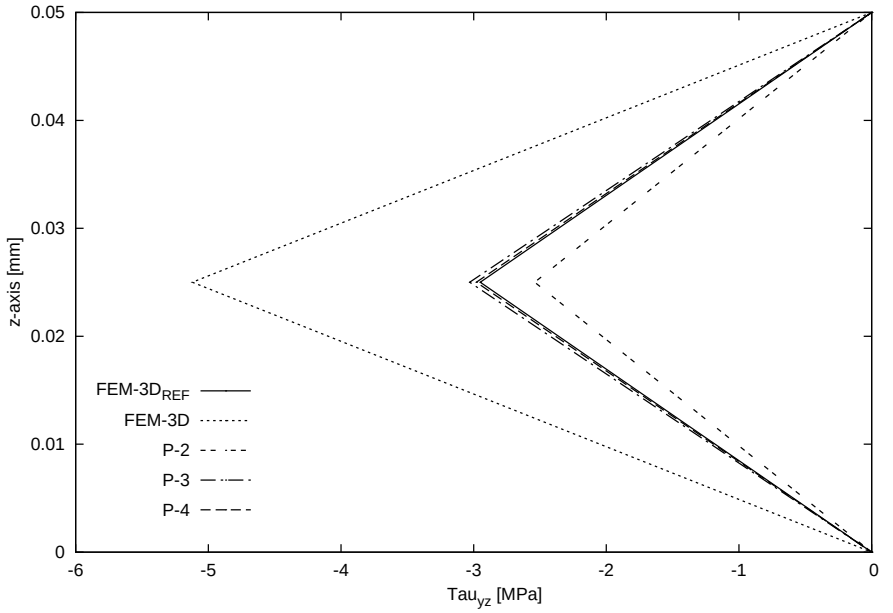

(b) τ_{yz} *along the central stringer, in* $x = a/2$ *and* $y = (3/4)b$.

Figure 6.10. Stress distribution for the flat plate.

6.1.2 Free vibration analysis

The free vibration analysis conducted in this section. The *Solid FE* model (Fig.6.13a) is used to compare the results. There are two FE models in the adopted commercial code. The $2D$ model (Fig.6.13c) made using shell elements for both plate and stringer. The $2D-1D$ model (Fig.6.13d) created using shell elements for the plate and beam elements for the stringers. Stringer elements considered in the former two models, with the correct offset. The $1D-CUF$ model called LE model is shown in Fig.6.11. These models are assessed and compared considering different aspect ratios and cross-sections (L and Z shapes) for the stringer.

6.1.3 The effect of the aspect-ratio of the stringer

The effect of the aspect-ratio of the stringer has been investigated in this part. The shape of the plate was the same for all the considered cases, but five different aspect-ratios were considered (see Fig.6.11). In particular, calling the horizontal side a and the vertical side of the cross-section of the stringer b, the considered b/a was 0.5, 1, 2, 4 and 8. Five $L9$ elements were used on the left and on the right of the stringer (see Fig.6.11) and $6-B4$ elements were introduced along the $y-axis$. The boundary conditions and further details are shown in Fig.6.12.

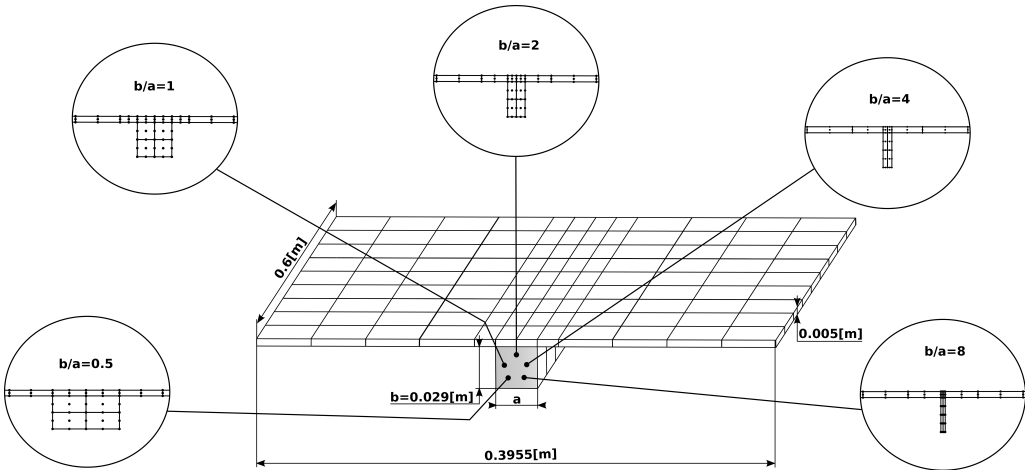

Figure 6.11. Different cross-section used for the stringer in the reinforced plate.

The *Shell* and *Shell* $-$ *Beam* FE models, shown in Fig.6.13, have the same number of elements along the $y-axis$ compared to the *Solid* FE model. Figures 6.14, 6.15, 6.16, 6.17 and 6.18 show the MAC between different models, in particular the matching shown are between the *Solid* FE model and the LE model, the *Solid* FE model and the *Shell* FE model, and the *Solid* and the *Shell* $-$ *Beam* FE models for all the considered aspect-ratios.

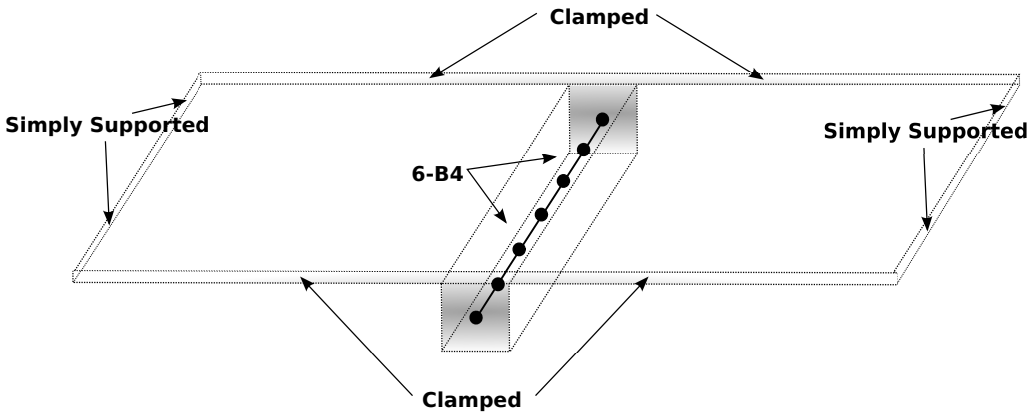

Figure 6.12. Boundary conditions applied on the reinforced plate.

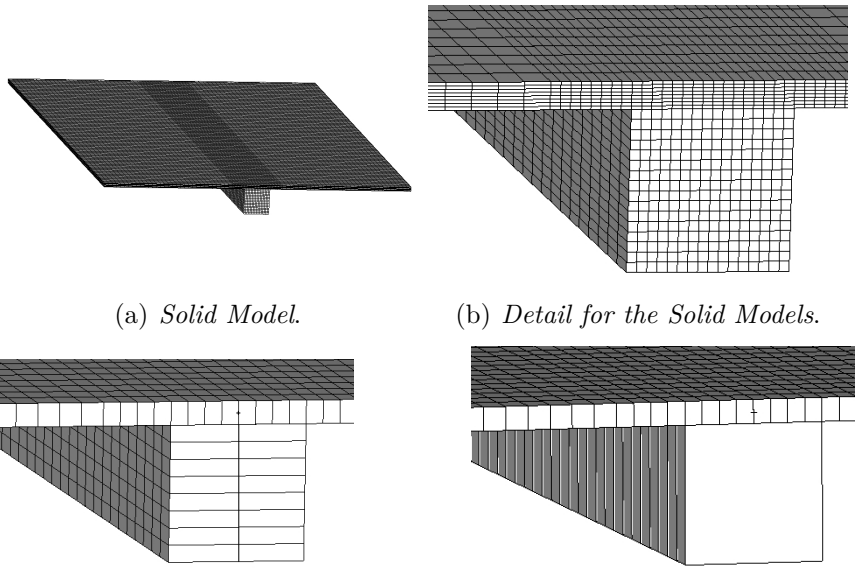

(a) *Solid Model.* (b) *Detail for the Solid Models.*

(c) *Detail for the Shell model.* (d) *Detail for the Shell-Beam model.*

Figure 6.13. Different models with b/a = 1 for the stiffened plate.

Tab.6.7 shows the results obtained considering the five aspect ratios for the first 5 modes (see Fig.6.19). The LE error in mode 1 is almost constant for all the considered aspect ratios, and it is about 1%, as shown in Fig.6.20b. The error for $b/a = 0.5$, in both the $2D$ and $2D-1D$ FE models, is about 10%. Only when the aspect ratio used is biggest than 4 the error is below 1%. However, the LE DOFs are only 2% than the $3D$ DOFs. The previously behavior characterizes the other modes, as shown in Tab.6.7, where the maximum error committed by the $2D$ and $2D-1D$ FE models is about 20%, unlike the LE model, where the error decreased

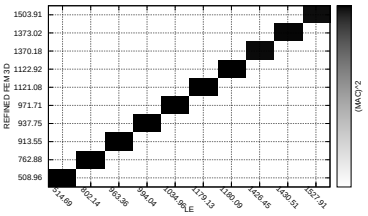

(a) *Ref 3D FE Vs LE FE.*

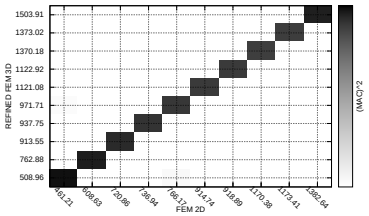

(b) *Ref 3D FE Vs 2D FE.*

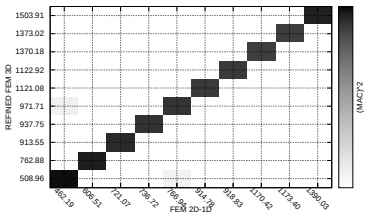

(c) *Ref 3D FE Vs 2D-1D FE.*

Figure 6.14. MAC for the stiffened plate using different FE models and b/a=0.5.

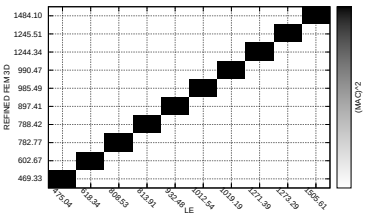

(a) *Ref 3D FE Vs LE FE.*

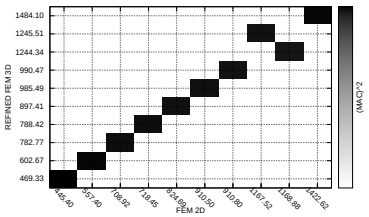

(b) *Ref 3D FE Vs 2D FE.*

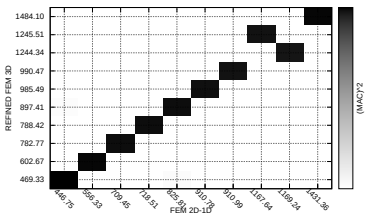

(c) *Ref 3D FE Vs 2D-1D FE.*

Figure 6.15. MAC for the stiffened plate using different FE models and b/a=1.

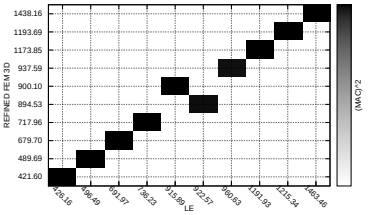

(a) *Ref 3D FE Vs LE FE.*

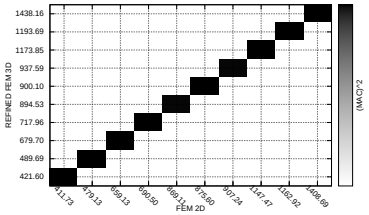

(b) *Ref 3D FE Vs 2D FE.*

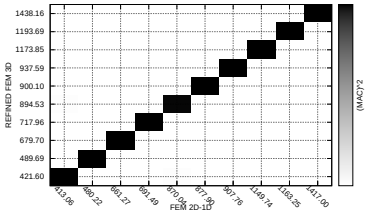

(c) *Ref 3D FE Vs 2D-1D FE.*

Figure 6.16. MAC for the stiffened plate using different FE models and b/a=2.

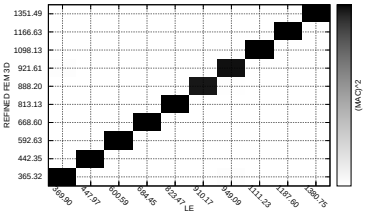

(a) *Ref 3D FE Vs LE FE.*

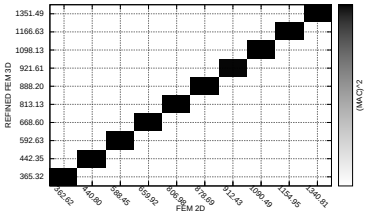

(b) *Ref 3D FE Vs 2D FE.*

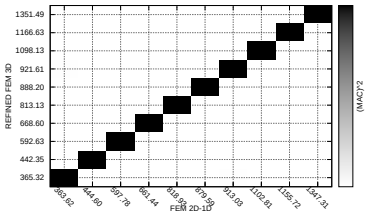

(c) *Ref 3D FE Vs 2D-1D FE.*

Figure 6.17. MAC for the stiffened plate using different FE models and b/a=4.

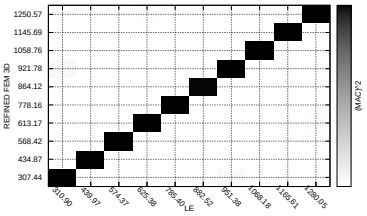

(a) *Ref 3D FE Vs LE FE.*

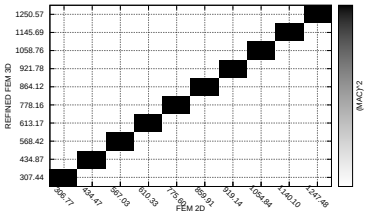

(b) *Ref 3D FE Vs 2D FE.*

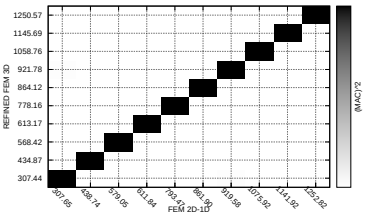

(c) *Ref 3D FE Vs 2D-1D FE.*

Figure 6.18. MAC for the stiffened plate using different FE models and b/a=8.

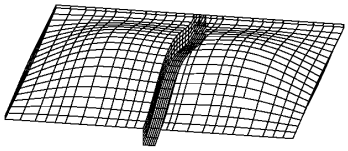

(a) *1: 426.16[Hz].*

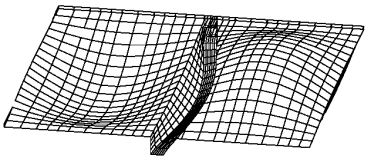

(b) *2: 496.49[Hz].*

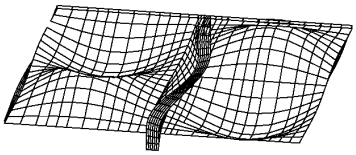

(c) *3: 691.97[Hz].*

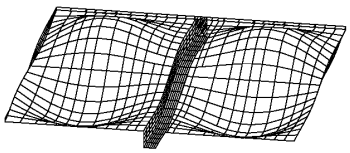

(d) *4: 736.23[Hz].*

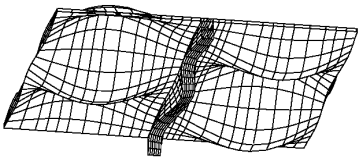

(e) *5: 922.57[Hz].*

Figure 6.19. First 5 modes with b/a=2 for the stiffened plate.

to 6%.

Fig.6.20, 6.21, 6.22, 6.23 and 6.24 show as increasing the value of b/a as the stiffness of the plate is decreased and the modes appear at a lower frequency. When b/a is equal to 0.5 and 1, the $2D$ and $1D-2D$ FE models not provide a good solution and the error for mode 1 and 8% for mode 2 (see Fig.6.24a).

The results highlight how the CUF models are not dependent on the value of the aspect ratio used, while the solution of the reduced FE models depends on the aspect ratio of the stringer.

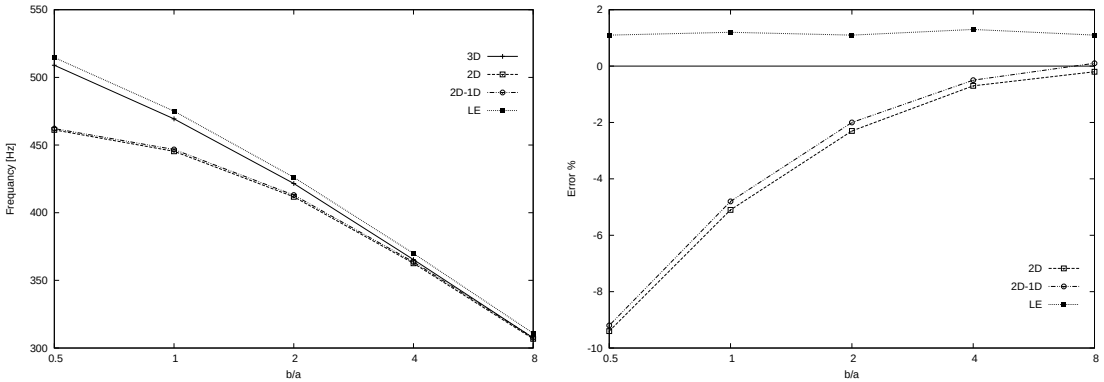

(a) *behavior of the mode.* (b) *Percentage Error.*

Figure 6.20. Mode 1 of the stiffened plate.

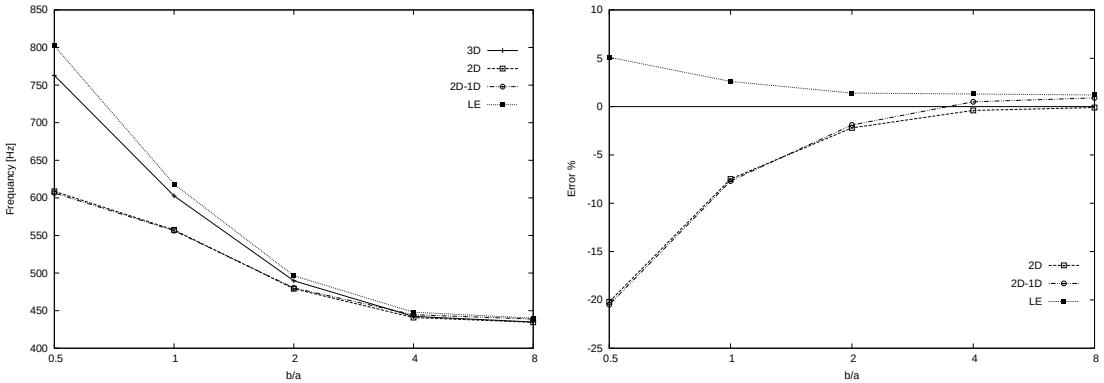

(a) *behavior of the mode.* (b) *Percentage Error.*

Figure 6.21. Mode 2 of the stiffened plate.

The effect of the cross-section with L-shape

In this section, two classical shapes of the stringer are considered, L and Z shapes. Fig.6.25 shows the geometrical properties of the plate. The same figure shows the

Model	FEM_{3D}	FEM_{2D}	FEM_{2D-1D}	LE
DOF / b/a	243459	37926	34080	4731
		Mode 1		
0.5	508.96	$461.21^{(-9.4\%)}$	$462.19^{(-9.2\%)}$	$514.69^{(+1.1\%)}$
1	469.33	$445.40^{(-5.1\%)}$	$446.75^{(-4.8\%)}$	$475.04^{(+1.2\%)}$
2	421.60	$411.73^{(-2.3\%)}$	$413.06^{(-2.0\%)}$	$426.16^{(+1.1\%)}$
4	365.32	$362.62^{(-0.7\%)}$	$363.62^{(-0.5\%)}$	$369.90^{(+1.3\%)}$
8	307.44	$306.77^{(-0.2\%)}$	$307.65^{(+0.1\%)}$	$310.90^{(+1.1\%)}$
		Mode 2		
0.5	762.88	$608.63^{(-20.2\%)}$	$606.51^{(-20.5\%)}$	$802.14^{(+5.1\%)}$
1	602.67	$557.40^{(-7.5\%)}$	$556.33^{(-7.7\%)}$	$618.34^{(+2.6\%)}$
2	489.69	$479.13^{(-2.2\%)}$	$480.22^{(-1.9\%)}$	$496.49^{(+1.4\%)}$
4	442.35	$440.80^{(-0.4\%)}$	$444.60^{(+0.5\%)}$	$447.97^{(+1.3\%)}$
8	434.87	$434.47^{(-0.1\%)}$	$438.74^{(+0.9\%)}$	$439.97^{(+1.2\%)}$
		Mode 3		
0.5	913.55	$720.86^{(-21.1\%)}$	$721.07^{(-21.1\%)}$	$963.36^{(+5.5\%)}$
1	782.77	$708.92^{(-9.4\%)}$	$709.45^{(-9.4\%)}$	$808.53^{(+3.3\%)}$
2	679.70	$659.13^{(-3.0\%)}$	$661.22^{(-2.7\%)}$	$691.97^{(+1.8\%)}$
4	592.63	$588.45^{(-0.7\%)}$	$592.63^{(+0.0\%)}$	$600.59^{(+1.3\%)}$
8	568.42	$567.03^{(-0.2\%)}$	$579.05^{(+1.9\%)}$	$574.37^{(+1.0\%)}$
		Mode 4		
0.5	937.75	$736.94^{(-21.4\%)}$	$736.72^{(-21.4\%)}$	$994.04^{(+6.0\%)}$
1	788.42	$718.45^{(-8.9\%)}$	$718.51^{(-8.9\%)}$	$813.91^{(+3.2\%)}$
2	717.96	$690.50^{(-3.8\%)}$	$691.49^{(-3.7\%)}$	$736.23^{(+2.5\%)}$
4	668.60	$659.92^{(-1.3\%)}$	$661.44^{(-1.1\%)}$	$684.45^{(+2.4\%)}$
8	613.17	$610.33^{(-0.5\%)}$	$611.84^{(-0.2\%)}$	$625.38^{(+2.0\%)}$
		Mode 5		
0.5	971.71	$766.17^{(-21.2\%)}$	$766.94^{(-21.1\%)}$	$1034.96^{(+6.5\%)}$
1	897.41	$824.69^{(-8.1\%)}$	$825.81^{(-8.0\%)}$	$932.48^{(+3.9\%)}$
2	894.53	$869.11^{(-2.8\%)}$	$870.04^{(-2.7\%)}$	$922.57^{(+3.1\%)}$
4	813.13	$806.98^{(-0.8\%)}$	$818.93^{(+0.7\%)}$	$823.47^{(+1.3\%)}$
8	778.16	$775.60^{(-0.3\%)}$	$793.47^{(+2.0\%)}$	$785.40^{(+0.9\%)}$

$(\ )^{(*\%)} : * \ percentage\ different\ with\ respect\ to\ Ref\ FEM-3D.$

Table 6.7. The first 5 frequencies using different models for the reinforced plate.

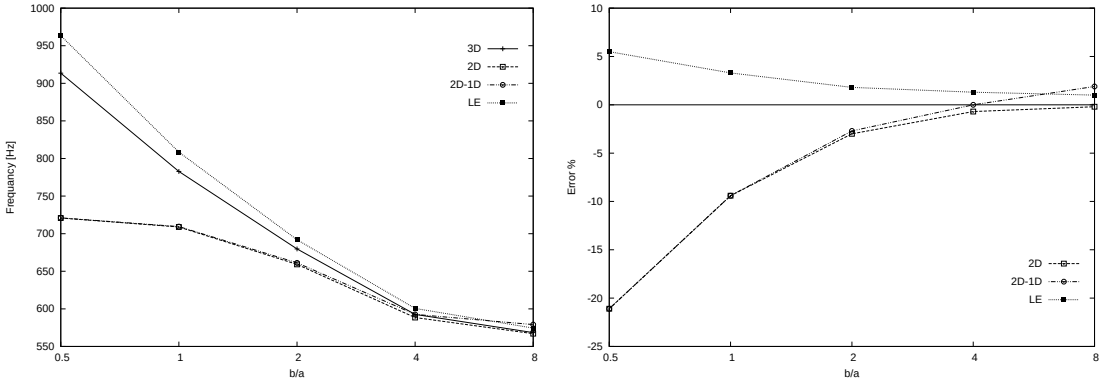

(a) *behavior of the mode.* (b) *Percentage Error.*

Figure 6.22. Mode 3 of the stiffened plate.

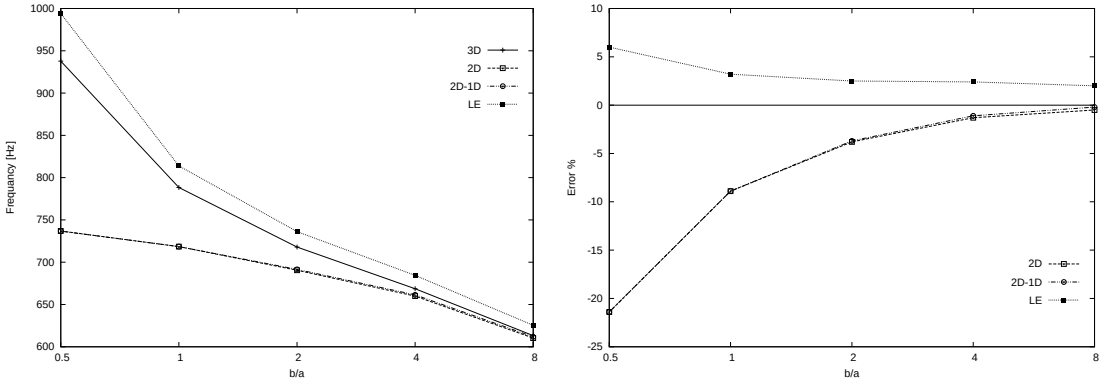

(a) *behavior of the mode.* (b) *Percentage Error.*

Figure 6.23. Mode 4 of the stiffened plate.

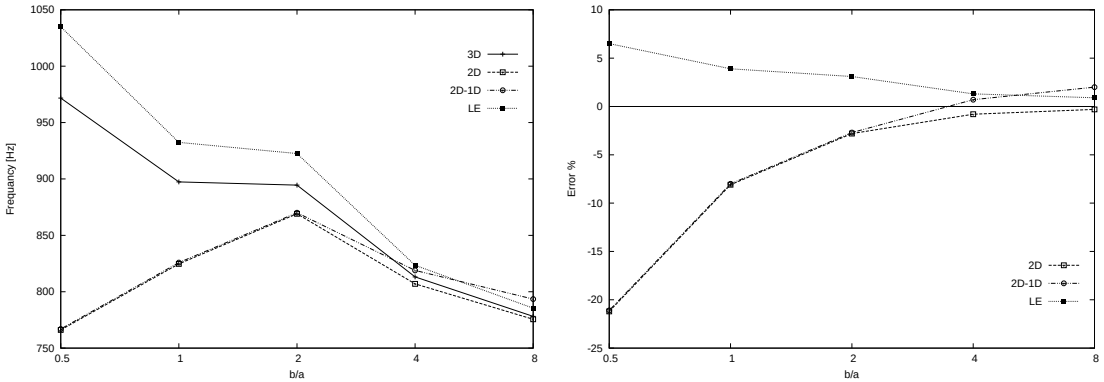

(a) *behavior of the mode.* (b) *Percentage Error.*

Figure 6.24. Mode 5 of the stiffened plate.

number of $L9$ elements used on the cross-section, where each square on the cross-section stands for an $L9$ element. The boundary conditions are shown in Fig.6.12.

Tab.6.8 shows the first 12 frequencies used to compare the results with the *Solid* model shown in Figures 6.27a and b. The *Shell* and $Shell-Beam$ reduced FE models are shown in Figures 6.27c and d, respectively. Fig.6.26j,k and l show the local stringer deformation, in fact, the plate is undeformed, as highlighted in Fig.6.28a. However, Fig.6.26 shows some very important shell-like modes, such as mode 4 and mode 8, where the deformation of the plate is the typical deformation of shell models. Using the MAC, mode 11 of the LE model appeared twice in the $3D$ FE model because it is a symmetric mode. MAC highlights the difficulties of the $Shell-beam$ model to find the local modes of the stringer. Fig.6.29a shows that the line related to the $Shell-Beam$ model is discontinued when there are local modes of the stringer, and its error increases for both modes 8 and 9, as shown in Fig.6.29b. In fact, in the $Shell-Beam$ model the effect of the stringer is added to the plate via inertia momentum and its shape becomes an irrelevant parameter although the beam offset is included. The LE model provides a good solution. In fact, the LE error for the first five modes is very low, and its trend is almost constant for the first seven frequencies, as shown in Fig.6.29b. The LE error for modes 8, 9 and 10 is about 9%, with respect the $3D$ FE model, but the LE DOFs are only 2% than the $3D$ DOFs, while the $2D$ DOFs are about 20% than the *Solid* DOFs.

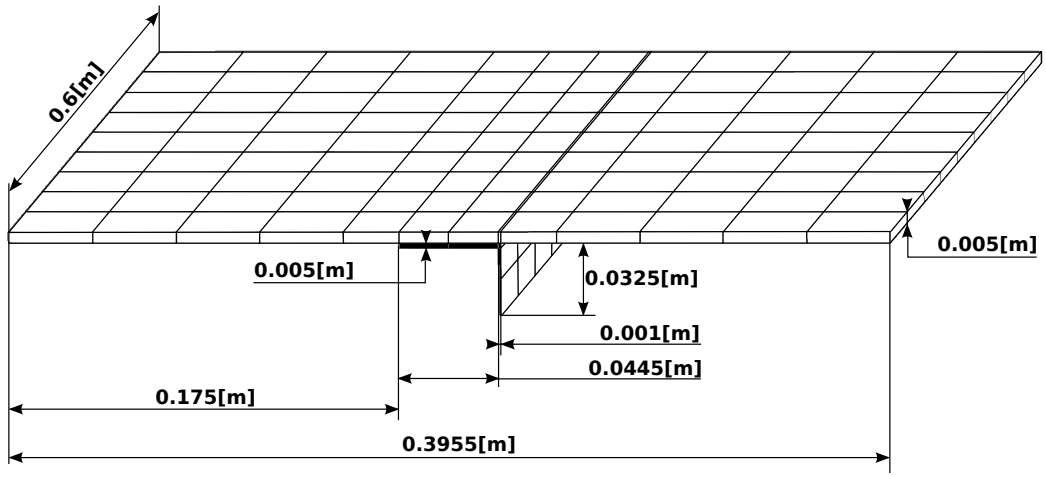

Figure 6.25. Reinforced plate with the stringer with the L-shape.

The effect of the cross-section with Z-shape

Fig.6.30 shows the geometry of the plate on which the stringer has a Z-shape. Again, in this case, the main model is the *Solid* FE model shown in Fig.6.32a and b. Figures

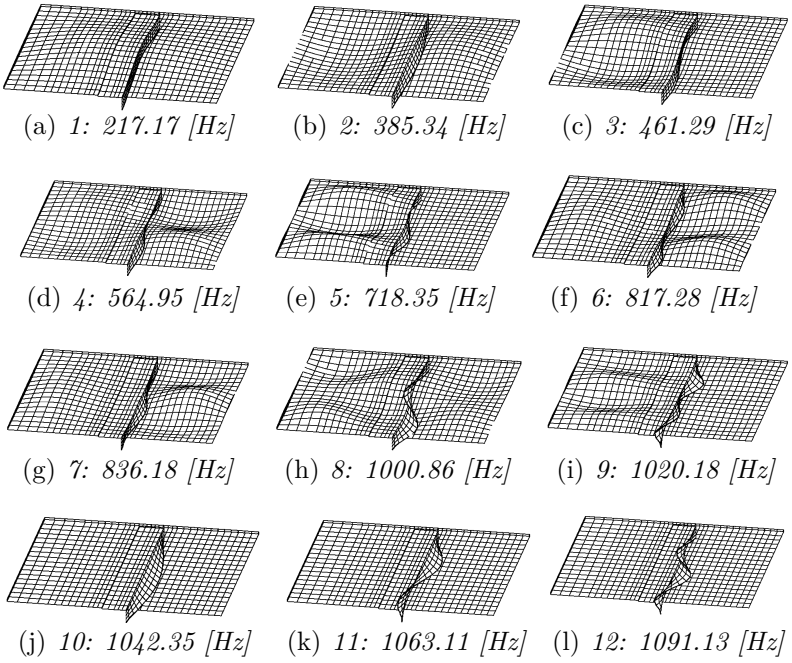

(a) *1: 217.17 [Hz]* (b) *2: 385.34 [Hz]* (c) *3: 461.29 [Hz]*

(d) *4: 564.95 [Hz]* (e) *5: 718.35 [Hz]* (f) *6: 817.28 [Hz]*

(g) *7: 836.18 [Hz]* (h) *8: 1000.86 [Hz]* (i) *9: 1020.18 [Hz]*

(j) *10: 1042.35 [Hz]* (k) *11: 1063.11 [Hz]* (l) *12: 1091.13 [Hz]*

Figure 6.26. The first 12 modes for the plate with the stringer with the L-shape.

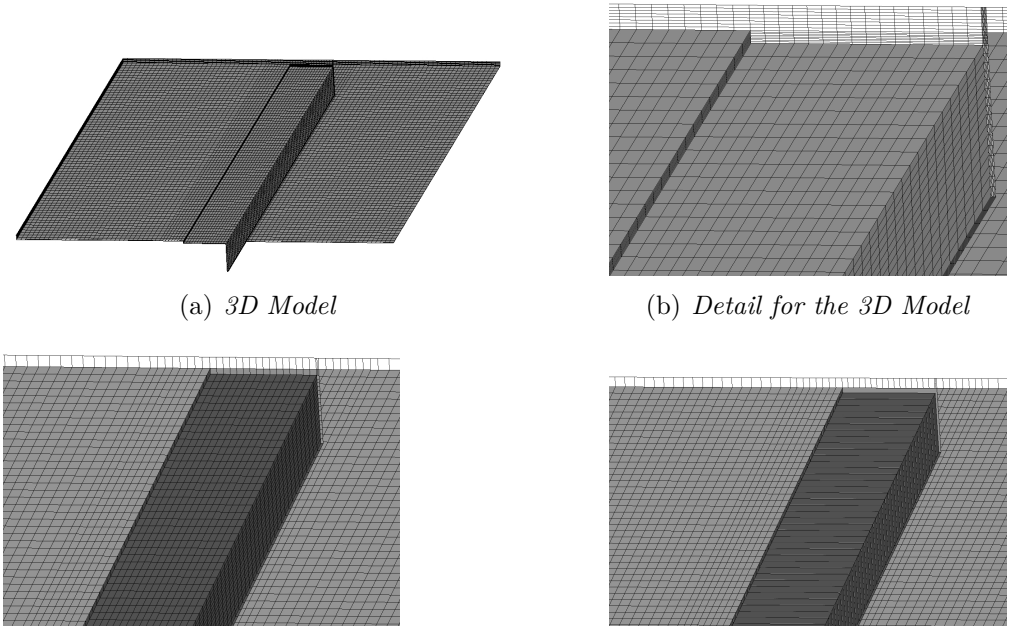

(a) *3D Model* (b) *Detail for the 3D Model*

(c) *Detail for the 2D Model* (d) *Detail for the 2D-1D Model*

Figure 6.27. Various models for the plate with the stringer with the L-shape.

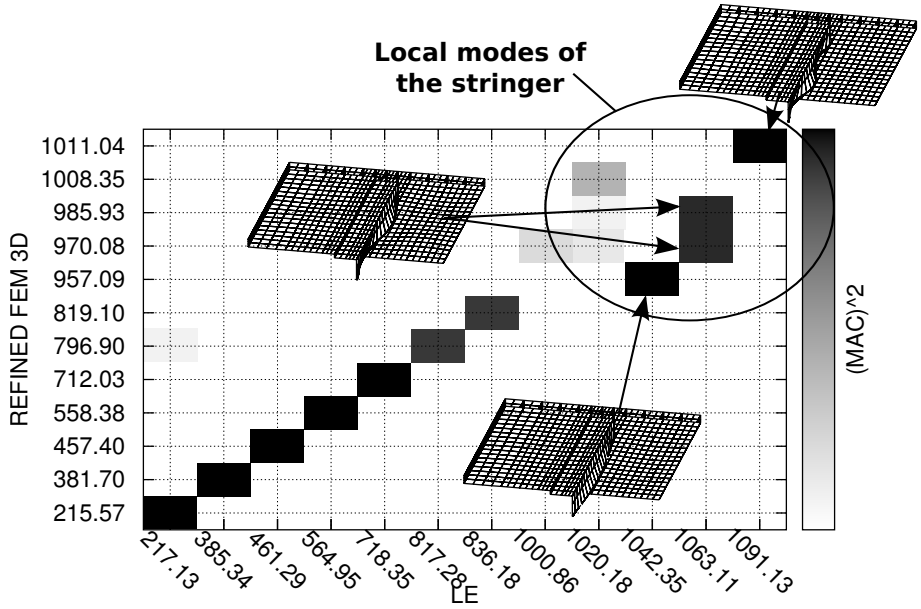

(a) *Refined FE Solid Model Vs LE Model.*

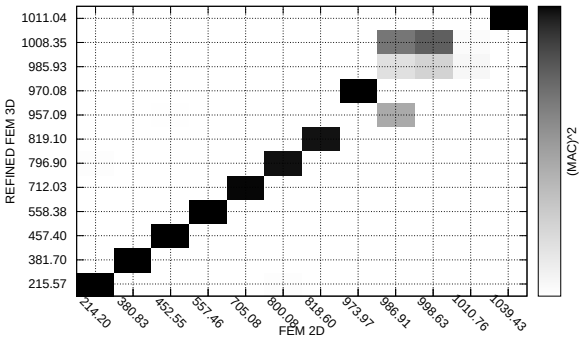

(b) *Ref 3D FE Model Vs 2D FE Model.*

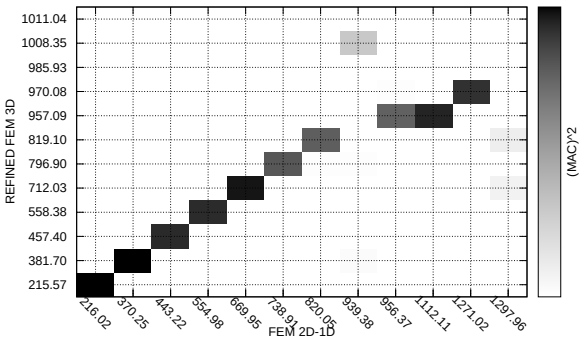

(c) *Ref 3D FE Model Vs 2D-1D FE Model.*

Figure 6.28. MAC using the stringer with the stringer with the L-shape.

Freq[Hz]	FEM_{3D-REF}	FEM_{2D}	FEM_{2D-1D}	LE
DOF	274131	57120	41748	6099
1	215.57	214.20 $^{(-0.6\%)}$	216.02$^{(+0.2\%)}$	217.13 $^{(+0.7\%)}$
2	381.70	380.83 $^{(-0.2\%)}$	370.25$^{(-3.0\%)}$	385.34 $^{(+1.0\%)}$
3	457.40	452.55 $^{(-1.1\%)}$	443.22$^{(-3.1\%)}$	461.29 $^{(+0.9\%)}$
4	558.38	557.46 $^{(-0.2\%)}$	554.98$^{(-0.6\%)}$	564.95 $^{(+1.2\%)}$
5	712.03	705.08 $^{(-1.0\%)}$	669.95$^{(-5.9\%)}$	718.35 $^{(+0.9\%)}$
6	796.90	800.08 $^{(+0.4\%)}$	738.91$^{(-7.3\%)}$	817.28 $^{(+2.6\%)}$
7	819.10	818.60 $^{(-0.1\%)}$	820.05$^{(+0.1\%)}$	836.18 $^{(+2.1\%)}$
8	957.09	986.91 $^{(+3.1\%)}$	1112.11$^{(+16.2\%)}$	1042.35 $^{(+8.9\%)}$
9	970.08	973.97 $^{(+0.4\%)}$	1271.02$^{(+31.0\%)}$	1063.11 $^{(+9.6\%)}$
10	985.93	998.63 $^{(+1.3\%)}$	-	1063.11 $^{(+7.8\%)}$
11	1008.35	998.63 $^{(-1.0\%)}$	939.38$^{(-6.8\%)}$	1020.18 $^{(+1.2\%)}$
12	1011.04	1039.43 $^{(+2.8\%)}$	-	1091.13 $^{(+7.9\%)}$

$(\ )^{(*\%)}$: $*$ *percentage different with respect to the* FEM_{3D-REF}.

Table 6.8. The first 12 frequencies considering the stringer with the L-shape.

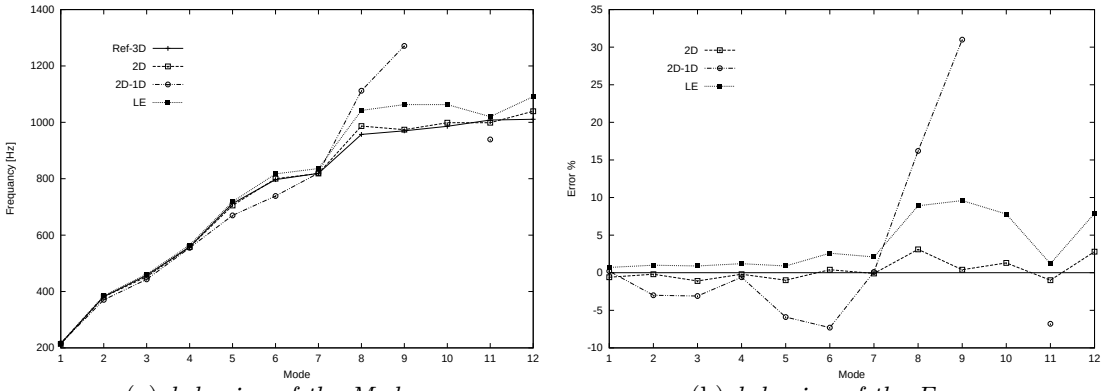

(a) *behavior of the Modes.* (b) *behavior of the Error.*

Figure 6.29. Results for the plate with the stringer with the L-shape.

6.32c and d show the *Shell* and $Shell - Beam$ FE models, respectively. In the *Shell* and $Shell - Beam$ FE models, the stringer is modeled including the offset.

The first 12 modes are used to compare the results, and they are shown in Fig.6.31. Tab.6.9 shows the results related to the first 12 considered modes. Mode 10 not appear in the *Shell* FE model, while the $Shell - Beam$ FE model is not able to find modes 11 and 12. Mode 12 is a local mode of the stringer.

The MAC highlights the capability of the LE refined model to obtain the nearest solution to the $3D$ solution, as shown in Fig.6.33. In fact, Fig.6.33a shows a linear matching between the $3D$ solution and the LE solution.

Again, in this case, the LE solution is almost linear, as shown in Fig.6.34a, and the LE error is almost constant for all the considered modes, as displayed in Fig.6.34b.

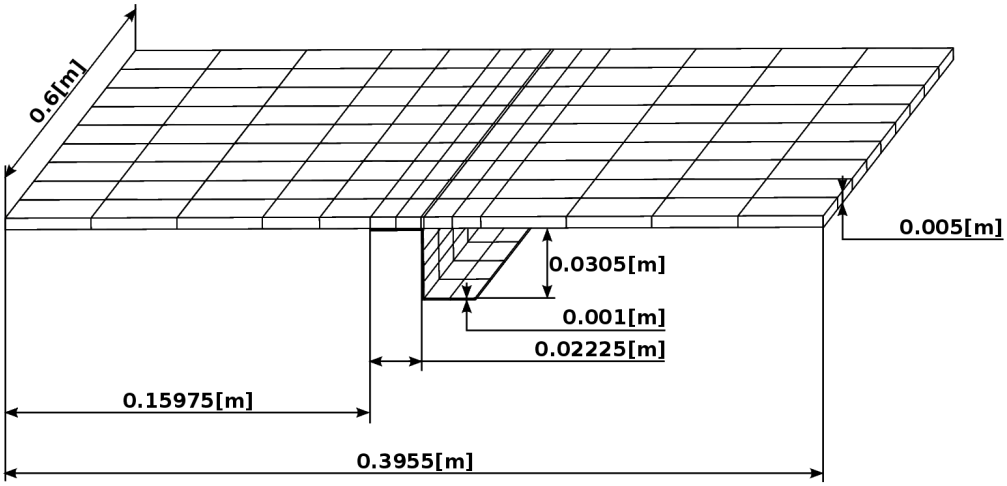

Figure 6.30. Reinforced plate with the stringer with the Z-shape.

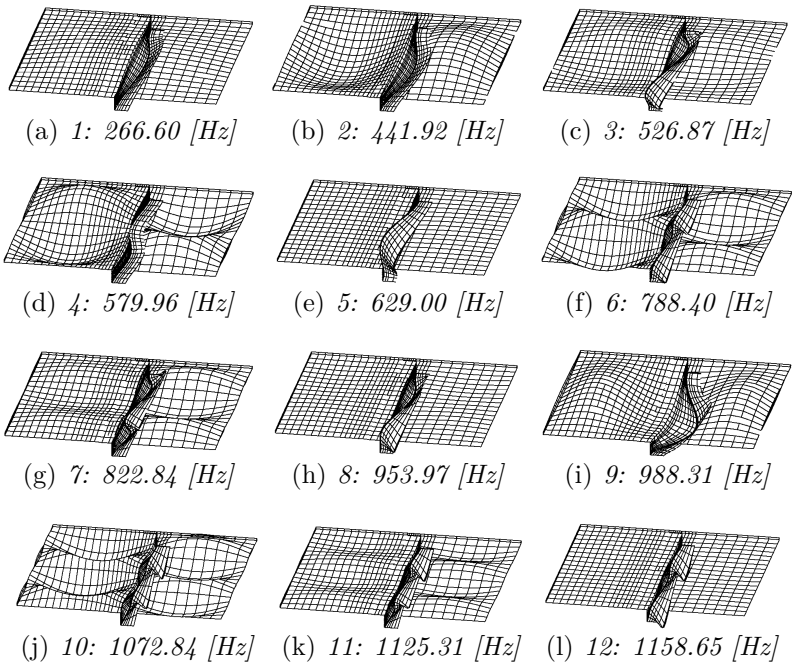

(a) *1: 266.60 [Hz]* (b) *2: 441.92 [Hz]* (c) *3: 526.87 [Hz]*

(d) *4: 579.96 [Hz]* (e) *5: 629.00 [Hz]* (f) *6: 788.40 [Hz]*

(g) *7: 822.84 [Hz]* (h) *8: 953.97 [Hz]* (i) *9: 988.31 [Hz]*

(j) *10: 1072.84 [Hz]* (k) *11: 1125.31 [Hz]* (l) *12: 1158.65 [Hz]*

Figure 6.31. The first 12 modes for the plate with the stringer with the Z-shape.

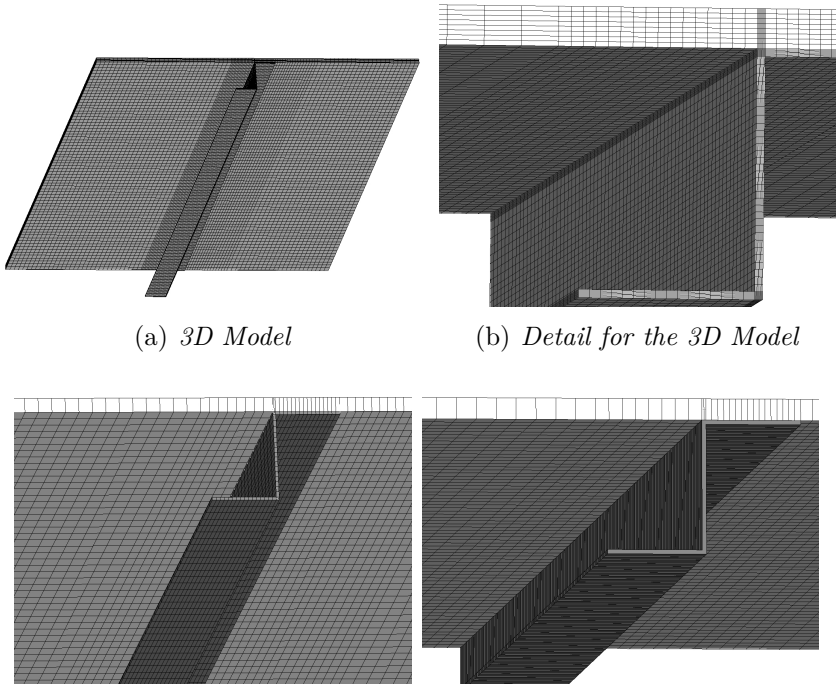

(a) *3D Model* (b) *Detail for the 3D Model*

(c) *Detail for the 2D Model* (d) *Detail for the 2D-1D Model*

Figure 6.32. Various models for the plate with the stringer with the Z-shape.

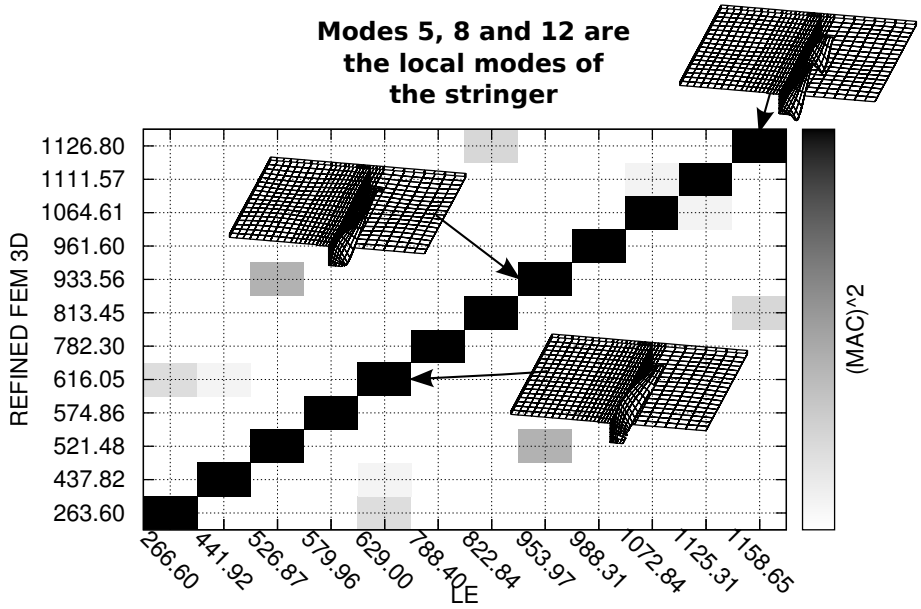

(a) *Refined FE Solid Model Vs LE Model.*

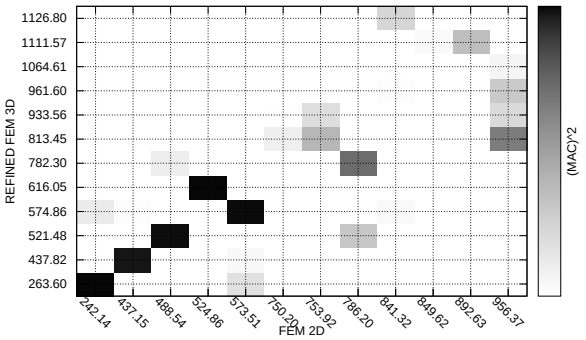

(b) *Ref 3D FE Model Vs 2D FE Model.*

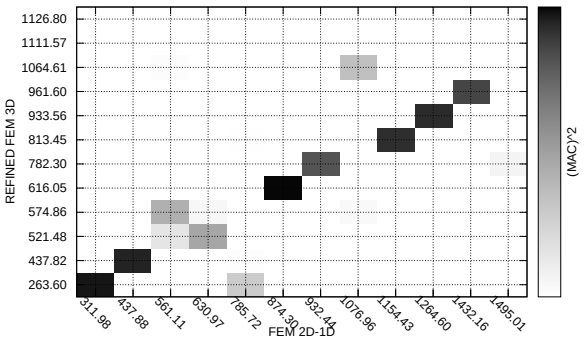

(c) *Ref 3D FE Model Vs 2D-1D FE Model.*

Figure 6.33. MAC using the stringer with the stringer with the Z-shape

Freq[Hz]	FEM_{3D-REF}	FEM_{2D}	FEM_{2D-1D}	LE
DOF	366147	65802	41748	8151
1	263.60	242.14 $^{(-8.1\%)}$	311.98 $^{(+18.4\%)}$	266.60 $^{(+1.1\%)}$
2	437.82	437.15 $^{(-0.2\%)}$	437.88 $^{(+0.0\%)}$	441.92 $^{(+0.9\%)}$
3	521.48	488.54 $^{(-6.3\%)}$	630.97 $^{(+21.0\%)}$	526.87 $^{(+1.0\%)}$
4	574.86	573.51 $^{(-0.2\%)}$	561.11 $^{(-2.4\%)}$	579.96 $^{(+0.9\%)}$
5	616.05	524.86 $^{(-14.8\%)}$	874.30 $^{(+41.9\%)}$	629.00 $^{(+2.1\%)}$
6	782.30	786.20 $^{(+0.5\%)}$	932.44 $^{(+19.2\%)}$	788.40 $^{(+0.8\%)}$
7	813.45	956.37 $^{(+17.6\%)}$	1154.43 $^{(+41.9\%)}$	822.84 $^{(+1.2\%)}$
8	933.56	956.37 $^{(+2.4\%)}$	1264.60 $^{(+35.5\%)}$	953.97 $^{(+2.2\%)}$
9	961.60	956.37 $^{(-0.5\%)}$	1432.16 $^{(+48.9\%)}$	988.31 $^{(+2.8\%)}$
10	1064.61	-	1076.96 $^{(+1.2\%)}$	1072.84 $^{(+0.8\%)}$
11	1111.57	892.63 $^{(-19.7\%)}$	-	1125.31 $^{(+1.2\%)}$
12	1126.80	841.32 $^{(-25.3\%)}$	-	1158.65 $^{(+2.8\%)}$

$(\ )^{(*\%)} : * \ percentage \ different \ with \ respect \ to \ the \ FEM_{3D-REF}.$

Table 6.9. The first 12 frequencies considering the stringer with the Z-shape.

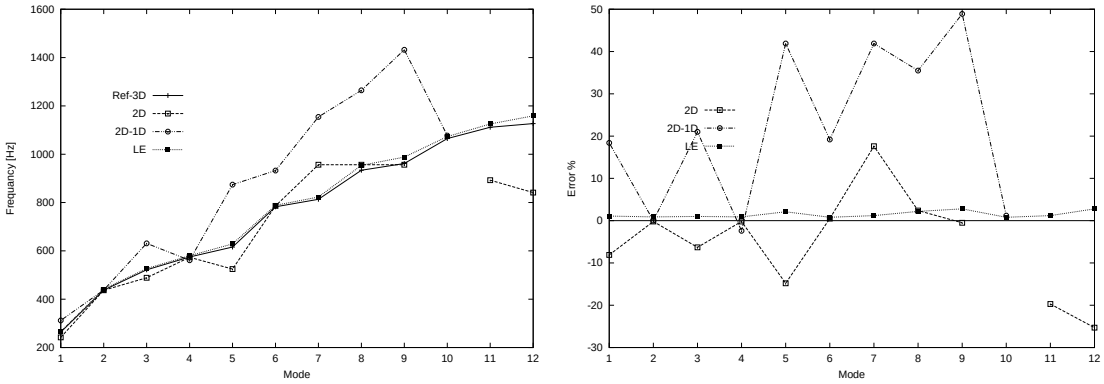

(a) *Behaviour of the Modes.* (b) *Behaviour of the Error.*

Figure 6.34. Results for the plate with the stringer with the Z-shape.

6.2 Curved panel

The structure shown in Fig.6.35 is investigated in this section. Fig.6.36 shows the geometry of the cross-section at $y = b/2$ and a loading configuration. Two asym-

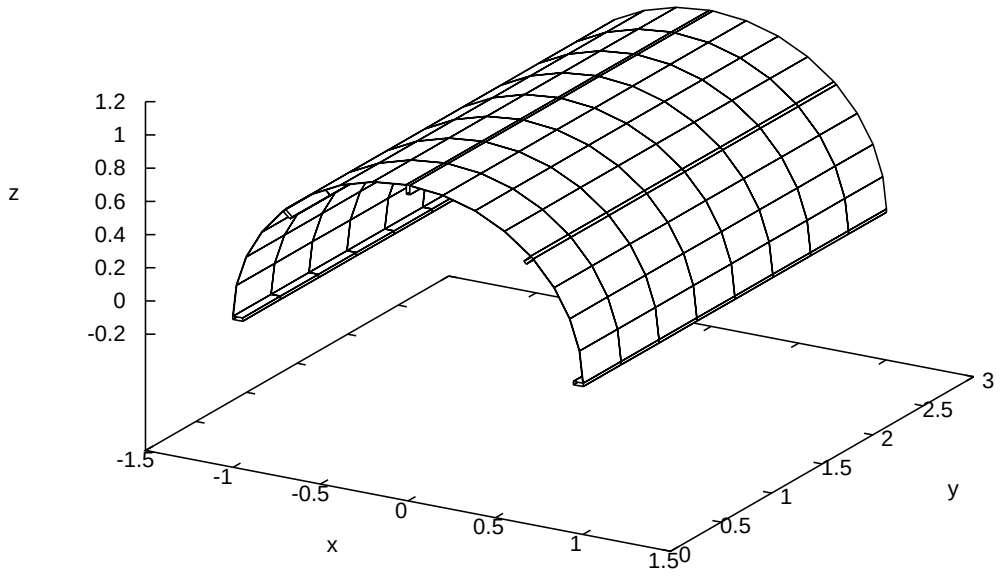

Figure 6.35. 3D model of the curved panel.

metric loads are considered with a magnitude of 500 [N]. The loads are applied at the mid-point of the beam length. The load F_1 is applied at the point A, and it is directed from the top to the bottom of the panel. The load F_2 applied at the point E with direction from the lower part of the upper part of the structure. The cross-section is characterized by a radius r of 1 [m], and the shell thickness is 0.002 [m]. Five longitudinal stringers are used and they are characterized by a rectangular cross-section. In particular, the sides m and p measure 0.054 [m] and 0.02 [m], respectively (see Fig.6.36). The beam length, b, measure 1.5 [m]. Two different FE models, built using the commercial NASTRAN® code, are considered. Fig.6.37 shows the solid FE model (FEM_{3D}). This is the main reference model because it has a high number of DOFs. Fig.6.38 shows the second FE model, it is a $shell - beam$ model. Shell elements are used for the skins while beam elements are used for the stringers, as shown in Fig.6.38. Four different models are used for

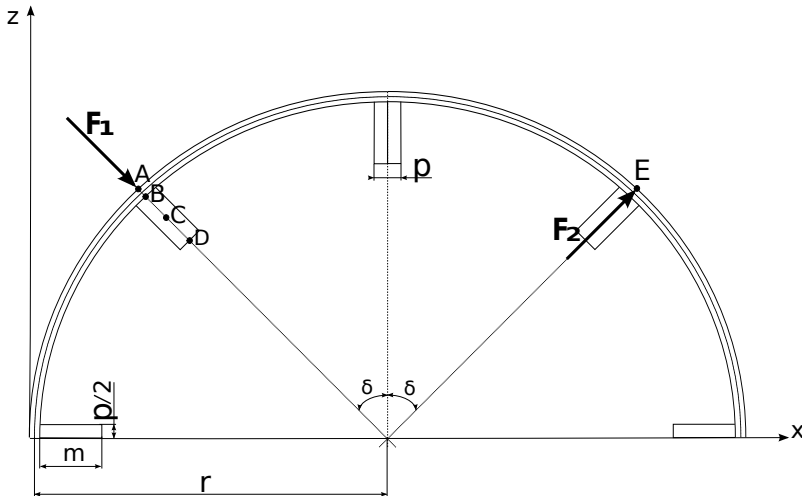

Figure 6.36. Geometry and load configuration in y=b/2 for the curved model.

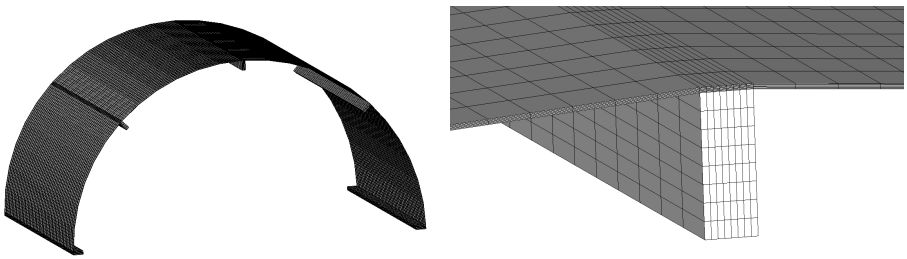

(a) *Global structure.* (b) *Local view.*

Figure 6.37. Solid FE Model with 346437 DOFs.

the LE model, in particular the LE models are called $S-1$, $S-2$, $S-3$, and $S-4$ with the cross-sections shown in the Fig.6.39. The four models have 1, 2, 3 and six elements between two stringers. Only nine-point LE elements are used to

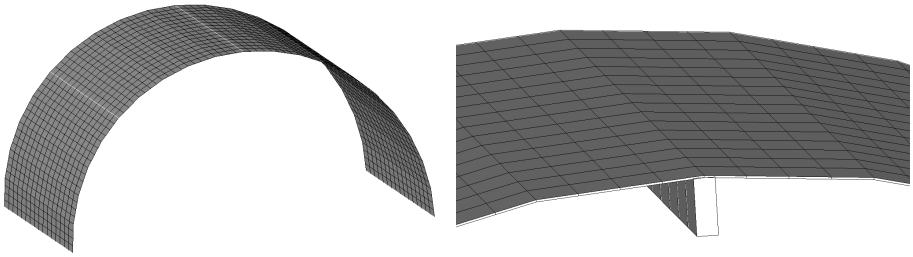

(a) *Global structure.* (b) *Local view.*

Figure 6.38. Shell/Beam FE Model.

built the $1D - CUF$ or LE models. Along the beam axis, the $S - 1$ and $S - 2$ models have $4 - B3$ beam elements, while the other two models have $8 - B4$ beam elements. The number of elements used on the cross-section has two effects on the

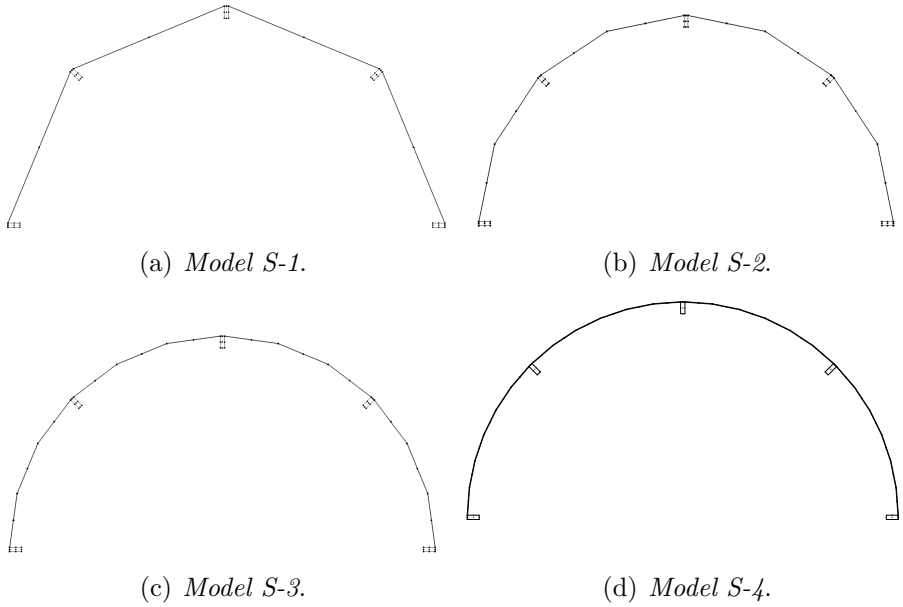

(a) *Model S-1.* (b) *Model S-2.*

(c) *Model S-3.* (d) *Model S-4.*

Figure 6.39. 1D CUF Models.

LE model, the former is a refinement of the kinematics model, while the latter is an improvement of the geometrical approximation of the curved panel. When a lower number of elements is used, the geometry of the model does not in fact accurately represent the real geometry.

6.2.1 Static analysis

The static analysis of the shown curved panel is investigated including displacement and stress fields analyses.

Displacement analysis

Fig.6.40 shows the vertical displacement on the cross-section at the mid-length point. In the figure, the results obtained with both $3D$ and $2D - 1D$ FE models are included. An amplification factor, $\times$ 1000, is used to plot the displacements. The displacements of the cross-section are shown in Tab.6.10.

Fig.6.36 shows the points where the u_x and u_z displacement components are evaluated. The displacement in the x-direction for the point A is called A_x, while along the z-direction it is called A_z. The percentage difference to the FEM_{3D} model

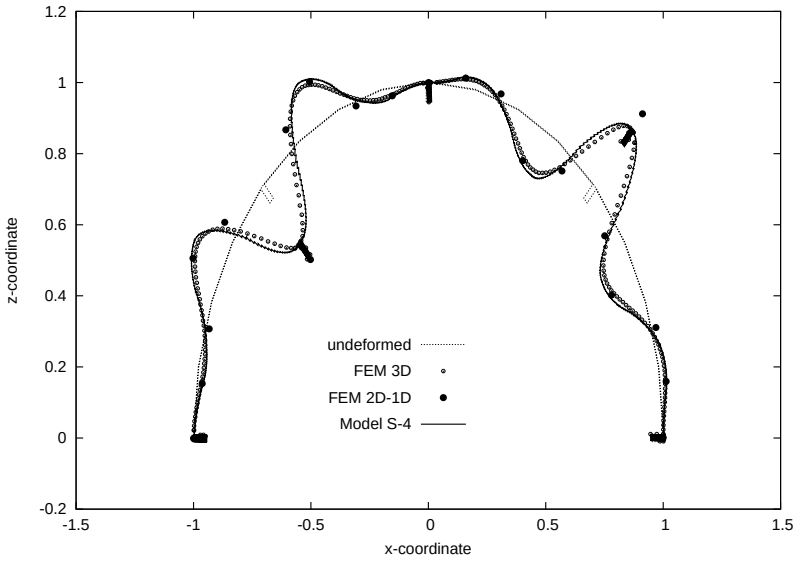

Figure 6.40. Displacement in y=b/2 × 1000 for the curved model.

Model	DOF	A_x	E_x	A_z	E_z
		$u_{x/z} \times 10^{-3}[m]$			
FEM_{3D}	346437	+0.1710	+0.1710	-0.1710	+0.1710
FEM_{2D-1D}	6030	$+0.2050^{(+19.9\%)}$	$+0.2050^{(+19.9\%)}$	$-0.2050^{(+19.9\%)}$	$+0.2050^{(+19.9\%)}$
$S-1$	2349	$+0.0167^{(-90.2\%)}$	$+0.0167^{(-90.2\%)}$	$-0.0170^{(-90.2\%)}$	$+0.0170^{(-90.2\%)}$
$S-2$	2997	$+0.0707^{(-58.7\%)}$	$+0.0707^{(-58.7\%)}$	$-0.0703^{(-58.9\%)}$	$+0.0703^{(-58.9\%)}$
$S-3$	3645	$+0.1242^{(-27.4\%)}$	$+0.1242^{(-27.4\%)}$	$-0.1245^{(-27.2\%)}$	$+0.1245^{(-27.2\%)}$
$S-4$	5589	$+0.1586^{(-7.3\%)}$	$+0.1586^{(-7.3\%)}$	$-0.1586^{(-7.3\%)}$	$+0.1586^{(-7.3\%)}$

$(\,)^{(*\%)}$: $*$ *percentage different to* FEM_{3D}

Table 6.10. Displacement at the selected points at $y = b/2$ for the curved panel.

is reported in superscript. According to the refined $S-4$ model, the error is lower than 9% on both the u_x and u_z components at the evaluated points. The $S-4$ DOFs are only 2% than the $3D$ DOFs. The $2D-1D$ FE model provide an error of about 20% with some DOFs nearest to the $S-4$ DOFs. The LE models, $S-1$ and $S-2$, provide inaccurate results because of the coarse mesh used on the cross-section.

Stress analysis

The axial stress is evaluated along the stringer where F_1 is applied. Four points are considered through the thickness, that is, points A, B, C and D, as shown in Fig.6.36. The error made using LE models depends on the mesh refinement, as

expected. However, LE gives a 3D stress field while the same stress components are not available when the combined beam/shell FE model is used. The σ_{yy} stress distribution is shown in Fig.6.41. The results are compared with respect those of

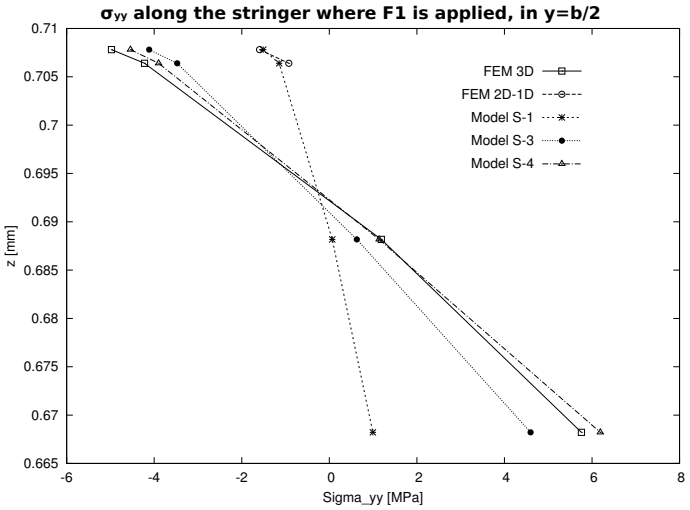

Figure 6.41. Stress analysis along the stringer in y=b/2 for the curved panel.

the $3D$ and $2D-1D$ FE models. When the $S-4$ model is used the solution is very close to the *Solid* solution. All the LE models gave better results than the $2D-1D$ model. Tab.6.11 shows the numerical results in terms of stress.

Model	DOF	A	B	C	D
FEM_{3D}	346437	-4975	-4222	+1187	+5758
FEM_{2D-1D}	6030	-1593$^{(-68.0\%)}$	-927 $^{(-78.0\%)}$	**	**
$S-1$	2349	-1181$^{(-76.3\%)}$	-946$^{(-77.6\%)}$	+80 $^{(-93.3\%)}$	+889$^{(-84.6\%)}$
$S-2$	2997	-2998$^{(-37.7\%)}$	-2412$^{(-42.9\%)}$	+259$^{(-78.4\%)}$	+2719$^{(-52.8\%)}$
$S-3$	3645	-4116$^{(-17.3\%)}$	-3475$^{(-17.7\%)}$	+629$^{(-47.0\%)}$	+4598$^{(-20.1\%)}$
$S-4$	5589	-4542$^{(-8.7\%)}$	-3900$^{(-7.6\%)}$	+1135$^{(-4.4\%)}$	+6189$^{(+7.5\%)}$

$(\ )^{(*\%)}$: $*$ *percentage different to* FEM_{3D}

$**$: *Not expected from the model*

Table 6.11. σ_{yy} in [KPa] along the stringer in $y = b/2$ for the curved panel.

The $S-4$ error is almost always below 9%. The stress analysis shows that the present 1D model can reduce the computational costs while preserving good accuracy. In this case, the $2D-1D$ model is not able to predict an accurate stress field although it has the same DOFs of the $S-4$ model. Along the stringer, the stress field can be analyzed for the kinematic beam element.

6.2.2 Free vibration analysis

This section deals with the free vibration analysis of thin-walled structures reinforced by longitudinal stiffeners using refined one-dimensional $1D$ models. The displacement field is obtained using Taylor (TE) and Lagrange (LE) Expansions function on the cross-section for the $1D-CUF$ models. The obtained results are compared with those from the classical finite element formulations based on plate and shell ($2D$), beam ($1D$) and solid ($3D$) elements that are available in commercial software. When TE models are used, different orders of expansion, N, are considered, where N is a free parameter of the formulation. As far as Lagrange expansions are concerned, four- ($LE4$) and nine-point ($LE9$) elements are used to build different cross-section.

The geometry of the curved panel is shown in Figure 6.35. Two different length values, b, are used along the y-axes: 1.5 [m] and 3.0 [m]. The cross-section is shown in Fig.6.36, where the radius is $R = 1$ m, the thickness is $t = 0.002$ m, and the stringers are located with an angular distance, α equal to 45°. The structure is clamped at both ends. Four $B3$ beam elements are used for the FEM approximation along the $y-axes$ for both the $1D-DUF$ models. Two different FE models are provided with the commercial $NASTRAN^{®}$ code, a refined $3D$ FE model and a $2D-1D$ FE model. Three different LE meshes are adopted on the cross-section, $S-2$, $S-3$ and $S-4$ shown in Fig.6.39b, c and d, respectively.

Tab.6.12 and Tab.6.13 show the first 12 frequencies for the structure with the length wqual to 1.5[m]. At the same way, Tab.6.14 and Tab.6.15 show the first 12 frequencies in the case on which b is equal to 3 [m].

Fig.6.42 shows the first 10 modal shapes with $TE6$ and $b = 3.0$ m.

In the case of the TE models, when N increases, a convergent solution is obtained. The convergence is faster in the case of $b = 3$, and a good agreement with the shell/beam solution is obtained. Tab.6.14 shows that the bending and torsional modes do not appear in the first 12 frequencies for either $N = 6$ or $N = 7$, and only shell-like modes appear, according to the MSC $NASTRAN^{®}$ results. However, the modes are all shell-likes when N is equal to 7, as showed in Tab.6.14. Moreover, when b is increased, the bending modes appear at lower frequencies, as expected. When LE is used, only shell-like modes are found. Better convergence can be expected for higher values of b. The number of LE elements on the cross-section is an important parameter for the accuracy of the solution. In fact, as shown in Tab.6.16, when the $S-4$ mesh is used, the first five modes are found, whereas only the first two frequencies are detected with the $S-3$ mesh.

Fig.6.43 shows how the first modal shape changes when different meshes are used on the cross-section. In fact, when the $S-2$ mesh is used (Fig.6.43a) the geometry is far from that of a curved panel and the first modal shape is not accurate.

Tab.6.16 shows that the $S-4$ results are accurate for both values of b but are

$fs\ [Hz]$	FEM_{3D}	FEM_{2D-1D}	$TE\ 5$	$TE\ 6$	$TE\ 7$
DOF	58344	8268	567	756	972
1	$103.57^{(S)}$	$97.17\ ^{(S)}$	$273.91^{(S)}$	$201.75^{(S)}$	$144.80^{(S)}$
2	$103.71^{(S)}$	$97.20\ ^{(S)}$	$285.15^{(S)}$	$216.98^{(S)}$	$176.98^{(S)}$
3	$107.41^{(S)}$	$103.78^{(S)}$	$370.98^{(S)}$	$312.46^{(S)}$	$178.93^{(S)}$
4	$109.67^{(S)}$	$104.55^{(S)}$	$422.72^{(S)}$	$351.50^{(S)}$	$225.73^{(S)}$
5	$110.98^{(S)}$	$107.00^{(S)}$	$581.28^{(B)}$	$397.69^{(S)}$	$265.18^{(S)}$
6	$118.48^{(S)}$	$114.75^{(S)}$	$629.20^{(S)}$	$450.63^{(S)}$	$306.59^{(S)}$
7	$124.85^{(S)}$	$120.84^{(S)}$	$646.50^{(S)}$	$521.70^{(S)}$	$313.95^{(S)}$
8	$128.19^{(S)}$	$124.22^{(S)}$	$664.51^{(S)}$	$532.63^{(S)}$	$334.96^{(S)}$
9	$149.35^{(S)}$	$141.16^{(S)}$	$711.18^{(S)}$	$549.11^{(S)}$	$391.30^{(S)}$
10	$151.10^{(S)}$	$143.30^{(S)}$	$767.06^{(S)}$	$560.56^{(S)}$	$454.75^{(S)}$
11	$154.73^{(S)}$	$147.84^{(S)}$	$792.85^{(S)}$	$590.02^{(S)}$	$506.35^{(S)}$
12	$159.07^{(S)}$	$150.12^{(S)}$	$862.26^{(S)}$	$661.63^{(S)}$	$512.47^{(S)}$

(B) *Bending* , (T) *Torsion* , (S) *Shell Like* , (A) *Axial*.

Table 6.12. The first 12 frequencies with TE and $b = 1.5[m]$ for the curved panel.

$fs\ [Hz]$	FEM_{3D}	FEM_{2D-1D}	$S-1$	$S-3$	$S-4$
DOF	58344	8268	2997	3645	5589
1	$103.57^{(S)}$	$97.17\ ^{(S)}$	$140.79^{(S)}$	$134.02^{(S)}$	$112.86^{(S)}$
2	$103.71^{(S)}$	$97.20\ ^{(S)}$	$143.97^{(S)}$	$140.87^{(S)}$	$115.68^{(S)}$
3	$107.41^{(S)}$	$103.78^{(S)}$	$157.72^{(S)}$	$149.31^{(S)}$	$122.74^{(S)}$
4	$109.67^{(S)}$	$104.55^{(S)}$	$176.69^{(S)}$	$162.85^{(S)}$	$123.90^{(S)}$
5	$110.98^{(S)}$	$107.00^{(S)}$	$203.56^{(S)}$	$177.70^{(S)}$	$130.24^{(S)}$
6	$118.48^{(S)}$	$114.75^{(S)}$	$203.78^{(S)}$	$180.94^{(S)}$	$135.08^{(S)}$
7	$124.85^{(S)}$	$120.84^{(S)}$	$241.91^{(S)}$	$192.79^{(S)}$	$138.69^{(S)}$
8	$128.19^{(S)}$	$124.22^{(S)}$	$276.43^{(S)}$	$196.14^{(S)}$	$144.87^{(S)}$
9	$149.35^{(S)}$	$141.16^{(S)}$	$285.23^{(S)}$	$241.06^{(S)}$	$155.72^{(S)}$
10	$151.10^{(S)}$	$143.30^{(S)}$	$317.62^{(S)}$	$245.12^{(S)}$	$165.53^{(S)}$
11	$154.73^{(S)}$	$147.84^{(S)}$	$353.68^{(S)}$	$252.87^{(S)}$	$169.94^{(S)}$
12	$159.07^{(S)}$	$150.12^{(S)}$	$365.49^{(S)}$	$290.80^{(S)}$	$172.86^{(S)}$

(B) *Bending* , (T) *Torsion* , (S) *Shell Like* , (A) *Axial*.

Table 6.13. The first 12 frequencies with LE and $b = 1.5[m]$ for the curved panel.

still better for $b = 3$, as previously mentioned. As shown in Tab.6.16, the number of LE elements on the cross-section has an important effect on the solution, especially for $b = 1.5$ [m], because shell-like modes appear in the first frequencies. When b is equal 3, both the refined and coarse meshes give accurate results for the first four

$fs\ [Hz]$	FEM_{3D}	FEM_{2D-1D}	$TE\ 5$	$TE\ 6$	$TE\ 7$
DOF	106485	16038	567	756	972
1	$41.02^{(S)}$	$39.76^{(S)}$	$95.98\ ^{(S)}$	$80.74\ ^{(S)}$	$72.00\ ^{(S)}$
2	$41.44^{(S)}$	$40.17^{(S)}$	$100.78^{(S)}$	$88.33\ ^{(S)}$	$84.67\ ^{(S)}$
3	$43.75^{(S)}$	$42.12^{(S)}$	$196.25^{(S)}$	$144.96^{(S)}$	$127.25^{(S)}$
4	$46.65^{(S)}$	$44.85^{(S)}$	$197.38^{(S)}$	$174.84^{(S)}$	$159.17^{(S)}$
5	$50.23^{(S)}$	$48.57^{(S)}$	$208.31^{(S)}$	$184.60^{(S)}$	$179.63^{(S)}$
6	$51.38^{(S)}$	$50.41^{(S)}$	$246.41^{(S)}$	$236.92^{(S)}$	$244.91^{(S)}$
7	$53.04^{(S)}$	$51.69^{(S)}$	$302.46^{(B)}$	$259.75^{(S)}$	$261.01^{(S)}$
8	$59.03^{(S)}$	$57.58^{(S)}$	$306.62^{(S)}$	$284.46^{(B)}$	$266.26^{(S)}$
9	$68.67^{(S)}$	$67.03^{(S)}$	$394.13^{(S)}$	$350.37^{(S)}$	$309.54^{(S)}$
10	$83.52^{(S)}$	$82.48^{(S)}$	$398.83^{(S)}$	$355.18^{(S)}$	$342.78^{(S)}$
11	$83.92^{(S)}$	$82.79^{(S)}$	$488.44^{(B)}$	$369.10^{(S)}$	$352.75^{(S)}$
12	$85.07^{(S)}$	$82.97^{(S)}$	$554.37^{(S)}$	$423.16^{(S)}$	$378.00^{(S)}$

(B) *Bending* , (T) *Torsion* , (S) *Shell Like* , (A) *Axial*.

Table 6.14. The first 12 frequencies with TE and $b = 3.0[m]$ for the curved panel.

$fs\ [Hz]$	FEM_{3D}	FEM_{2D-1D}	$S-2$	$S-3$	$S-4$
DOF	106485	16038	2997	3645	5589
1	$41.02^{(S)}$	$39.76^{(S)}$	$46.31\ ^{(S)}$	$44.16\ ^{(S)}$	$32.34^{(S)}$
2	$41.44^{(S)}$	$40.17^{(S)}$	$46.46\ ^{(S)}$	$44.17\ ^{(S)}$	$44.17^{(S)}$
3	$43.75^{(S)}$	$42.12^{(S)}$	$65.68\ ^{(S)}$	$45.84\ ^{(S)}$	$45.54^{(S)}$
4	$46.65^{(S)}$	$44.85^{(S)}$	$67.78\ ^{(S)}$	$51.01\ ^{(S)}$	$50.27^{(S)}$
5	$50.23^{(S)}$	$48.57^{(S)}$	$90.96\ ^{(S)}$	$60.34\ ^{(S)}$	$55.56^{(S)}$
6	$51.38^{(S)}$	$50.41^{(S)}$	$93.23\ ^{(S)}$	$90.85\ ^{(S)}$	$59.48^{(S)}$
7	$53.04^{(S)}$	$51.69^{(S)}$	$97.01\ ^{(S)}$	$94.94\ ^{(S)}$	$62.86^{(S)}$
8	$59.03^{(S)}$	$57.58^{(S)}$	$118.59^{(S)}$	$99.63\ ^{(S)}$	$69.33^{(S)}$
9	$68.67^{(S)}$	$67.03^{(S)}$	$133.62^{(S)}$	$111.17^{(S)}$	$79.95^{(S)}$
10	$83.52^{(S)}$	$82.48^{(S)}$	$135.47^{(S)}$	$111.97^{(S)}$	$98.90^{(S)}$
11	$83.92^{(S)}$	$82.79^{(S)}$	$150.56^{(S)}$	$115.78^{(S)}$	$101.97^{(S)}$
12	$85.07^{(S)}$	$82.97^{(S)}$	$159.17^{(S)}$	$124.42^{(S)}$	$106.08^{(S)}$

(B) *Bending* , (T) *Torsion* , (S) *Shell Like* , (A) *Axial*.

Table 6.15. The first 12 frequencies with LE and $b = 3.0[m]$ for the curved panel.

frequencies because they are related to the bending phenomena. In addition, the $S-4$ DOFs are about the half than the FEM_{2D-1D} DOFs, as shown in Tab.6.16.

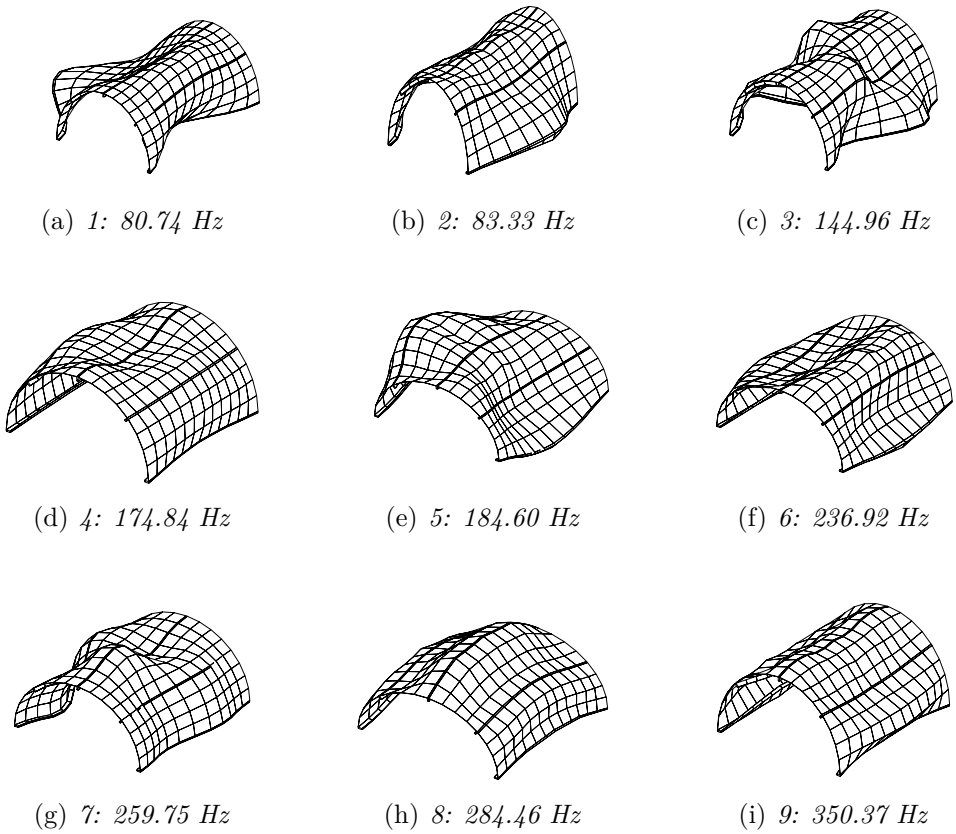

(a) *1: 80.74 Hz* (b) *2: 83.33 Hz* (c) *3: 144.96 Hz*

(d) *4: 174.84 Hz* (e) *5: 184.60 Hz* (f) *6: 236.92 Hz*

(g) *7: 259.75 Hz* (h) *8: 284.46 Hz* (i) *9: 350.37 Hz*

Figure 6.42. $TE6$ modes with $b = 3.0$ [m] for the curved panel.

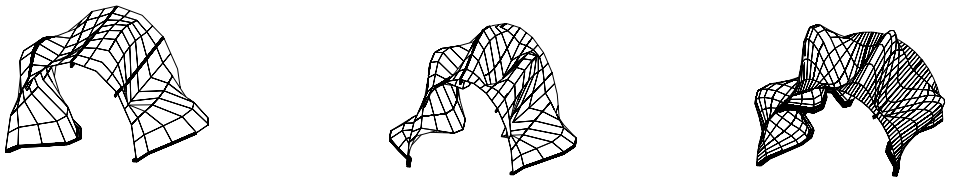

(a) $S-2$= *44.31 Hz* (b) $S-3$= *44.16 Hz* (c) $S-4$= *44.01 Hz*

Figure 6.43. Mode 1 using different LE mesh for the curved panel and $b = 3[m]$.

$fs\ [Hz]$	FEM_{3D}	FEM_{2D-1D}	$S-3$	$S-4$
DOF	106485	16038	3645	5589
		$b = 1.5\ [m]$		
1	103.57	$97.17^{(-6.4\%)}$	$140.87^{(+36.0\%)}$	$116.19^{(+12.2\%)}$
2	103.71	$97.20^{(-6.6\%)}$	$134.02^{(+29.2\%)}$	$115.08^{(+11.0\%)}$
3	107.41	$103.78^{(-3.1\%)}$	**	$123.53^{(+15.0\%)}$
4	109.67	$104.55^{(-4.7\%)}$	**	$130.37^{(+18.9\%)}$
5	110.98	$107.00^{(-4.2\%)}$	**	$134.13^{(+20.9\%)}$
		$b = 3\ [m]$		
1	41.02	$39.76^{(-1.9\%)}$	$44.16^{(+7.9\%)}$	$44.01^{(+7.3\%)}$
2	41.44	$40.17^{(-3.5\%)}$	$44.17^{(+6.1\%)}$	$44.17^{(+7.3\%)}$
3	43.75	$42.12^{(-4.6\%)}$	$45.84^{(+4.9\%)}$	$45.54^{(+5.3\%)}$
4	46.65	$44.85^{(-3.5\%)}$	$51.01^{(+8.4\%)}$	$50.27^{(+8.6\%)}$
5	50.23	$48.57^{(-2.8\%)}$	$90.85^{(+81.4\%)}$	$59.48^{(+10.6\%)}$

$(\ )^{(*\%)} : * \ percentage\ difference\ with\ respect\ to\ FEM_{3D}.$

$** : Mode\ Not\ Found.$

Table 6.16. Comparison of the first 5 natural frequencies for the curved panel.

Chapter 7

Analysis of parts of space vehicle

This chapter presents the static and dynamic analysis of parts of the launcher. In fact, launchers are made using many components. Panels, ribs, stringers are joined to obtain curved panels, very used for example to create an opening; reinforced cylindrical parts can be composed of different stringers and some ribs to increase the stiffeners of the skins. The approaches used to model these components depending on the number of elements used and on their positioning in the structure.

7.1 Reinforced cylindrical component

In this section, a thin-walled cylindrical component is considered. The structure is reinforced using eight longitudinal stringers and one rib located at half length. The boundary conditions used are clamped-clamped. Two different material configurations are treated; the first case considers only a standard aluminum allow for all the components, while in the second case both isotropic and orthotropic material are adopted.

The geometry of the cylindrical structure is shown in Fig.7.1, where the length, L, is equal to 15 m. Three components are used to build the whole structure. Fig. 7.2 shows the beam configuration, where the components 1 and 3 have the same cross-section (Fig. 7.3a).

The components 1 and 3 are thin-walled cylinders reinforced with eight stringers. The component 2 (Fig.7.3b) is a circumferential reinforcement or rib. The geometrical properties of both components are shown in Fig.7.3.

7.1.1 Free-Vibration Analysis of Metallic structure

TE and LE models are used in this section to evaluate classical beam modes, such as bending and torsional modes. The results are compared with those obtained using

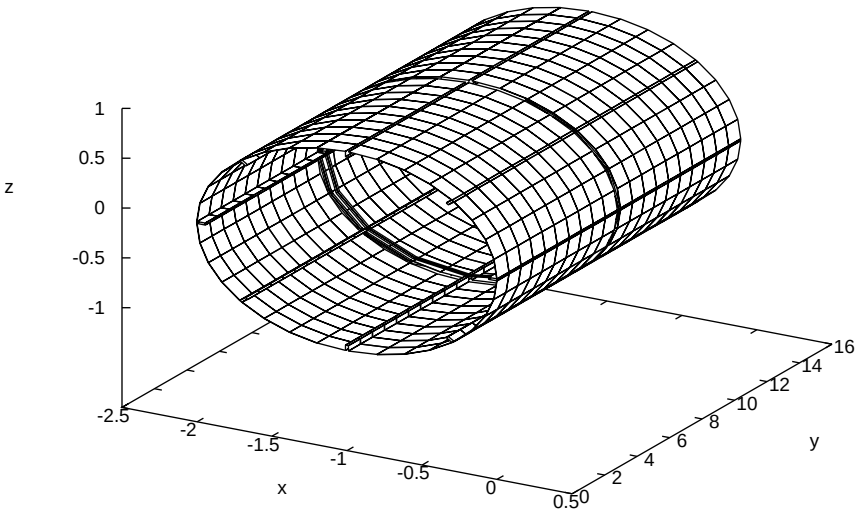

Figure 7.1. Reinforced cylinder model.

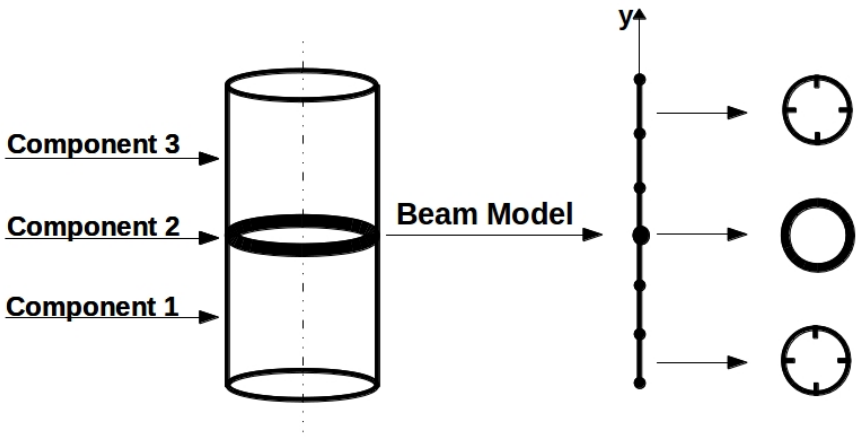

Figure 7.2. Component-wise representation of the reinforced cylinder.

two FE models built using the commercial NASTRAN® code. The $3D$ FE model is made using solid elements, while, in the $2D-1D$ FE model, the shell elements are used to simulate the skin while the beam elements are utilized for both stringers and rib, the correct offset from the skin is included in the beam properties. To evaluate the convergence of the solution for the TE models, different N orders of expansion are considered. The TE models are called $TE-N$, where N stands the

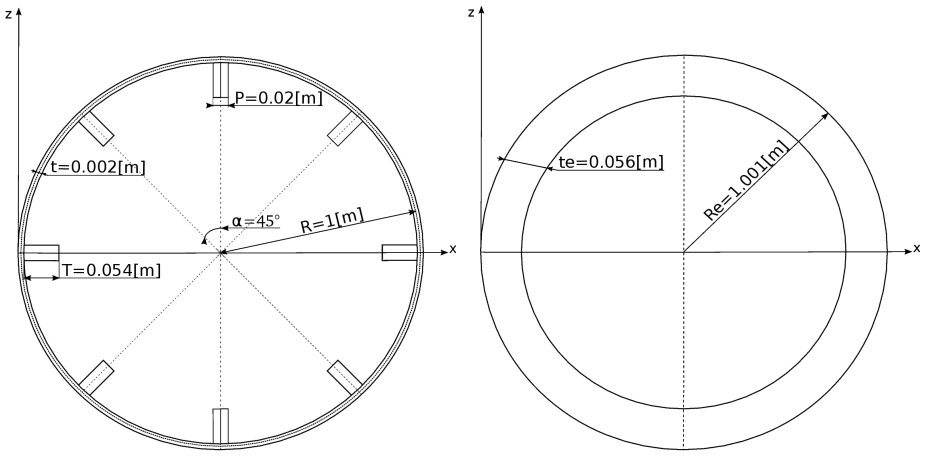

(a) *Component* 1 *and* 3. (b) *Component* 2.

Figure 7.3. Reinforced cylinder cross-section geometry.

expansion order. The LE model are called LE 24 because they are built using 24 nine-point elements over the cross-sections, as shown in Fig.7.4. Two different FEM approximations are used for the LE models. The LE 24 model considers four beam elements with quadratic interpolation (B3) for the components 1 and 3. The LE 24+ has eight cubic elements (B4) for the same components. For both LE models, component 2 has one cubic beam element (B3) along the axis.

The structure is realized using a standard aluminum alloy, with a value of Young modulus, E, equal to 75 GPa, the Poisson ratio, ν, equal to 0.3 and the value of density, ρ equal to 2700 kg/m^3. Tab.7.1 shows the first 15 frequencies evaluated using different TE models. When $TE-1$ and $TE-2$ are considered, only bending, axial and torsional modes can be found, because a coarse kinematic model is used. When the N-order increases, the model can identify more shell-like modes, and bending and torsional modes converge to $3D$ FE solution. Tab.7.2 shows the first 15 frequencies with both LE models. The LE 24+ shows more shell-like modes before the first bending frequency compared to LE 24 model, and also the bending frequency slightly decreases, as expected. Tab.7.3 presents the first two bending and torsional frequencies computed using different structural models. The first column reports the results evaluated by the solid FE model. The $3D$ FE results are accurate thanks to the refined mesh used, and then they are used as the reference. The $2D-1D$ FE model allows the number of DOFs to be drastically reduced. However, the FEM_{2D-1D} error is greater than 10% for the first bending and torsional frequencies. When the $TE-5$ model is used, the bending frequencies show an error close to 15%. Concerning the error for the torsional frequency, it is about 30% for the $TE-5$ model. The LE models provide results that are very close to the solid reference solution. Both the LE models provide an error close to 1% in the case of the

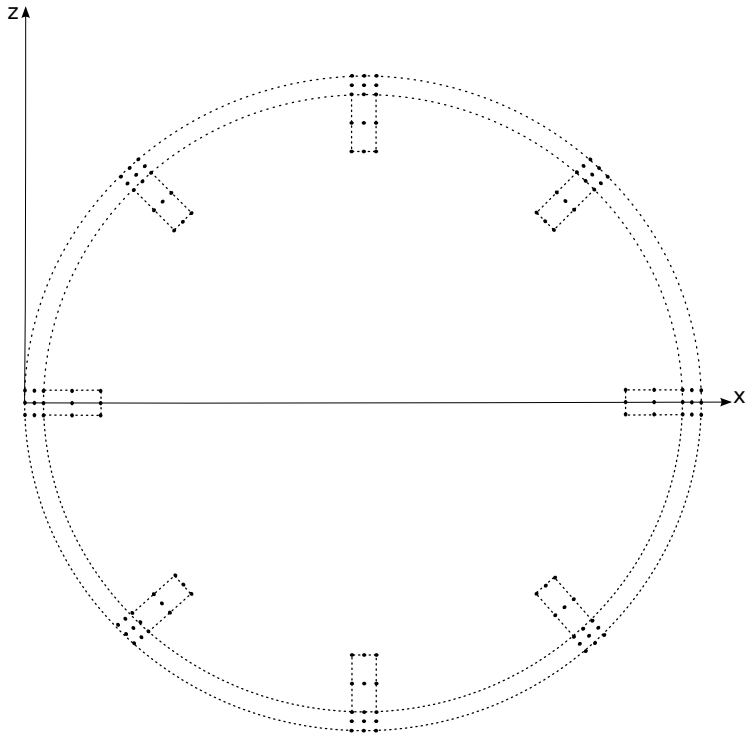

Figure 7.4. LE distretization of the cross-section for the reinforced cylinder.

first bending and torsional frequency, while, the error increases up to 6% when the second frequency is considered. The refined $1D-LE$ models appear more accurate compared to the FEM_{2D-1D} and TE models. However, the LE models still provide an error to the solid FE model for the second bending and torsional frequencies, but the LE DOFs are about 4% than the $3D$ FE DOFs. Convergence to the $3D$ FE solution can be observed using the $B4$ beam elements, as shown in Tab.7.3. Fig.7.5 shows the first bending mode for all the models, FEM_{3D}, FEM_{2D-1D}, $TE-5$ and LE 24+. Considering both the models obtained by a commercial code, both global and local effects are well detected, while, with TE and LE models, only global modes appear. In the case of TE models, theses result can be improved increasing the order of expansion N, while, for the LE models a refined cross-sectional mesh is required to detect local effects. Figures 7.6, 7.7 and 7.7 show that both TE and LE models are able to detect accurately the global behaviour of the reinforced cylindrical component.

$fs\ [Hz]$	$TE-1$	$TE-2$	$TE-3$	$TE-4$	$TE-5$
1	$42.25^{(B)}$	$42.90^{(B)}$	$38.98^{(B)}$	$38.92^{(B)}$	$38.79^{(B)}$
2	$42.25^{(B)}$	$42.90^{(B)}$	$39.04^{(B)}$	$38.97^{(B)}$	$38.94^{(B)}$
3	$91.53^{(T)}$	$91.53^{(T)}$	$78.01^{(S)}$	$70.05^{(S)}$	$53.24^{(S)}$
4	$120.66^{(A)}$	$123.04^{(B)}$	$78.09^{(S)}$	$70.14^{(S)}$	$53.28^{(S)}$
5	$121.95^{(B)}$	$123.05^{(B)}$	$91.53^{(T)}$	$83.28^{(S)}$	$67.21^{(S)}$
6	$121.95^{(B)}$	$147.57^{(A)}$	$107.50^{(B)}$	$83.29^{(S)}$	$70.47^{(S)}$
7	$193.06^{(B)}$	$195.24^{(B)}$	$107.71^{(B)}$	$91.53^{(T)}$	$70.48^{(S)}$
8	$193.06^{(B)}$	$195.24^{(B)}$	$120.87^{(S)}$	$102.77^{(S)}$	$77.27^{(S)}$
9	$220.66^{(T)}$	$220.66^{(T)}$	$120.88^{(S)}$	$102.78^{(S)}$	$91.53^{(T)}$
10	$281.81^{(T)}$	$281.81^{(T)}$	$147.33^{(A)}$	$107.27^{(B)}$	$92.78^{(S)}$
11	$295.96^{(A)}$	$307.28^{(B)}$	$162.12^{(B)}$	$107.43^{(B)}$	$92.80^{(S)}$
12	$305.67^{(B)}$	$307.29^{(B)}$	$162.46^{(B)}$	$147.28^{(A)}$	$107.18^{(B)}$
13	$305.68^{(B)}$	$357.06^{(A)}$	$162.66^{(S)}$	$147.84^{(S)}$	$107.36^{(B)}$
14	$373.53^{(A)}$	$379.54^{(B)}$	$162.67^{(S)}$	$147.88^{(S)}$	$133.75^{(S)}$
15	$377.38^{(B)}$	$379.55^{(B)}$	$220.63^{(T)}$	$161.43^{(B)}$	$139.39^{(S)}$

(B) *Bending* , (T) *Torsion* , (S) *Shell Like* , (A) *Assial*

Table 7.1. First 15 frequencies of the reinforced cylinder for the TE models.

$fs\ [Hz]$	$LE\ 24$	$LE\ 24+$
1	$18.51^{(S)}$	$17.43^{(S)}$
2	$18.67^{(S)}$	$17.46^{(S)}$
3	$26.22^{(S)}$	$25.10^{(S)}$
4	$26.24^{(S)}$	$25.11^{(S)}$
5	$30.74^{(S)}$	$30.26^{(S)}$
6	$30.80^{(S)}$	$30.34^{(S)}$
7	$31.63^{(S)}$	$30.48^{(S)}$
8	$31.89^{(S)}$	$30.55^{(S)}$
9	$34.17^{(B)}$	$31.66^{(S)}$
10	$34.55^{(B)}$	$31.74^{(S)}$
11	$35.93^{(S)}$	$33.99^{(B)}$
12	$36.45^{(S)}$	$34.14^{(B)}$
13	$43.39^{(S)}$	$42.35^{(S)}$
14	$43.51^{(S)}$	$42.38^{(S)}$
15	$68.64^{(S)}$	$46.71^{(S)}$

(B) *Bending* , (S) *Shell Like*

Table 7.2. The first 15 frequencies of the reinforced cylinder for the LE models.

$Mode$	FEM_{3D}	FEM_{2D-1D}	TE 5	LE 24	LE 24+
DOF :	390192	26206	2142	8352	15264
Bending	Frequencies:				
1^a	33.64	37.49 $^{(+11.4\%)}$	38.79 $^{(+15.3\%)}$	34.17 $^{(+1.6\%)}$	33.99 $^{(+1.0\%)}$
2^a	94.82	91.06 $^{(-4.0\%)}$	107.18$^{(+13.0\%)}$	88.89 $^{(-6.3\%)}$	89.07 $^{(-6.4\%)}$
Torsion	Frequencies:				
1^a	67.67	77.83 $^{(+15.0\%)}$	91.53 $^{(+35.3\%)}$	68.65 $^{(+1.4\%)}$	68.32 $^{(+0.9\%)}$
2^a	175.33	179.49$^{(+2.4\%)}$	220.63$^{(+25.8\%)}$	163.90$^{(-6.5\%)}$	162.90$^{(-7.6\%)}$

$(\ )^{(*\%)} : * \ Percentage\ difference\ with\ respect\ to\ 3D\ FE\ Model$

Table 7.3. The first two bending and torsional frequencies for the cylinder.

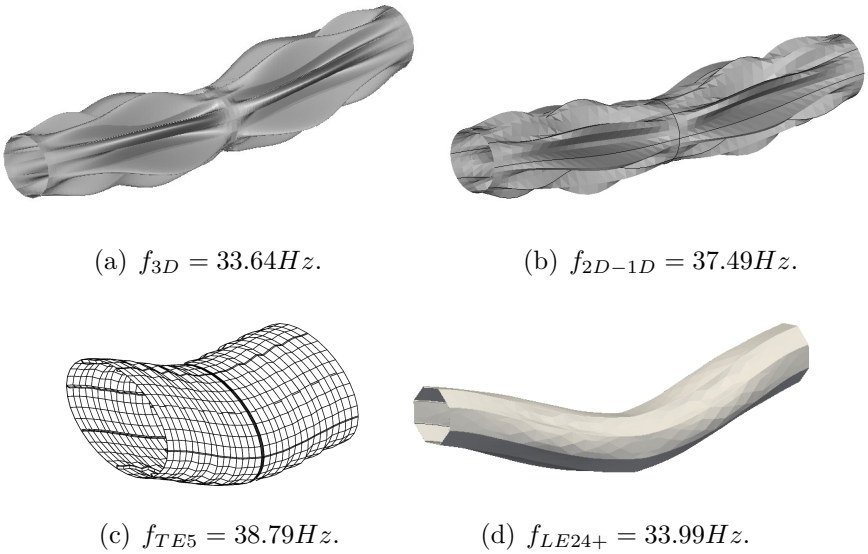

(a) $f_{3D} = 33.64Hz.$ (b) $f_{2D-1D} = 37.49Hz.$

(c) $f_{TE5} = 38.79Hz.$ (d) $f_{LE24+} = 33.99Hz.$

Figure 7.5. The first bending mode for the reinforce cylinder.

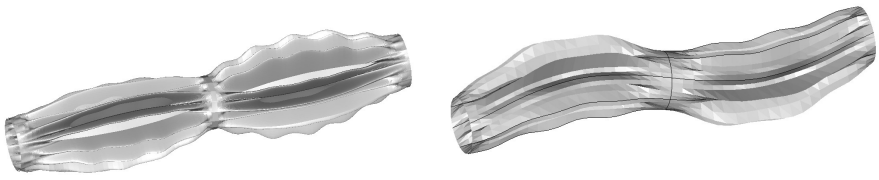

(a) $f_{3D} = 94.82Hz.$ (b) $f_{2D-1D} = 91.07Hz.$

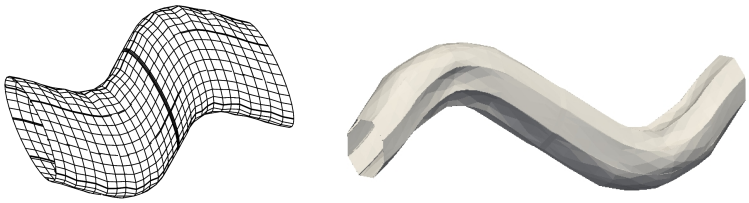

(c) $f_{TE5} = 107.18Hz.$ (d) $f_{LE24+} = 89.07Hz.$

Figure 7.6. the second bending mode for the reinforce cylinder.

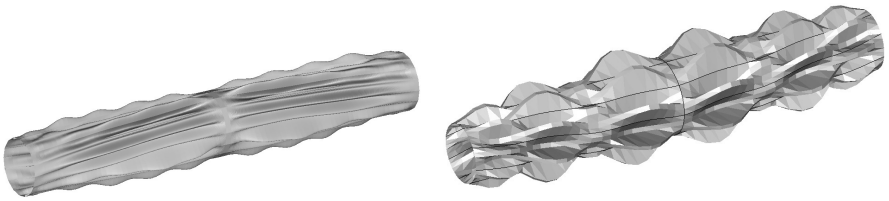

(a) $f_{3D} = 67.67Hz.$ (b) $f_{2D-1D} = 77.83Hz.$

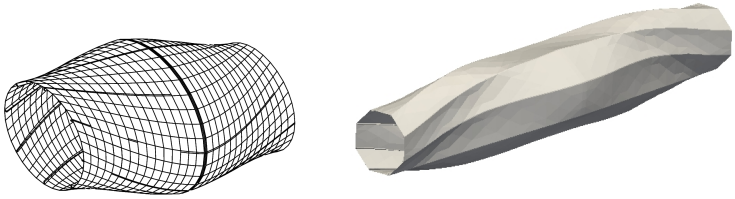

(c) $f_{TE5} = 91.53Hz.$ (d) $f_{LE24+} = 68.32Hz.$

Figure 7.7. The first torsional mode for the reinforce cylinder.

7.1.2 Free-Vibration Analysis of Composite structure

The structure analyzed is shown in Fig.7.1, and the Fig.7.3 shows the two cross-sections used to model the components. The capability of the $1D-CUF$ models in the analyses of the composite structure has been checked in the work of Cavallo et al. [a]. The stringers and the rib are realized using a classical aluminium alloy, with a value of Young modulus, E, equal to 75 GPa, the Poisson ratio, ν, equal to 0.3 and the value of density, ρ equal to 2700 kg/m^3. For the skins, a orthotropic material is used with E_{33} = 142 GPa, E_{22} = 9.8 GPa, E_{11} = 9.8 GPa, G_{32} = 6 Gpa, G_{31} = 6 Gpa, G_{21} = 4.83 Gpa, ν_{32} = 0.42, ν_{31} = 0.42, ν_{21} = 0.5 and ρ = 1445 kg/m^3. The boundary conditions are equal to the case above mentioned, clamped-clamped. Two different fibers orientations are used for the skins, in particular, the outer skin's fibers are oriented at an angle of +45°, while the inner skins are characterized by fibers oriented at an angle of -45°. Fig.7.8 contains some information about the geometrical configuration and the beam discretization.

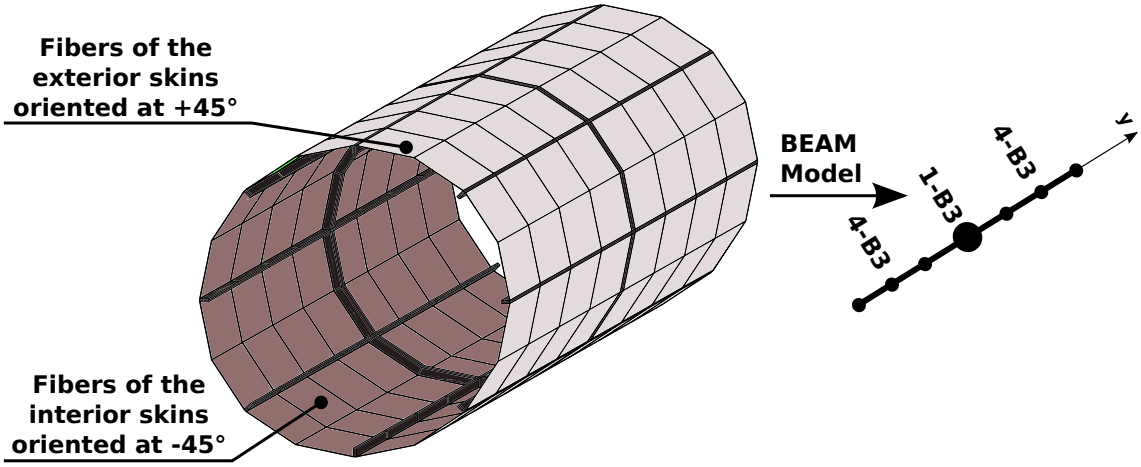

Figure 7.8. The layout for the composite reinforced cylinder.

Tab.7.4 shows the first 15 frequencies for the composite structure. The table also contains the results about the isotropic structure shown in the previous paragraph with the purpose to highlight the effect on the torsional frequencies due to the fibers oriented with an angle of ± 45°.

Tab.7.5 shows the first and second bending and torsional frequencies. The first three columns are related to the isotropic model proposed in the previous section. The last column contains the results using the composite layout. As has been said earlier, with the composite material the value for the bending frequencies are about similarly to the bending frequencies obtained using the isotropic material; in contrast, the torsional frequencies increase when the composite material is used.

$Mode$	$LE_{ISOTROPIC}$	$LE_{COMPOSITE}$
1	16.44	15.23
2	18.38	15.70
3	18.38	17.09
4	18.69	17.14
5	19.58	19.13
6	19.71	19.22
7	22.64	23.15
8	24.40	23.77
9	25.31	24.30
10	25.45	24.34
11	25.53	24.65
12	25.78	24.87
13	26.61	27.85
14	27.26	28.52
15	30.17	31.19

Table 7.4. The first 15 frequencies for the isotropic and composite structure.

$Mode$	FEM_{3D}	FEM_{2D-1D}	$LE_{ISOTROPIC}$	$LE_{COMPOSITE}$
DOF :	390192	26206	8352	16848
Bending	Frequencies [Hz]:			
1^a	33.64	37.49 $^{(+11.4\%)}$	34.23 $^{(+1.7\%)}$	34.16
2^a	94.82	91.06 $^{(-4.0\%)}$	93.85 $^{(-1.0\%)}$	101.31
Torsional	Frequencies [Hz]:			
1^a	67.67	77.83 $^{(+15.0\%)}$	73.18 $^{(+8.1\%)}$	90.90
2^a	175.33	179.49$^{(+2.4\%)}$	174.61$^{(-0.4\%)}$	283.49

Table 7.5. The effect of the composite layout on the torsional frequencies.

7.1.3 Load factor effect

The structure analyzed is the composite thin-walled cylinder shown in the section 7.1.2, where the information about the materials used and the boundary conditions are introduced. The aim of this part is to analyze the effect of a load factor in the free vibration analysis. Fig.7.9 shows the load factor N applied to the reinforced cylinder following the y-direction. According to the load factor direction, components 1 and 3 are subjected to two different load stress, in fact, component 1 is subjected to a compression stress, while component 3 is subjected to a tensile stress because the structure is clamped at both and.

Tab.7.6 shows the first 10 frequencies considering the load factor N. When N

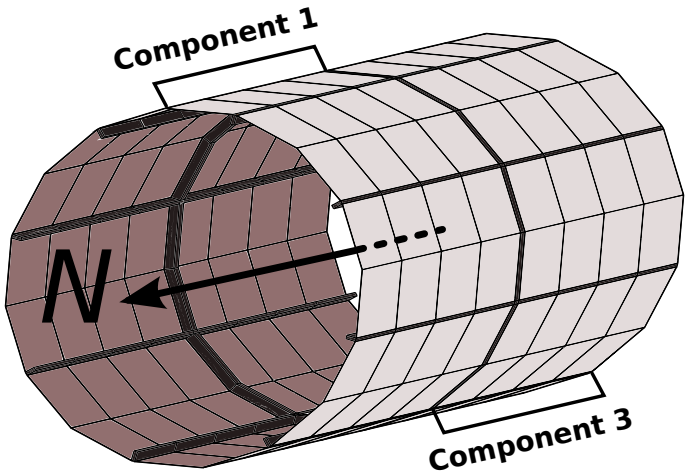

Figure 7.9. The Load factor N applied on the composite reinforced cylinder.

increases, globally the frequencies decrease, but two different behaviors can be analyzed for the frequencies. As shown in Fig.7.10, mode one without a load factor is characterized by four half-waves in both cylindrical components. When a load factor is applied, this mode can be found at two different frequencies, one for each cylindrical component. When N increases, for component 1 subjected to a compression stress, the frequencies decrease, in contrast for component 3 subjected to a tensile stress, when N increases the frequencies decrease.

This behavior is well known, in fact when a structure is subjected to a compression stress when the load increases the frequencies decreases and they converge to zero. The value of the load on which the frequency is zero is called Eulerian buckling load as shown in the works of Timoshenko [1961] and Matsunaga [1996]. Buckling is characterized by a sudden sideways failure of a structural member subjected to high compressive stress, where the compressive stress at the point of failure is less than the ultimate compressive stress that the material is capable of withstanding. Mathematical analysis of buckling often makes use of an "artificial" axial load eccentricity that introduces a secondary bending moment that is not a part of the primarily applied forces being studied. As an applied load is increased on a member, such as a beam, it will ultimately become large enough to cause the member to become unstable and is said to have buckled. The further load will cause significant and somewhat unpredictable deformations, possibly leading to complete loss of the member's load-carrying capacity. If the deformations that follow buckling are not catastrophic the member will continue to carry the load that caused it to buckle. If the buckled member is part of a larger assemblage of components such as a building, any load applied to the structure beyond that which caused the member to buckle will be redistributed within the structure. Theoretically, buckling is

caused by a bifurcation in the solution to the equations of static equilibrium. At a certain stage under an increasing load, the further load can be sustained in one of two states of equilibrium: a purely compressed state (with no lateral deviation) or a laterally-deformed state.

Mode	*No LF*	$N = 1$	$N = 2$	$N = 3$
1	15.23	15.08	13.96	10.52
2	15.70	15.74	14.03	10.81
3	17.09	16.17	14.90	11.11
4	17.14	16.28	16.08	11.75
5	19.13	19.59	16.87	14.61
6	19.22	19.61	17.38	15.46
7	23.15	20.90	18.76	16.34
8	23.77	21.34	20.17	17.87
9	24.30	21.47	20.22	18.34
10	24.34	26.30	25.28	20.61

Table 7.6. The first 10 frequencies considering also the load factor N.

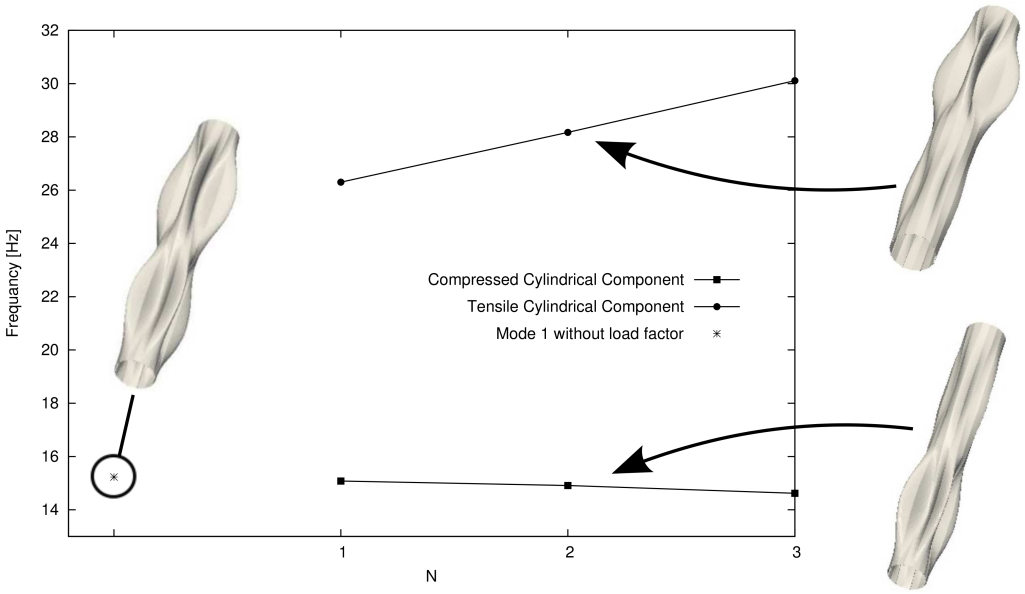

Figure 7.10. Load factor N on the composite reinforced cylinder.

Chapter 8

Free vibration analysis of launchers including non-structural masses

The aim of this section in to extend the structural 1D model based on the CUF to complex space structure. The structure considered is an outline of launcher inspired by the Arian V, European launcher. One of the objectives is to investigate the effect of the modeling adopted in both metallic and composite structure. Besides, the effect of the non-structural masses due to fuel and payload on the free vibration analysis is treated.

8.1 Global Geometry Configuration

The geometry of the outline of launcher analyzed is shown in Fig.8.1. The structure is composed of three main components, a central body and two lateral boosters joined with four connection points, as shown in Fig.8.2c. Eleven components are used along the beam axis to build this launcher structure. The bold black components are ribs, and they are shown in Fig.8.1. The other components are thin-walled cylinder reinforced using four stringers with an angle of 90°. Each component alone is a beam model, and the component-wise approach is used to obtain a unique one-dimensional model. Fig.8.2 shows the seven different cross-sections used to build the model. The rib components are proposed in Figures 8.2a, e, and g, and they are used for components 1, 5 and 9, respectively. The components 2, 4, 6, 8 and 10 are thin-walled cylinders with four longitudinal stringers. Their cross-sections are displayed in Figures 8.2b, d, and f. The sizes of the components of these seven cross-sections are shown in Tab.8.1. The rib components have only one cubic element along the beam axis while two cubic elements are used for the beam approximation for the

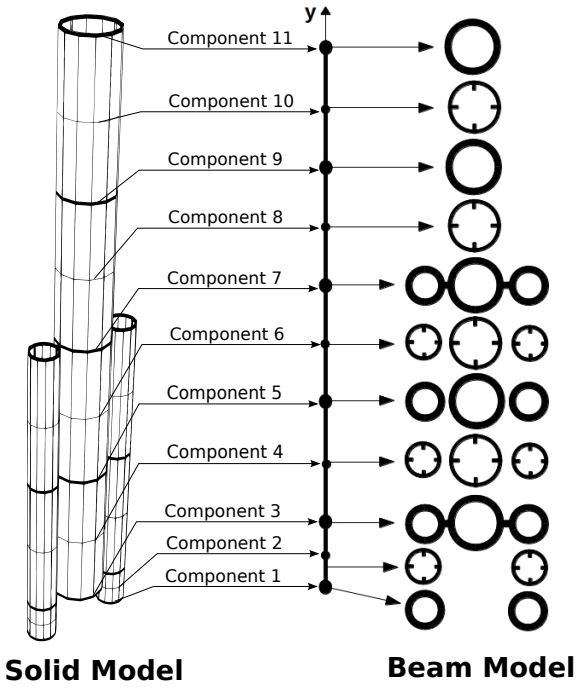

Figure 8.1. From the 3D to the 1D model of the Launcher.

other thin-walled components. Both stringers and connection points (CP) data are reported in Tab.8.2. A detail of cross-section 3 is shown in Fig.8.3.

8.2 Metallic Launcher

The first launcher analyzed is made using a standard aluminum aerospace alloy, with a value of Young modulus, E, equal to 75 GPa, the Poisson ratio, ν, equal to 0.3 and the value of density, ρ equal to 2700 kg/m^3.

8.2.1 Empty Launcher

The results obtained using the $1D$ CUF model are compared with those from two solid FE models analyzed using the commercial MSC NASTRAN® code.

Fig.8.4a shows the MSC NASTRAN solid FE model (called FE $Solid$ model, or $FE-3D$ model) with the same number of degrees of freedom, that is 29628, as the one-dimensional CUF model. Fig.8.4b shows the main solid FE model (called $Refined$ FE $Solid$ model, or $Refined$ $FE-3D$ model). The $Refined$ $FE-3D$ model is the refined model because has a very high number of DOFs, that is 197436 . The results are compared regarding natural frequencies and mode shapes, and in the

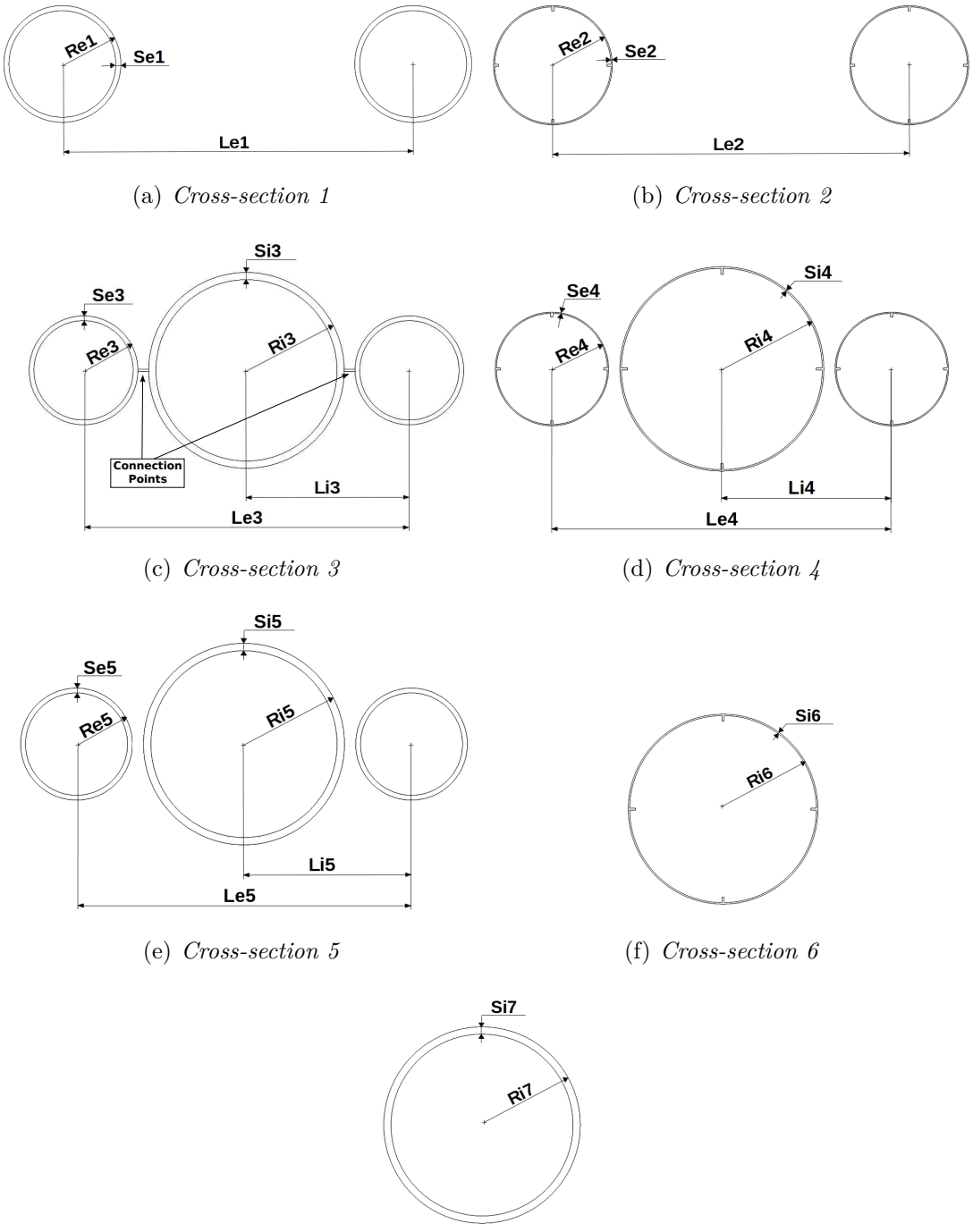

(a) *Cross-section 1*

(b) *Cross-section 2*

(c) *Cross-section 3*

(d) *Cross-section 4*

(e) *Cross-section 5*

(f) *Cross-section 6*

(g) *Cross-section 7*

Figure 8.2. Cross-section of the launcher components.

$ID\ Sec$	$Comp$	N_{BEAM}	$Cross-Section\ [m]$	$Lenght\ [m]$
1	1	1	$Re_1 = 1.50$	$h = 0.25$
			$Se_1 = 0.13$	
			$Le_1 = 9.00$	
2	2	2	$Re_2 = 1.50$	$h = 3.50$
			$Se_2 = 0.03$	
			$Le_2 = 9.00$	
3	3 / 7	1	$Re_3 = 1.50$ $Ri_3 = 2.70$	$h = 0.25$
			$Se_3 = 0.13$ $Si_3 = 0.20$	
			$Le_3 = 9.00$ $Li_3 = 4.50$	
4	4 / 6	2	$Re_4 = 1.50$ $Ri_4 = 2.70$	$h = 13.50$
			$Se_4 = 0.03$ $Si_4 = 0.04$	
			$Le_4 = 9.00$ $Li_4 = 4.50$	
5	5	1	$Re_5 = 1.50$ $Ri_5 = 2.70$	$h = 0.25$
			$Se_5 = 0.13$ $Si_5 = 0.20$	
			$Le_5 = 9.00$ $Li_5 = 4.50$	
6	8 / 10	2	$Ri_6 = 2.70$	$h = 13.50$
			$Si_6 = 0.04$	
7	9 / 11	1	$Ri_7 = 2.70$	$h = 0.25$
			$Si_7 = 0.20$	

N_{BEAM} : *Number of refined beam element along the* $y-axis$
h : *Component size along the* $y-axis$

Table 8.1. Geometrical data of the components of the launcher.

$Dimensions$	S_i	S_e	CP
Long side	0.16	0.10	0.30
Short side	0.06	0.06	0.06

S_i : *Stringers located in the central body*
S_e : *Stringers located in the lateral bodies*
CP : *Connection Points*

Table 8.2. Cross-sections data of the components of the launcher.

second case, the Modal Assurance Criterion (MAC) is used to evaluate the modal matching. Fig.8.5a shows the complete matching between the $1D\ CUF$ model and the $Refined\ FE-3D$ model for the first ten modes. Fig.reffig:Launcher1b shows the switching between mode 5 and mode 6 of the $FE-3D$ model and the $Refined\ FE-3D$ model, respectively. The results shown in Figures 8.5a and b are summarized in Tab.8.3. The natural frequencies show the best agreement to

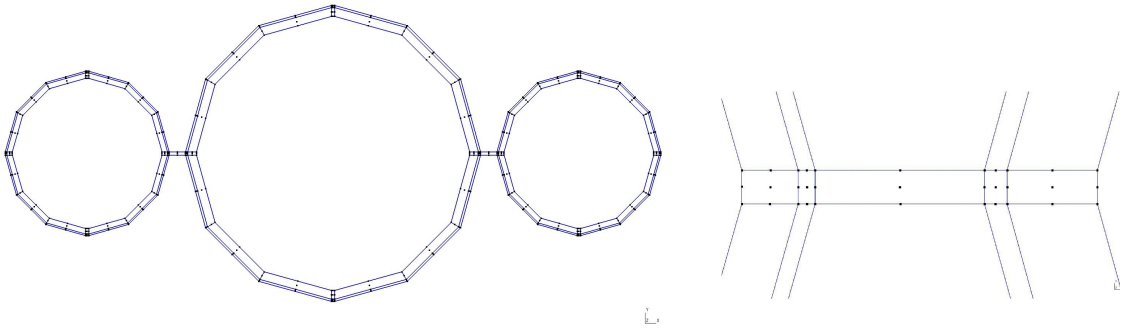

(a) *Cross – Section* (b) *Detail for the CP*

Figure 8.3. *LE* mesh of the area between the central body and the boosters.

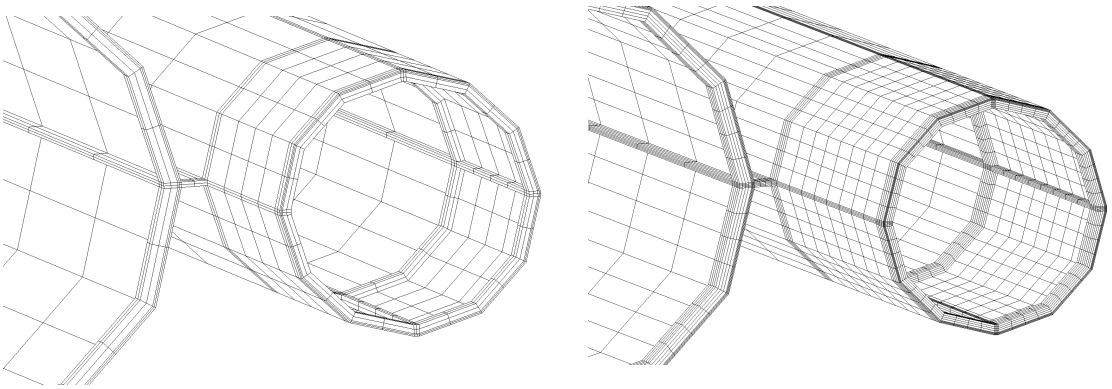

(a) *FE solid Model: 29628 DOFs* (b) *Refined FE solid Model: 197436 DOFs*

Figure 8.4. Refined FE Solid Model.

the $Refined\ FE-3D$ model is produced using the $1D\ CUF$ model. The error

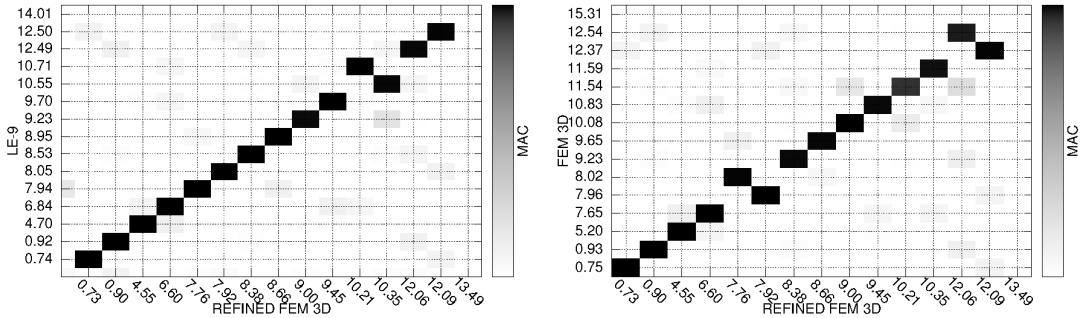

(a) *LE9 Vs Refined FE 3D Model.* (b) *FE 3D Model Vs Refined FE 3D Model.*

Figure 8.5. Comparison of the first 15 no rigid modes of various empty launcher.

MODE DOF	$REF\ FEM-3D$ 197436	$FEM-3D$ 29628	$LE9$ 29628
1	0.73	0.75 $^{(+2.7\%)}$	0.74 $^{(+1.4\%)}$
2	0.90	0.93 $^{(+3.3\%)}$	0.92 $^{(+2.2\%)}$
3	4.55	5.20 $^{(+14.3\%)}$	4.70 $^{(+3.3\%)}$
4	6.60	7.65 $^{(+15.9\%)}$	6.84 $^{(+3.6\%)}$
5	7.76	8.02 $^{(+3.4\%)}$	7.94 $^{(+2.3\%)}$
6	7.92	7.96 $^{(+0.5\%)}$	8.05 $^{(+1.6\%)}$
7	8.38	9.23 $^{(+10.1\%)}$	8.53 $^{(+1.8\%)}$
8	8.66	9.65 $^{(+11.4\%)}$	8.95 $^{(+3.3\%)}$
9	9.00	10.08$^{(+12.0\%)}$	9.23 $^{(+2.6\%)}$
10	9.45	10.83$^{(+14.6\%)}$	9.70 $^{(+2.6\%)}$
11	10.21	11.54$^{(+13.0\%)}$	10.71$^{(+4.9\%)}$
12	10.35	11.59$^{(+12.0\%)}$	10.55$^{(+1.9\%)}$
13	12.06	12.54$^{(+4.0\%)}$	12.49$^{(+3.6\%)}$
14	12.09	12.37$^{(+2.3\%)}$	12.50$^{(+3.4\%)}$

$(\ )^{(*\%)} : *$ *percentage difference with respect to refined FE3D Model*

Table 8.3. The first 15 Modes in [Hz] for the empty launcher.

committed by the $1D\ CUF$ model is under 4% for the first ten modes. The $1D$ CUF has only 15% of the DOFs of the $Refined\ FE-3D$ DOFs. Figure 8.6 shows

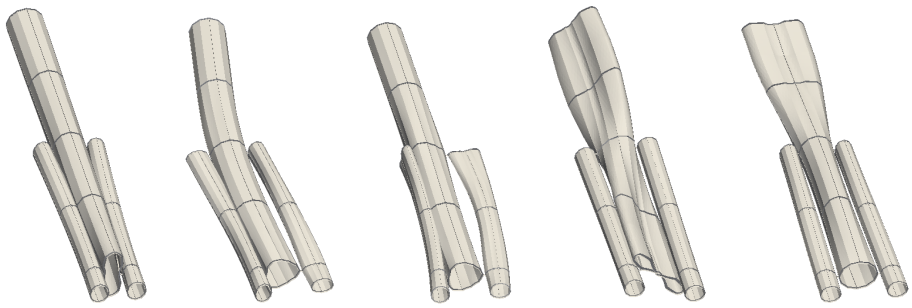

(a) $4.70Hz$. (b) $7.94Hz$. (c) $8.95Hz$. (d) $9.23Hz$. (e) $9.70Hz$.

Figure 8.6. Various modes for the $1D\ CUF$ Model.

some representative mode shapes of the $1D\ CUF$ model. The mode shapes shown global and local deformations. The last usually can be detected with two- and three-dimensional models. Both "local" and "global" modes can be obtained correctly, and the computational costs are significantly reduced compared to the $3DFE$ models.

8.2.2 Full launcher

The effect of solid fuel consumption on free vibration analysis is discussed in this section. The fuel mass and the payload are included in the model using lamped mass. Concerning the solid fuel consumption, only the solid fuel located in the boosters is considered. Three different consumptions are analyzed, radial, centripetal and axial consumption. The fuel mass and the payload are added, as shown in Fig.8.7a. Fig.8.7b shows the position of the masses at the central body. Each mass is located in the central node on the free edge of the stringers. The masses are spaced equally at about 3.375 [m] along the y direction in both the cryogenic main and upper stages, between two ribs. The payload masses are placed at 7 [m] from the top of the launcher. The solid fuel is exhausted in 140 seconds (Tab.8.4).

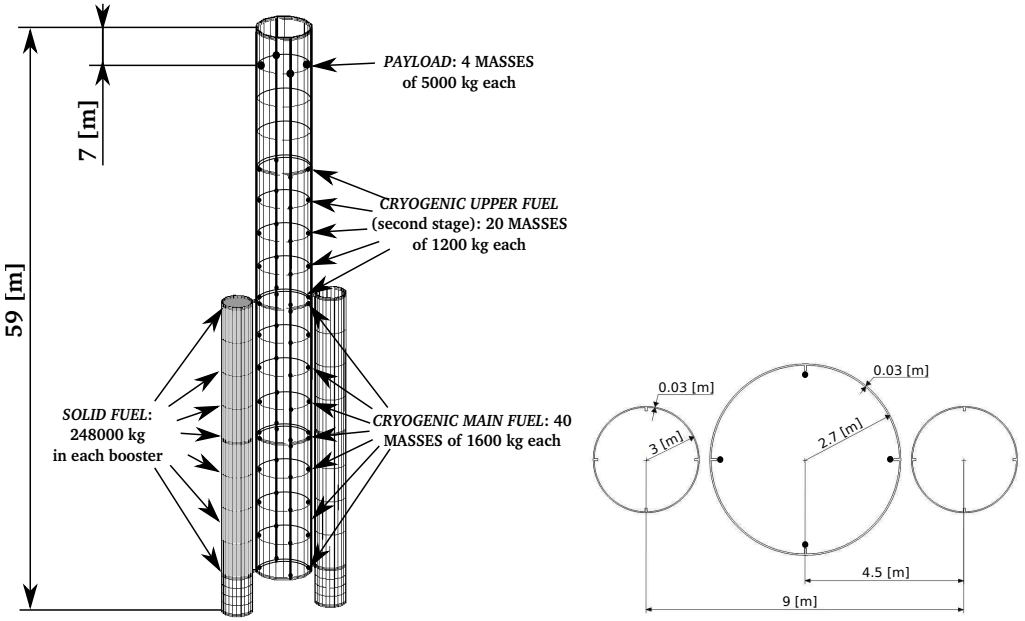

(a) *Total added mass.*

(b) *Positioning of the masses in the central body.*

Figure 8.7. Fuel and payload mass configurations for radial and centripetal cases.

Radial Consumption

In the case of radial consumption, the solid fuel burns from the inner to the outer part of the solid rockets (Fig.8.8). To model, the behavior of this consumption, 36 masses are used, and they are located at each cross-section of the solid booster (Fig.8.8a). The fuel consumption is simulated by activating or deactivating the masses.

Launcher Configuration	*Time* $[sec]$	*Solid Mass* $10^3[kg]$
100%	0	248.0
90%	14	223.2
80%	28	198.4
70%	42	173.6
60%	56	148.8
50%	70	124.0
40%	84	99.2
30%	98	74.4
20%	112	49.6
10%	126	24.8
0%	140	0.0

Table 8.4. Solid Fuel Consumption in each booster of the launcher.

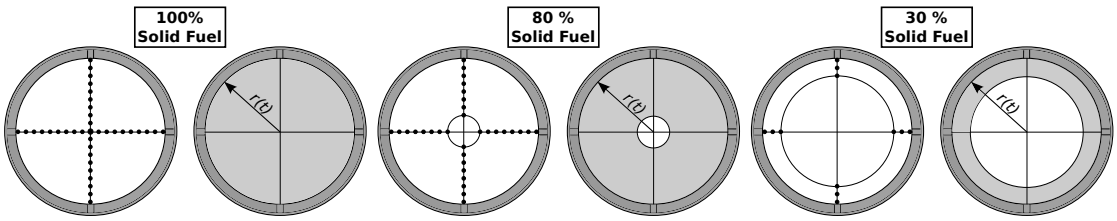

(a) *Full solid tank.* (b) *20% of solid fuel burned.* (c) *70% of solid fuel burned.*

Figure 8.8. Radial consumption in the boosters of the launcher.

Tab.8.5 shows the values of the natural frequencies for different fuel consumption stages.

Fig.8.9 contains the first five modes for the radial consumption. The subscript '$*$' represents the interpolated line of their relative mode. For example, '*Mode 1**' is the interpolation line for *Mode 1*. From the interpolation point of view, mode one and two show an almost linear behavior despite the interpolation law used is based on an exponential function. The first and the second modes are almost constant, while the other frequencies follow an exponential form.

Centripetal Consumption

Centripetal consumption is studied in this part. The same approach used in the radial fuel consumption case is again utilized but in this case, the solid fuel burns from the outer to the inner part of the solid booster, as shown in Fig.8.10. Tab.8.6 shows the first ten modes organized so that the same modal shape is contained in

MODE % Solid Fuel	1	2	3	4	5	6	7	8	9	10
100%	0.37	0.55	1.75	2.80	3.80	3.84	3.92	4.22	4.28	4.53
90%	0.38	0.55	1.77	2.90	3.86	3.89	3.96	4.30	4.35	4.71
80%	0.38	0.55	1.91	3.03	4.10	4.17	4.23	4.44	4.47	4.92
70%	0.38	0.55	2.02	3.16	4.27	4.37	4.42	4.59	4.59	5.15
60%	0.39	0.55	2.14	3.32	4.47	4.64	4.64	4.80	5.41	5.44
50%	0.40	0.56	2.29	3.51	4.85	5.00	4.85	5.13	5.69	5.80
40%	0.41	0.57	2.49	3.74	5.44	5.46	5.07	5.60	5.96	6.21
30%	0.44	0.59	2.73	4.01	5.96	6.01	5.30	6.24	6.46	6.65
20%	0.47	0.62	3.06	4.34	6.20	6.51	5.60	7.12	6.73	7.09
10%	0.54	0.67	3.53	4.74	6.25	6.76	5.99	8.59	7.11	7.42
0%	0.70	0.81	4.23	6.36	6.42	6.89	6.55	11.95	6.89	7.59

Table 8.5. The first 10 frequencies for different steps (Tab.8.4) and radial case.

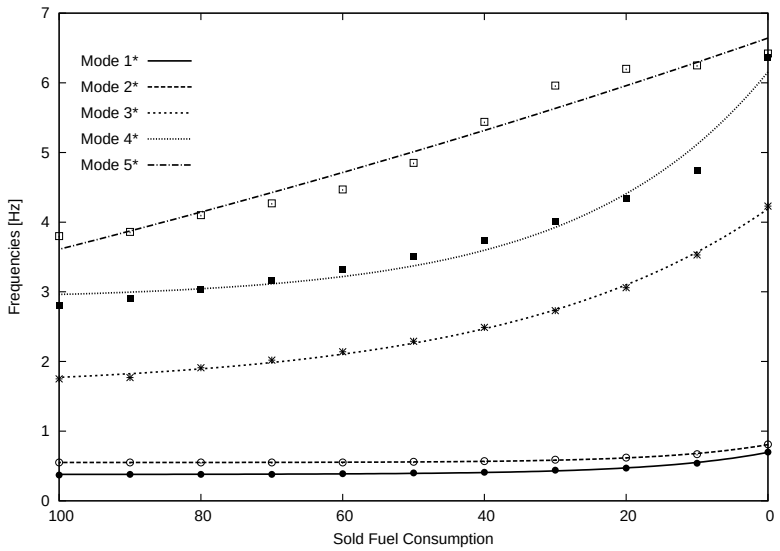

Figure 8.9. Exponential interpolation of the first 5 modes for the radial case.

each row of the table proposed.

Fig.8.11 shows again, in this case, an almost linear behavior for the first two no-rigid modes. According to the radial fuel consumption, the others frequencies considered are more sensitive to the mass variation.

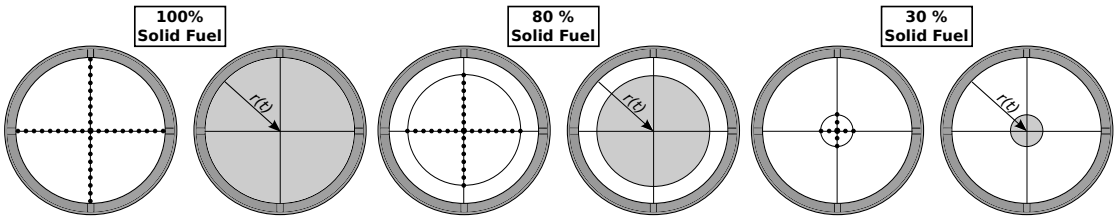

(a) *Full solid tank.* (b) *20% of solid fuel burned.* (c) *70% of solid fuel burned.*

Figure 8.10. Centripetal consumption in the boosters of the launcher.

MODE % Solid Fuel	1	2	3	4	5	6	7	8	9	10
100%	0.37	0.55	1.75	2.80	3.80	3.84	3.92	4.22	4.28	4.53
90%	0.40	0.58	1.82	2.91	3.96	4.01	4.05	4.31	4.35	4.70
80%	0.43	0.61	1.91	3.04	4.14	4.20	4.20	4.42	4.44	4.90
70%	0.46	0.64	2.02	3.18	4.34	4.38	4.45	4.59	4.55	5.14
60%	0.48	0.67	2.15	3.36	4.54	4.60	4.79	4.86	4.71	5.44
50%	0.51	0.69	2.30	3.54	4.73	4.81	5.22	5.27	4.97	5.80
40%	0.53	0.71	2.49	3.77	4.93	5.02	5.73	5.79	5.34	6.21
30%	0.55	0.72	2.73	4.03	5.18	5.27	6.31	6.46	5.84	6.67
20%	0.58	0.74	3.06	4.36	5.49	5.58	6.71	7.41	6.54	7.16
10%	0.62	0.76	3.53	4.75	5.89	5.99	6.83	8.94	7.66	7.44
0%	0.70	0.81	4.23	5.23	6.42	6.55	6.89	11.95	9.84	7.59

Table 8.6. The first 10 frequencies for different steps and centripetal case.

Axial Consumption

The Axial fuel consumption is considered in this section. In this case, the fuel burns from the bottom to the top in both boosters along the $y - direction$. Fig.8.12a shows the use of various masses along the y-direction to simulate a booster filled. The masses assume a value equal to zero in the case of fuel burned as shown in Fig.8.12b where to reproduce the case with 70% of solid fuel, the first three level of solid fuel are removed. Each column in the Tab.8.7 contains the frequencies related to the mode numbered in the first row.

Fig.8.13 shows the behavior of the first five frequencies regarding the axial consumption. Except mode five characterized by an almost constant behavior in the range from full configuration to about 20% of fuel, also in this configuration mode one and two follow a quasi-constant trend.

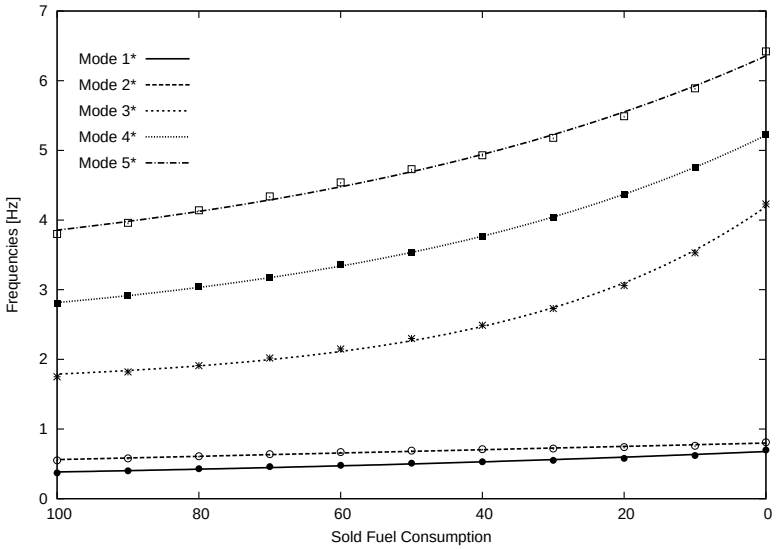

Figure 8.11. Exponential interpolation of the first 5 modes for the centripetal case.

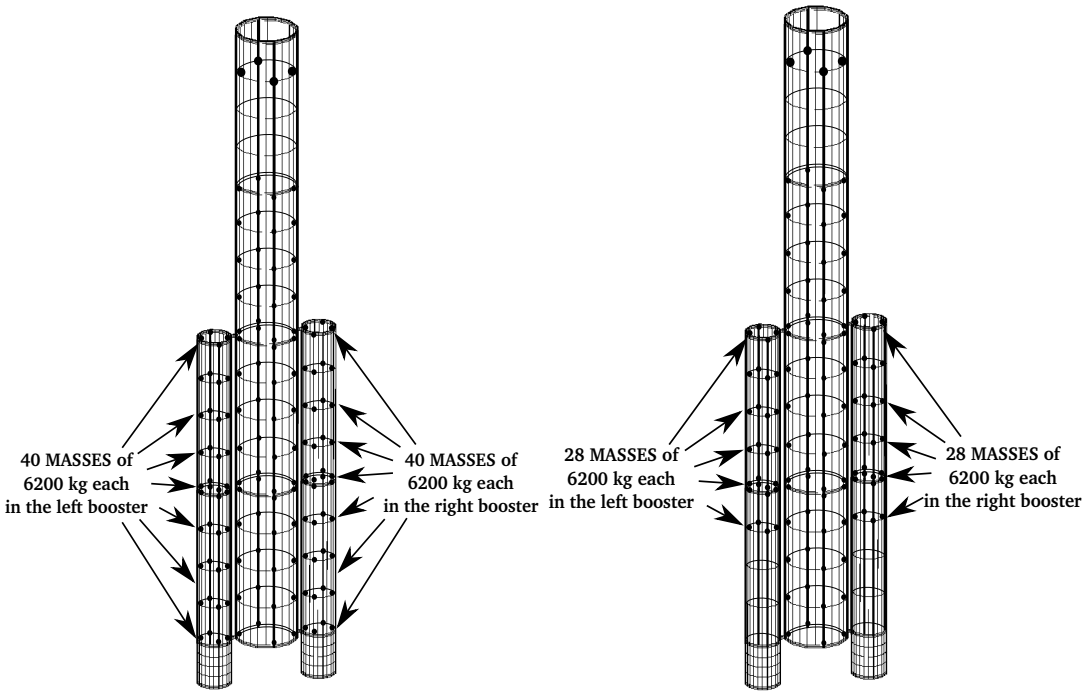

(a) *100% of solid fuel.* (b) *30% of solid fuel consumed.*

Figure 8.12. Symmetric Axial consumption in the boosters of the launcher..

Comparison of Centripetal, Radial and Axial Consumption

The results shown in the previous section demonstrate how a different configuration concerning the solid fuel burning can influence the behavior of the frequencies in the

Mode Solid Fuel	1	2	3	4	5	6	7	8	9	10
100%	0.28	0.41	1.57	2.63	3.27	3.85	4.00	4.21	4.37	4.42
90%	0.29	0.43	1.64	2.87	3.36	3.96	4.02	4.58	4.45	4.49
80%	0.30	0.44	1.72	3.13	3.41	4.23	4.07	4.74	4.83	4.50
70%	0.31	0.46	1.81	3.38	3.43	4.54	4.12	4.91	5.60	4.50
60%	0.32	0.48	1.93	3.61	3.44	4.80	4.18	5.16	5.83	4.58
50%	0.34	0.50	2.08	3.79	3.48	5.10	4.34	5.31	5.93	4.78
40%	0.37	0.52	2.24	4.05	3.52	5.55	4.49	5.39	6.04	4.94
30%	0.40	0.56	2.46	4.27	3.65	6.04	4.89	5.43	6.37	5.57
20%	0.44	0.60	2.78	4.36	3.95	6.11	5.59	5.50	7.34	6.11
10%	0.52	0.67	3.36	4.40	4.60	6.35	6.05	5.69	8.17	6.35
0%	0.74	0.92	4.70	4.70	7.94	7.94	9.70	8.05	14.01	7.94

Table 8.7. The first 10 frequencies for different steps (Tab.8.4) and axial case.

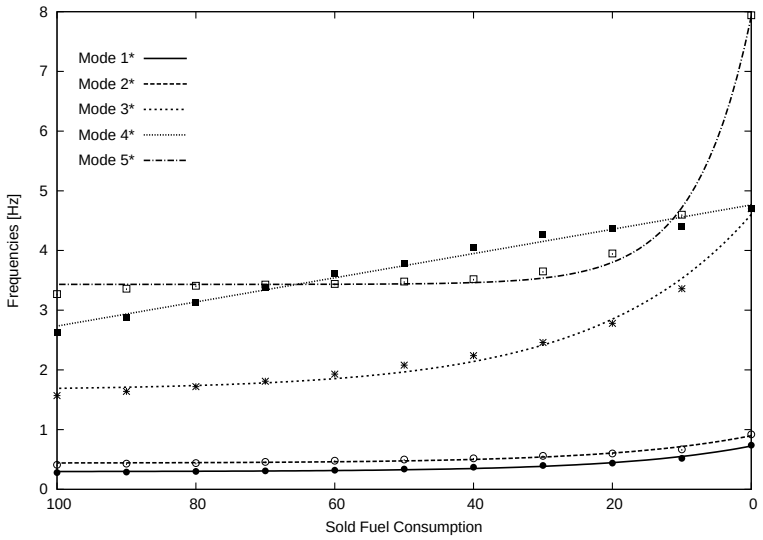

Figure 8.13. Exponential interpolation of the first 5 modes for the axial case.

free vibration analysis. The previously analysis can move on different approximate conclusions, in particular, mode one and two do not depend on the type of criterion used for the solid fuel. This analysis does not permit to highlight the best method to burn the solid fuel. An accurate analysis for the first two modes can help to give more information about the present status. Fig.8.14a and Fig.8.14b show the behavior of mode one and two, respectively, for all the case considered.

By focusing on the first two modes, only the centripetal fuel consumption ensures an almost linear variation for the natural frequencies when the solid fuel is burning.

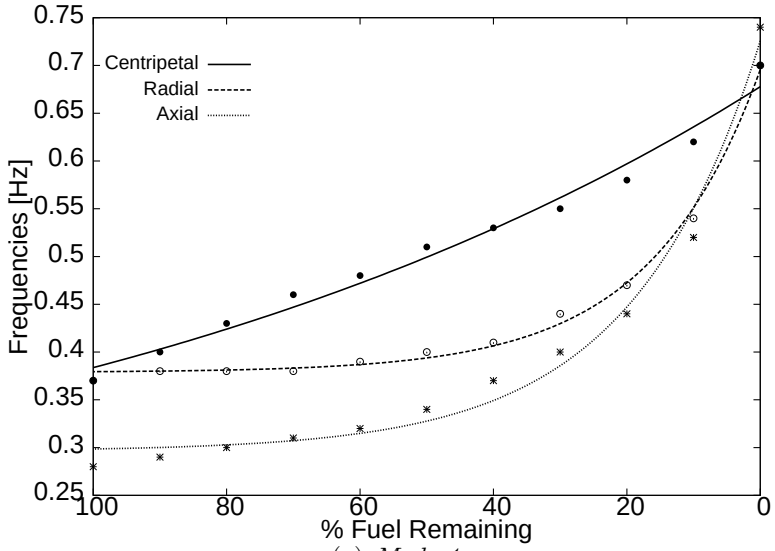

(a) *Mode 1.*

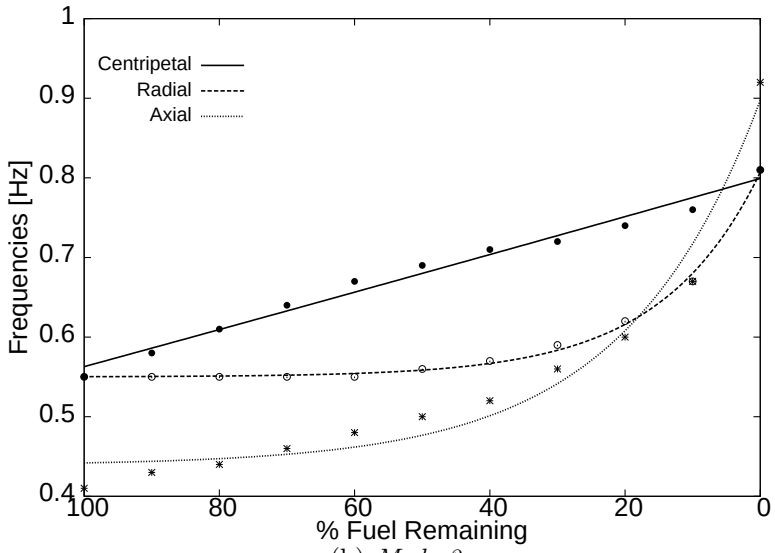

(b) *Mode 2.*

Figure 8.14. Exponential interpolation for the first two modes.

In the cases previously discussed, the scale used did not permit to highlight this detail.

8.3 Composite structure

The aim of this section is to analyze the effect of composite material on free-vibration analysis of the outline of launcher. The geometry of the launcher considered is shown in section 8.1. The composite layout is shown in Fig.8.15, and two different materials are used. The stringers and the rib are realized using a classical aluminium alloy, with a value of Young modulus, E, equal to 75 GPa, the Poisson ratio, ν, equal to 0.3 and the value of density, ρ equal to 2700 kg/m^3, while for the skins, a orthotropic material is used with E_{33} = 142 GPa, E_{22} = 9.8 GPa, E_{11} = 9.8 GPa, G_{32} = 6 Gpa, G_{31} = 6 Gpa, G_{21} = 4.83 Gpa, ν_{32} = 0.42, ν_{31} = 0.42, ν_{21} = 0.5 and ρ = 1445 kg/m^3. Two different fibers orientation are used for the skins, in particular for the outer skins fibers are oriented with an angle of +45°, while the inner skins are characterized by fibers oriented with an angle of -45°, as shown in Fig.7.8, where some information about the beam discretization are included.

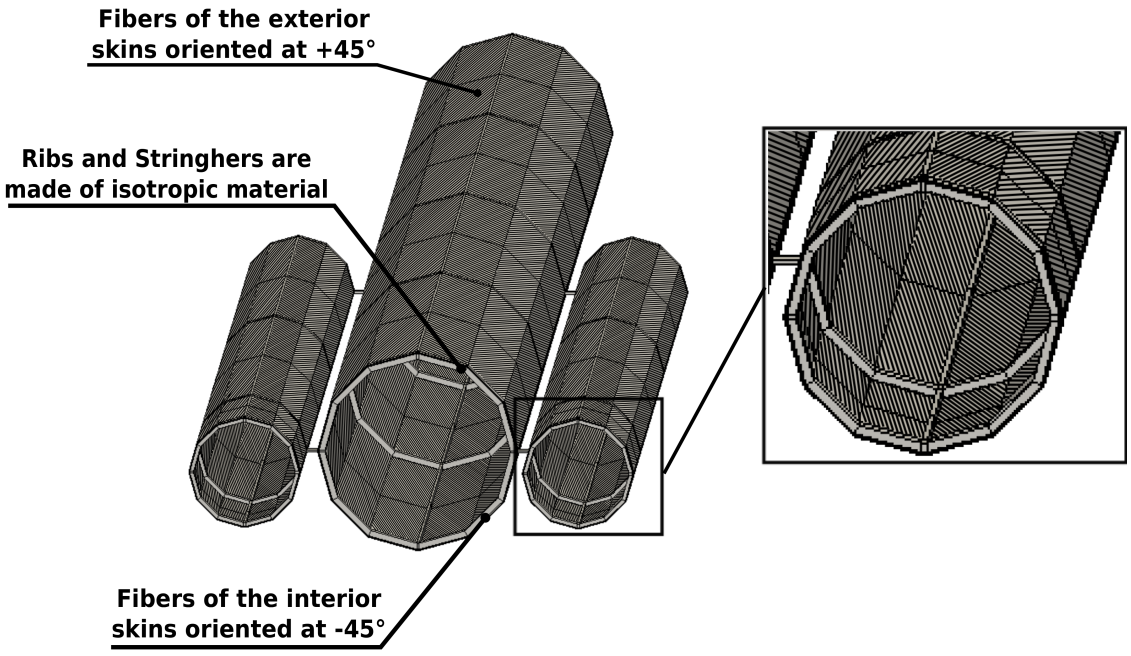

Figure 8.15. Global layout for the composite launcher.

8.3.1 Empty Composite Launcher

The goal of this section is to extend the mechanical model to the analysis of a composite launcher. First of all, the case without masses added, fuel and payload masses, is considered to obtain the values of the first fifteen no-rigid modes for the present case. For the sake of simplicity, only two layers of the composite material are considered. For the two layers of the composite material, two different fiber orientations are used for the out and inner layers. This configuration makes it possible to increase the torsional frequencies because they are dependent on the transverse shear modulus, that is a valuable property in a composite material. Tab.8.3.1 shows the first 15 no rigid modes for the composite structure. The first three no rigid modes are due to the boosters, as shown in Fig.8.16a, b and c. The global bending mode is highlighted in Fig.8.16d. The ability of the present one-dimensional model in the local analysis is shown in Fig.8.16e, f, and g. Shell-like modes are shown in Fig.8.16h, i and j, where the deformation of the plate does not follow the beam deformation.

MODE	*COMPOSITE*
DOF	42876
1	0.76
2	0.95
3	4.82
4	6.37
5	6.40
6	6.95
7	9.03
8	9.13
9	9.84
10	10.06
11	10.61
12	10.87
13	11.75
14	12.61
15	14.06

Table 8.8. First 15 no rigid modes for the composite launcher.

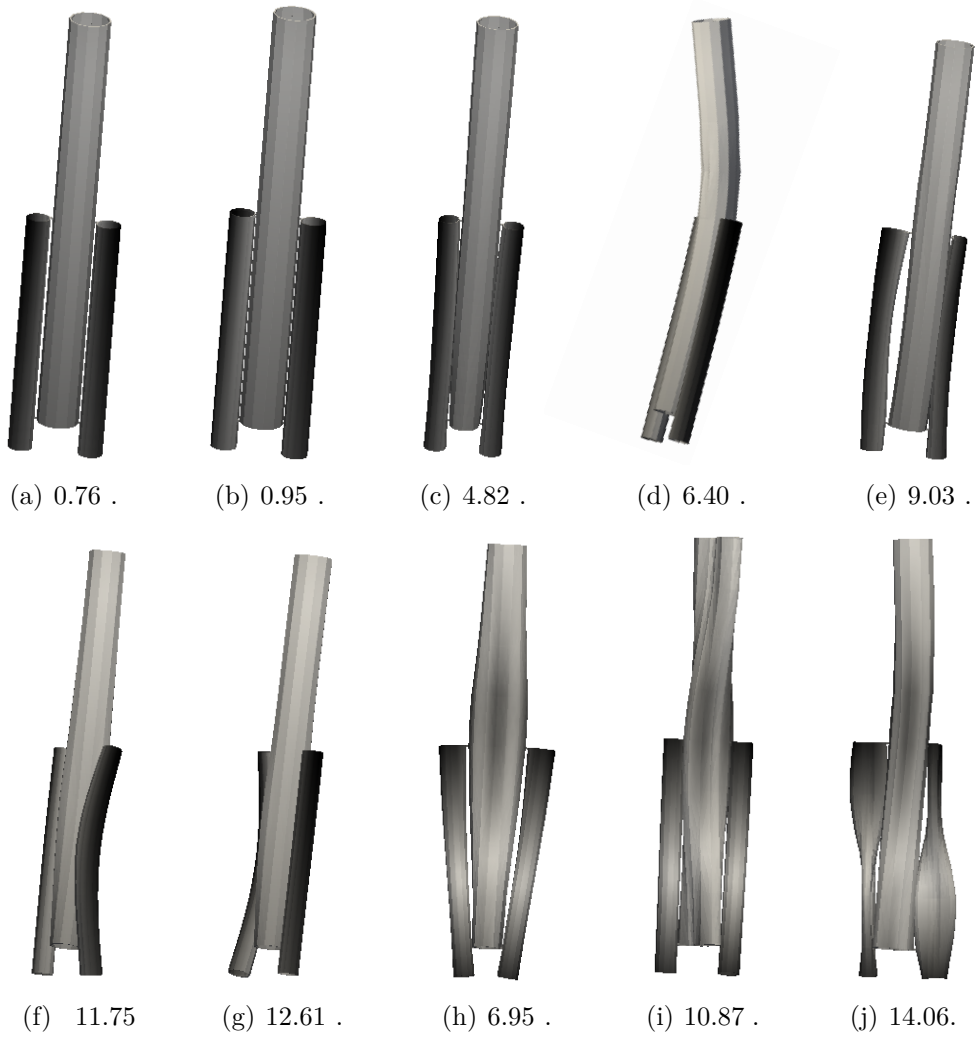

(a) 0.76 . (b) 0.95 . (c) 4.82 . (d) 6.40 . (e) 9.03 .

(f) 11.75 . (g) 12.61 . (h) 6.95 . (i) 10.87 . (j) 14.06.

Figure 8.16. Various Modes for the composite launcher in Hz.

8.3.2 Full Composite Launcher

In this section, the composite launcher analyzed previously, is studied including additional masses typically of the take-off phase, as shown in Fig.8.7. The full configuration comes from the manual of the Arian V Engineering [2011]. The boosters contain the solid fuel, while the cryogenic fuel is introduced into the central body. In the top of the launcher, there is the payload. Solid, cryogenic and payload masses are added like non-structural masses in the model. Each mass is located at the central node on the free-edge of the stringers, and they are spaced equally at about 3.375 [m] along the y direction, how Fig.8.12a shows.

8.3.3 Comparison of Composite Empty and Full launcher

Tab.8.9 shows the first fifteen no-rigid frequencies when the fuel and the payload masses are added to the empty launcher. The first effect concerns the reduction of the frequencies. In fact, if the whole stiffness does not change and the mass increases, the frequencies decreases, as shown in the column related to the full launcher proposed in the Tab.8.9. The models have the same number of the degrees of freedoms.

Mode	1	2	3	4	5	6	7	8	9	10	11	12	13	14	15
Empty	0.76	0.95	4.82	6.37	6.95	9.03	9.13	9.84	10.06	10.61	10.87	11.75	12.61	14.06	14.33
Full	0.28	0.42	1.63	2.71	3.34	3.87	4.06	4.06	4.29	4.37	4.39	4.59	4.72	5.08	5.70

Table 8.9. The first 15 no-rigid frequencies for empty and full configurations.

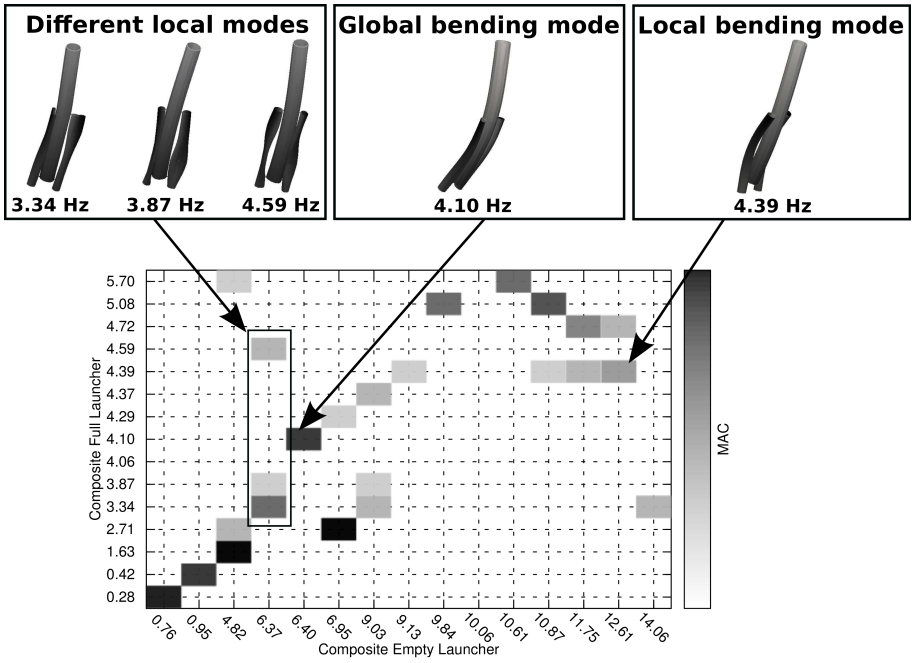

Figure 8.17. Comparison between empty and full composite launcher.

Fig.8.17 contains the comparison between the empty and full composite launcher. When the total weight increases due to fuel and the payload masses, different local shell-like modes due to the boosters appear before the global bending mode. Also, the global bending mode is after in the full launcher, in fact, it is mode 8 in the full configuration and mode 5 in the empty launcher case. By contrast, the local bending mode of the boosters in before in the full launcher than the empty launcher, in fact, it is mode 11 in the full launcher and mode 14 in the empty launcher.

Chapter 9

Conclusions

An advanced component-wise approach has been adopted to analyze thin structures reinforced using a set of stringers, that is, either transversal or rib, and longitudinal or stringer. This advanced structural configuration can be used in the various engineering field, from the civil engineering to the aerospace engineering, where reinforced structures were introduced to permit aircraft and space vehicle to fly. The adopted reinforced model fulfil the lightness and strength requirements, both of which are important properties when the structural weight is a project parameter.

Classical analysis approaches require the use of 3D models or the use of 2D, 1D models when the computational costs must be reduced. The coupling between 2D and 1D elements in the FE analysis is very used by engineers because this approach makes it possible to model reinforced structure very simple and to reduce the computational costs. In contrast, several geometrical and mathematical inconsistencies introduce error difficult to assess, carry out the result afflicted by largely hidden errors. In particular, the area of which the reduced 1D and 2D elements are coupled represents the focus of problems at the interface, well known by scientific community and engineers.

The advanced component-wise approach has been adopted to analyze the effect introduced by reinforcements when FE refined models are used to perform the static and dynamic analysis. The effects of the stringer can influence the solution locally regarding stress and displacement field and regard local vibration. The shape of the stringer is an additional parameter to consider when a reinforced structures must be analyzed.

Various analysis of simple components, such as plate and curved reinforced panels, are considered to analyze the behaviour of different FE models in the analysis of reinforced structures.

Solid, shell and shell-beam FE models are considered including also 1D refined models based on the Carrera Unified Formulation (CUF).

The CUF formulation is extended to complex reinforced structures. Reinforced

cylinders and an outline of a launcher with the shape similar to the European launcher Arian V are taken into account using isotropic and composite materials and including also the effect of non-structural masses.

From the results it is possible to state that:

- the 1D CUF models permit to analyze complex reinforced structure using a unique one-dimensional formulation without the need to include in the model various geometrical approximation, how shell and beam FE elements do;
- the refined one-dimensional models based on the CUF overcome the limitations of the classical FE reduced models and can detect both global and local (shell-like) modes;
- the LE solution provides accurate results even if different reinforcement geometries are considered;
- the refined one-dimensional LE models can provide a quasi-3D solution reducing the computational costs;
- the coupling between 2D and 1D elements in the FE models is an important aspect to consider when reinforced structures are analyzed;
- the accuracy of the results of static and dynamic analyses of reinforced structure adopting FE models is strongly influenced by the shape of the structure and also by the form of the stringer;
- the reduced 1D/2D FE models do not provide an accurate stress field. Despite the 1D elements are modeled including an appropriate offset, the stress field can be inaccurate if compared to a three-dimensional stress field;
- the reduced 1D/2D FE models are not accurate in the prediction of the local modes of the stringer;
- the present 1D models can be used in the analysis of complex reinforced structures, providing an high-fidelity description of the geometry;
- the 1D CUF models allow composite materials, non-structural masses and load factors to be included quickly;

In conclusion, the refined 1D-CUF models are very attractive compared to the reduced FE models when the reinforce structure are analyzed. The accuracy of the results and the computational efficiency make these models a valid alternative to the classical analysis approach.

The ability of the proposed model to introduce a three-dimensional displacement field and to predict complex stress fields, make the present one-dimensional model attractive for all the applications where local effects play an important role. The analysis of local and global buckling in complex reinforced structures, as well as, the failure analysis in civil structures, including the effects of fatigue and multiple damages, could be an interesting extension of the proposed method.

Chapter 10

Publications and Conference

Journal articles

- T. Cavallo, A. Pagani, E. Zappino and E. Carrera. Effect of Localized Damages in the Free Vibration Analysis of Civil Structures by Component-Wise Approach. *Journal of Structural Engineering (ASCE)*, 2017. Submitted.

- T. Cavallo, E. Carrera and E. Zappino. Component-Wise Vibration Analysis of Stiffened Plates Accounting for Stiffener Modes. *CEAS Aeronautical Journal*, 8 (2), pp 385-412, 2017.

- T. Cavallo, E. Carrera and E. Zappino. Free-Vibration Analysis of Space Vehicle Structures made by Composite materials. *Composite Structures*, 2016. In Press.

- E. Carrera, E. Zappino and T. Cavallo. Static Analysis of Reinforced Thin-Walled Plates and Shells by means of Various Finite Element Models. *International Journal for Computational Methods in Engineering Science & Mechanics*, DOI: 10.1080/15502287.2016.1157647, 2016.

- E. Carrera, E. Zappino and T. Cavallo. Accurate Free Vibration Analysis of Launcher Structures Using Refined 1D Models. *International Journal of Aeronautical and Space Sciences*, 16(2), pp. 206-222, 2015.

- E. Zappino, E. Carrera and T. Cavallo. Free Vibration analysis of Reinforced Thin-Walled Plates and Shells through Various Finite Element Models. *Mechanics of Advanced Materials and Structures*, DOI: 10.1080/15376494.2015.1121562, 2015.

Technical Notes

- E. Carrera, T. Cavallo and E. Zappino. Effect of Solid Mass Consumption on the Free Vibration Analysis of Launchers. Journal of Spacecraft and Rockets (AIAA), 54 (3), pp 774-781, 2017. doi: 10.2514/1.A33650

Conference Proceeding

- T. Cavallo, E. Zappino, A. Pagani and E. Carrera. A Component-Wise Approach to Analyse a Composite Launcher Structure subjected to Loading Factor. In International Mechanical Engineering Congress & Exposition (ASME 2016), Usa, Phoenix, November 11-17, 2016.

- T. Cavallo, E. Zappino, and E. Carrera. Analysis of Composite Launcher with non- structural Masses subjected to Loading Factor. In 14Th European Conference on Spacecraft Structures, Materials and Environmental Testing (ECSSMET), France, Toulouse, September 27-30, 2016.

- T. Cavallo, E. Zappino, M. Filippi and E. Carrera. Analysis of Composite Space Structures subjected to Loading Factor. In 19-th International Conference on Composite Structures, Portugal, Porto, September 5-9, 2016.

- E. Carrera, T. Cavallo and E. Zappino. Accurate Analysis of Launcher Structures by means of Refined One dimensional model. In 23-rd Conference of the Italian Association of Aeronautics and Astronautic, Torino, Italy, November 17-19, 2015.

- E. Carrera, E. Zappino and T. Cavallo. Structural Analysis of Launcher Structures by means of Refined Beam Models. In 11-th World Congress on Computational Mechanics , Barcelona, Spain, July 20-25, 2014.

- E. Zappino, T. Cavallo and E. Carrera. Component-Wise Approach for Efficient and Accurate Analysis of Structures of Launchers. In European Conference on Spacecraft Structures, Materials & Environmental Testing, Braunschweig, Germany, April 1-4, 2014.

Bibliography

R. J. Allemang and D. L. Brown. A correlation coefficient for modal vector analysis. *Proceedings of the 1st SEM International Modal Analysis Conference*, pages 110–116, 1982. Orlando, FL, November 8-10.

K.J. Bathe. *Finite element procedure*. Prentice hall, 1996.

O. A. Bauchau and J. I. Craig. *Structural Analysis: With Applications to Aerospace Structures.* Springer Science and Business Media, 2009.

C.W. Bert, S.K. Jang, and A.G. Striz. Nonlinear bending analysis of orthotropic rectangular plates by the method of differential quadrature. *Computational Mechanics*, 5(2/3):217–226, 1989.

W. B. Bickford. A consistent higher-order beam theory. *Developments in Theoretical and Applied Mechanics*, 11:137–150, 1982.

R. D. Buehrle, G. A. Fleming, and R. S. Pappa. Finite element model development and validation for aircraft fuselage structures. *18-th international Modal Analysis Conference.*, 2000a. San Antonio, Texas.

R.D. Buehrle, G.A. Fleming, and R.S. Pappa. Finite element model development and validation for aircraft fuselage structures. *18th International Modal Analysis Conference*, 2000b. San Antonio, Texas.

E. Carrera. Theories and finite elements for multilayered, anisotropic, composite plates and shells. *Archives of Computational Methods in Engineering.*, 9(2):87–140, 2002.

E. Carrera. Theories and finite elements for multilayered plates and shells: a unified compact formulation with numerical assessment and benchmarking. *Archives of Computational Methods in Engineering.*, 10(3):216–296, 2003.

E. Carrera and G. Giunta. Refined beam theories based on a unified formulation. *Int. J. Appl. Mech.*, 2(1):117–143, 2010a.

E. Carrera and G. Giunta. Refined beam theories based on a unified formulation. *International Journal of Applied Mechanics*, 2(1):117–143, 2010b.

E. Carrera, E. Zappino, and T. Cavallo. Effect of solid mass consumption on the free-vibration analysis of launchers. *Journal of Spacecraft and Rockets (AIAA)*. doi: 10.2514/1.A33650.

E. Carrera, G. Giunta, P. Nali, and M. Petrolo. Refined beam elements with arbitrary cross-section geometries. *Comput. Struct.*, 88(5-6):283–293, 2010.

E. Carrera, G. Giunta, and Petrolo M. *Beam Structures, Classical and Advanced Theories.* John Wiley & Sons, 2011a.

E. Carrera, M. Petrolo, and P. Nali. Unified formulation applied to free vibrations finite element analysis of beams with arbitrary section. *Shock Vib.*, 18(3):485–502, 2011b.

E. Carrera, A. Pagani, and M. Petrolo. Classical, refined and component-wise analysis of reinforced-shell structures. *AIAA Journal*, 51(5):1255–1268, 2013a.

E. Carrera, A. Pagani, and M. Petrolo. Component-wise method applied to vibration of wing structures. *Journal of Applied Mechanics*, 88(4):1–15, 2013b.

E. Carrera, M. Cinefra, M. Petrolo, and E. Zappino. *Finite Element Analysis of Structures Through Unified Formulation.* John Wiley & Sons, 2014a.

E. Carrera, M. Cinefra, M. Petrolo, and E. Zappino. Comparisons between 1d (beam) and 2d (plate/shell) finite elements to analyze thin walled structures. *Aerotecnica Misssili & Spazio. The journal of Aerospace Science, Technology and Systems*, 93(1-2), 2014b.

E. Carrera, E. Zappino, and T. Cavallo. Accurate free vibration analysis of launcher structures using refined 1d models. *International Journal of Aeronautical and Space Sciences*, 16(2):206–222, 2015.

E. Carrera, E. Zappino, and T. Cavallo. Static analysis of reinforced thin-walled plates and shells by means of various finite element models. *nternational Journal for Computational Methods in Engineering Science and Mechanics*, 17(2):106–126, 2016.

T. Cavallo, E. Zappino, and E. Carrera. Free-vibration analysis of space vehicle structures made by composite materials. *Composite structures*, a. In Press.

T. Cavallo, E. Zappino, and E. Carrera. Component-wise vibration analysis of stiffened plates accounting for stiffener modes. *CEAS Aeronautical Journal*, b. In press.

F. Civan. Solving multivariable mathematical models by the quadrature and cubature methods. *Numerical Methods for Partial Differential Equations*, 10:545–567, 1994.

R. Courant. Variational methods for the solution of problems of equilibrium and vibrations. *Bulletin of the American Mathematical Society*, 43:1–23, 1943.

M. Şimşek and T. Kocatuŕk. Free vibration analysis of beams by using a third-order shear deformation theory. *Sādhanā*, 32(3):167–179, 2007.

A. Deb and Booton M. Finite element models for stiffened plates under transverse loading. *Computers and Structures*, 8(3):361–372, 1988.

G. Durin, F. Bouvier, G. Mastrangelo, and E. Robert. Ariane 5 solid rocket booster dynamic behaviour with respect to pressure oscillations. *Progress in Propulsion Physics*, 2:149–162, March 2011a.

G. Durin, F. Bouvier, G. Mastrangelo, and E. Robert. Ariane 5 solid rocket booster dynamic behaviour with respect to pressure oscillation. *Propulsion Physics*, 2: 149–162, 2011b.

B. M. Efimtsov and L. A. Lazarev. Forced vibrations of plates and cylindrical shells with regular orthogonal system of stiffeners. *Journal of Sound and Vibration*, 327 (1-2):41–54, 2009.

Edouard Perez Senior Vice President Engineering. *Ariane 5, User s Manual.*, volume 5. arianespace service & solutions, 2011.

L. Euler. De curvis elasticis. methodus inveniendi lineas curvas maximi minimive proprietate gaudentes, sive solutio problematis iso-perimetrici lattissimo sensu accepti. 1744. Bousquet, Geneva.

J. Farsa, A.R. Kukreti, and C.W. Bert. Fundamental frequency analysis of single spacially orthotropic, generally orthotropic and anisotropic rectangular layered plates by differential quadrature method. *Computers and Structures*, 46(3):465–477, 1993.

L. Gan, X Li, and Z. Zhang. Free vibration analysis of ring-stiffened cylindrical shells using wave propagation approach. *Journal of Sound and Vibration*, 326: 633–646, 2009.

R. Ganesan and A. Zabihollah. Vibration analysis of tapered composite beams using a higher-order finite element, part i: Formulation. *Composite Structures*, 77(3): 306–318, 2007a.

R. Ganesan and A. Zabihollah. Vibration analysis of tapered composite beams using a higher-order finite element, part ii: Parametric study. *Composite Structures*, 77 (3):319–330, 2007b.

B. Prusty Gangadhara. Linear static analysis of hat stiffened laminated shells using finite elements. *Finite elements in analysis and design.*, 39:1125–1138, 2003.

G. Giunta, F. Biscani, S. Belouettar, A. J. M. Ferreira, and E. Carrera. Free vibration analysis of composite beams via refined theories. *Composite Part B*, 44(1): 540–552, 2013.

Q. Guanghui, F. Zhenyu, L. Yanhong, and Q. Jiaujun. A semianalytical solution for free vibration analysis of stiffened cylindrical shells. *Journal of Mechanic of Materials and Structures*, 1(1), 2006.

J-L. Guyader, C. Cacciolati, and E. Guyader. Prediction of vibroacoustic behaviour of multilayered structures using equivalent materials. 2010. Proceedings of 17th International Congress on Sound and Vibration, Cairo, Egypt.

P. R. Heyliger and J. N. Reddy. A higher order beam finite element for bending and vibration problems. *Journal of Sound and Vibration*, 126(2):309–326, 1988.

C. H. Hodges, J. Power, and J. Woodhouse. The low frequency vibration of a ribbed cylinder, part 1: theory. *Journal of Sound and Vibration*, 101(2):219–235, 1985.

A. Hrennikoff. Solution of problems of elasticity by the framework method. *Journal of applied mechanics*, 12:169–175, 1941.

M. C. Junger and D. Feit. *Sound, Structures and Their Interaction. 2nd ed.* Acoustical Society of America, 1993. New York.

T. kant and A. Gupta. A finite element model for a higher-order shear deformable beam theory. *Journal of Sound and Vibration*, 125(2):193–202, 1988.

K. Kapania and S. Raciti. Recent advances in analysis of laminated beams and plates, part i: Shear effects and buckling. *AIAA Journal*, 27(7):923–935, 1989a.

K. Kapania and S. Raciti. Recent advances in analysis of laminated beams and plates, part ii: Vibrations and wave propagation. *AIAA Journal*, 27(7):935–946, 1989b.

G. Kirchhoff. Ueber das gleichgwich und die bewegung einer elastischen schiebe. *J. Angew. Math.*, 40:51–88, 1850.

M. Kolli and K. Chandrashekhara. Finite element analysis of stiffened laminated plates under transverse loading. *Composite Science and Technology.*, 56:1355–1361, 1996.

R. S. Langley. Application of the dynamic stiffness method to the free and forced vibrations of aircraft panels. *Journal of Sound and Vibration*, 135(2):319–331, 1989.

Summer A. Leadbetter, Wendell B. Stephens, John L. Sewall, Joe W. Majka, and Barrett jack R. Vibration characteristics of 1/8-scale dynamic models of the space-shuttle solid-rocket boosters. *NASA TN D-8158*, 1976. Langley Research Center, Hampton.

J-H. Lee and J. Kim. Sound transmission through periodically stiffened cylindrical shells. *Journal of Sound and Vibration*, 251(3):431–456, 2002.

A. Leissa. *Vibration of Plates.* Acoustical Society of America, 1993a. New York.

A. Leissa. *Vibration of Shells.* Acoustical Society of America, 1993b. New York.

A. W. Leissa. Vibration of plate. *NASA*, 1969. SP-160.

M. Levinson. A new rectangular beam theory. *Journal of Sound and Vibration*, 74 (1):81–87, 1981.

A. E. H. Love. The mathematical theory of elasticity, 4th editions. *Cambridge University press*, 1927. Cambridge.

Y. Luan, M. Ohrlich, and F. Jacobsen. Improvements of the smearing technique for cross-stiffened thin rectangular plates. *Journal of Sound and Vibration*, 330: 4274–4286, 2011.

B. R. Mace. Periodically stiffened fluid-loaded plates, ii: response to line and point forces. *Journal of Sound and Vibration*, 73(4):487–504, 1980.

B. Manzanares, J. Flores, L. Gutierrez, R.A. Mendez, G. Monsivais, A. Morales, and F. Ramos. Flexural vibrations of a rectangular plate for the lower normal modes. *Journal of Sound and Vibration*, 329:5105–5115, 2010.

S. R. Marur and T. kant. Free vibration analysis of fiber reinforced composite beams using higher order theories and finite element modelling. *Journal of Sound and Vibration*, 194(3):337–351, 1996.

S. R. Marur and T. kant. On the angle ply higher order beam vibrations. *Computational Mechanics*, 40:25–33, 2007.

S. R. Marur, T. kant, and G. S. Rao. Analytical solution to the dynamic analysis of laminated beams using higher order refined theory. *Composite Structures*, 40 (1):1–9, 1997.

H. Matsunaga. Buckling instabilities of thick elastic beams subjected to axial stress. *Comput. Struct.*, 59(5):859–868, 1996.

D. J. Mead and N. S. Bardell. Free vibration of a thin cylindrical shell with discrete axial stiffeners. *Journal of Sound and Vibration*, 111(2):229–50, 1986.

D. J. Mead and N. S. Bardell. Free vibration of a thin cylindrical shell with periodic circumferential stiffeners. *Journal of Sound and Vibration*, 115(3):499–520, 1987.

N. Merlette and E. Pagnacco. Structural dynamics of solid propellants with frequency dependent properties. *12-th European Conference os Space Structures, Materials & Enviromental Testing.*, 2012. Noordwijk, The Netherlands.

R. D. Mindlin. Influence of rotatory inertia and shear on flexural motions of isotropic, elastic plates. *ASME Journal of Applied Mechanics*, 18:31–38, 1951.

V. V. Novozhilov. *Theory of elasticity.* 1961. Elmsford.

E. Oñate. *Structural Analysis with the Finite Element Method: Linear Statics, Volume 1.* Springer, Barcelona, Spain, 2009.

C. Omid'varan. Free vibration of grid-stiffened plates. *Journal of Sound and Vibration*, 19:463–472, 1971.

C. Omid'varan and W. Delagarza. Vibration of monolithic grid-stiffened plates. *Journal of Sound and Vibration*, 26:21–28, 1973.

A. Pagani, F. Zangallo, and E. Carrera. Influence of non-structural localized inertia on free vibration response of thin-walled structures by variable kinematic beam formulations. *Shock and Vibration*, 11, 2014. doi: http://dx.doi.org/10.1155/2014/141982.

S. N. Patel, P. K. Datta, and A.H. Seikh. Buckling and dynamic instability analysis of stiffened shell panels. *Thin-Walled Structures*, 44:321–333b, 2006.

Z. Ping, Z.X. Leia, and K.M. Liew. Static and free vibration analyses of carbon nanotube-reinforced composite plates using finite element method with first order shear deformation plate theory. *Composite Structures*, 19:1450–1460, 2012.

E. Reissner. The effect of transverse shear deformation on the bending of elastic plates. *ASME Journal of Applied Mechanics*, 12:68–77, 1945.

R.E. Rossi and P.A.A. Laura. On the effect of the poissonâs ratio and certain approximation schemes on transverse vibrations of thin rectangular plates with a free edge. *Journal of Sound and Vibration*, 194(3), 1996.

Z. Rychter. On the accuracy of a beam theory. *Mechanics Research Communications*, 14(2):99–105, 1987.

S. K. Satsangi and M. Mukhopadhyay. Finite element state analysis of girder bridges having arbitrary platform. *Int. Ass. of Bridge Struct. Engng.*, 17:65–94, 1987.

N. Silvestre. Second-order generalised beam theory for arbitrary orthotropic materials. *Thin-Walled Structures*, 40(9):791–820, 2002.

K. P. Soldatos and I. Elishakoff. A transverse shear and normal deformable orthotropic beam theory. *Journal of Sound and Vibration*, 155(3):528–533, 1992.

N. G. Stephen and M. Levinson. A second order beam theory. *Journal of Sound and Vibration*, 63(3):293–305, 1979.

G. Strang and G. Fix. *An Analysis of the Finite Element Method*. 1973.

P. Subramanian. Dynamic analysis of laminated composite beams using higher order theories and finite elements. *Composite Structures*, 73(3):342–353, 2006.

R. Szilard. *Theories and Applications of Plate Analysis*. John Wiley & Sons, 2004. Hoboken, New York.

T. I. Thinh and N. N. Khoa. Free vibration analysis of stiffened laminated plates using a new stiffened element. *Technische Mechanik.*, 28(2-3):227–236, 2008.

S. P. Timoshenko. On the correction for shear of the differential equation for transverse vibrations of prismatic bars. *Philosophical Magazine*, 41:744–746, 1921.

S. P. Timoshenko. *Theory of Elastic Stability*. McGraw-Hill, 1961. New York.

S. P. Timoshenko and J. N. Goodier. Theory of elasticity. *McGraw-Hill*, 1951.

S.P. Timoshenko. *Theory of Plates and Shells, 2nd ed.* McGraw-Hill, 1959. New York.

M. S. Troitsky. *Stiffened Plates: Bending, Stability and Vibrations*. Oxford Pergamon Press, 1976.

V. Z. Vlasov. Thin-walled elastic beams. *National Science Foundation*, 1961. Washington.

G. M. Voŕoš. A special purpose element for shell-beam systems. *Computers and Structures*, 29(2):301–308, 1988.

K. Washizu. *Variational methods in elasticity and plasticity.* Oxford: Pergamon Press, 1968.

W. Yu, V. Volovoi, D. Hodges, and X. Hong. Validation of the variational asymptotic beam sectional analysis (vabs. *AIAA Journal*, 40(10):2105–2113, 2002.